Rotation of multimode Gauss–Laguerre light beams in free space

V. V. Kotlyar, V. A. Soĭfer, and S. N. Khonina

Institute of Image Processing Systems, Russian Academy of Sciences, Samara
(Submitted November 18, 1996)
Pis'ma Zh. Tekh. Fiz. **23**, 1–6 (September 12, 1997)

An iterative algorithm is presented for calculating diffractive phase optical elements that form light beams which are an effective superposition of a small number of nonradially symmetric Gauss–Laguerre modes with a prescribed energy contribution from each mode.
 [S1063-7850(97)00109-2]

An important current problem is the development of diffractive optical elements that are matched with light modes of one type or another. Such diffractive optical elements find applications in the problems of parallel injection of radiation into a fiber bundle, selection of transverse laser modes, and formation of nondiffracting beams.[1]

Iterative methods exist for calculating diffractive phase optical elements capable of forming light beams with a prescribed composition of Gauss–Hermite modes,[2] Gauss–Hermite[3] and Gauss–Laguerre[4] modes in different diffraction orders, and Bessel modes (nondiffracting beams).[5] Only radially symmetric Gauss–Laguerre modes are studied in Ref. 4.

The conditions under which rotation of a multimode beam around the propagation axis is observed have also been found, and an expression has been obtained for the total number of revolutions.

It is known[6] that light fields which are a superposition of Gauss–Laguerre modes satisfy the Helmholtz equation. The complex amplitude of such fields in free space can be represented in cylindrical coordinates (r,φ,z) as

$$U(r,\varphi,z)=\exp\left[ikz+\frac{ikr^2}{2R}-\frac{r^2}{\sigma^2}\right]\times\sum_{m,n=0}^{\infty}C_{mn}\left(\frac{\sqrt{2}r}{\sigma}\right)^n L_m^n\left(\frac{2r^2}{\sigma^2}\right)\times\exp[-i\beta_{mn}(z)\pm in\varphi], \tag{1}$$

where

$$\beta_{mn}(z)=(2m+n+1)\tan^{-1}(z/z_0), \tag{2}$$

$R=z(1+z_0^2/z^2)$ is the radius of curvature of the parabolic front of the light field, $\sigma^2=\sigma_0^2(1+z^2/z_0^2)$ is the effective radius of the beam, $2z_0=2\pi\sigma_0^2/\lambda$ is the confocal parameter, σ_0 is the radius of the beam waist, C_{mn} are constant coefficients, and k is the wave number of light with wavelength λ.

To generate a light beam with the amplitude (1) it is necessary to form in the plane $z=0$ the complex amplitude

$$U_0(r,\varphi)=\sum_{m,n=0}^{\infty}C_{mn}\Omega_{mn}^{\pm}(r,\varphi), \tag{3}$$

where we have introduced the following notation for the orthonormalized mode basis functions

$$\Omega_{mn}^{\pm}(r,\varphi)=\left[\frac{2(m-n)!}{\pi\sigma_0^2(m!)^3}\right]^{1/2}\left(\frac{\sqrt{2}r}{\sigma_0}\right)^n L_m^n\left(\frac{2r^2}{\sigma_0^2}\right)\times\exp\left(-\frac{r^2}{\sigma_0^2}\pm in\varphi\right). \tag{4}$$

An iterative algorithm for calculating the parameters of a diffractive phase optical element forming the complex amplitude (3) has the form

$$S_{k+1}(r,\varphi)=\arg\left\{\sum_{m,n=0}^{\infty}B_{mn}\Omega_{mn}^{\pm}(r,\varphi)\exp[iv_{mn}^{(k)}]\right\}, \tag{5}$$

$$v_{mn}^{(k)}=\arg\left\{\int_0^{\infty}\int_0^{2\pi}A_0(r,\varphi)\exp[iS_k(r,\varphi)]\times\Omega_{mn}^{\pm *}(r,\varphi)r\,dr\,d\varphi\right\}, \tag{6}$$

where $A_0(r,\varphi)=|U_0(r,\varphi)|$ is the amplitude of the illuminating beam, $S_k(r,\varphi)$ is the phase of the diffractive optical element calculated at the kth iteration, and $B_{mn}\geqslant 0$ are given numbers which specify the energy contribution of the corresponding mode.

Next, we shall obtain the condition for observing rotation of the transverse section of a multimode beam. On the basis of Eq. (1), we write an expression for the intensity $I(r,\varphi,z)=|U(r,\varphi,z)|^2$

$$I(r,\varphi,z)=\exp\left[-\frac{2r^2}{\sigma^2}\right]\left\{\sum_{m,n=0}^{\infty}|C_{mn}|^2\left(\frac{\sqrt{2}r}{\sigma}\right)^{2n}\left|L_m^n\left(\frac{2r^2}{\sigma^2}\right)\right|^2+2\sum_{m\neq m'}\sum_{n\neq n'}|C_{mn}C_{m'n'}|\left(\frac{\sqrt{2}r}{\sigma}\right)^{n+n'}\left|L_m^n\left(\frac{2r^2}{\sigma^2}\right)\times L_{m'}^{n'}\left(\frac{2r^2}{\sigma^2}\right)\right|\cos\Phi_{m'n'}^{mn}(r,\varphi)\right\}, \tag{7}$$

where

$$\Phi_{m'n'}^{mn}(r,\varphi)=\arg C_{mn}-\arg C_{m'n'}+[2(m-m')+(n-n')]\tan^{-1}\frac{z}{z_0}\pm(n-n')\varphi. \tag{8}$$

All terms in the second sum in Eq. (7) will rotate at the same rate (and the entire beam will rotate as a whole) if, in the expression for the polar angle φ as a function of the distance z,

$$\varphi = B \tan^{-1} \frac{z}{z_0}, \tag{9}$$

the coefficient B is constant:

$$B = \frac{2(m-m') + (n-n')}{\mp(n-n')} = \text{const}. \tag{10}$$

The distance z_p over which the beam makes p revolutions can be found from Eq. (9):

$$z_p = z_0 \tan\left(\frac{2\pi p}{B}\right), \quad p = 1,2,\ldots,N, \tag{11}$$

where $N = B/4$ is the maximum number of revolutions which the beam can make from $z=0$ to $z=\infty$ ($z \gg z_0$). The rotation rate ν of the transverse section of a multimode beam depends on the distance z as

$$v = \frac{d\varphi}{dz} = B\left[1 + \left(\frac{z}{z_0}\right)^2\right]^{-1}. \tag{12}$$

It follows from what we have said above that by choosing the nonzero terms in Eq. (3) with numbers satisfying the condition (10) it is possible to use Eqs. (5) and (6) to design phase optical elements which when illuminated by laser light form, with a high efficiency, nonradially symmetric multimode Gauss–Laguerre beams whose intensity distribution in the transverse section rotates around the propagation axis.

The numerical modeling parameters are: number of mesh points 256×256, waist radius $\sigma_0 = 0.1$ mm, wavelength $\lambda = 0.63$ μm, radius of the diffractive optical element $R_0 = 0.5$ mm, and confocal parameter $z_0 = 49.86$ mm.

Numerical examples are displayed in Fig. 1. Column 1 shows the phase of the diffractive optical element (1a) calculated according to Eqs. (3)–(6) with two nonzero terms in the sum (3), with the coefficients $C_{1,-1}$ and $C_{11,2}$ is shown in column 1. For two terms condition (10) obviously holds, and $B=7$. The maximum number of revolutions $N=1.75$. It follows from Eq. (11) that the beam will have made a complete revolution over a distance $z=62.53$ mm and another half revolution at $z=217.76$ mm. Figure 1 shows halftone renderings of the normalized transverse distributions of the intensity of a light beam formed by a diffractive phase optical element (1a) and the distributions computed using a Fresnel transformation in the planes $z=62.53$ mm (1b), $z=101.34$ mm (1c), $z=140.15$ mm (1d), $z=178.95$ mm (1e), and $z=217.76$ mm (1f). The pattern rotates counterclockwise.

Similar results for a rotating beam consisting of three modes with the coefficients $C_{1,-1}$, $C_{5,0}$, and $C_{11,2}$ are shown in column 2. Condition (10) holds: $B=7$, 7, and 7. The phase function of such an element (2a) is shown in halftones (black is 2π, white is 0). The transverse intensity distributions for such a beam (2b–2f) are shown at the same distances as in column 1.

The phase (3a) and an intensity section (3b)–(3f) for a three-mode beam with the coefficients $C_{2,-2}$, $C_{5,0}$, and $C_{15,2}$ are presented in column 3. Condition (10) does not hold — $B=2$, 6, and 11, and different parts of the beam rotate with different rates, which results in distortion rather than rotation of the pattern.

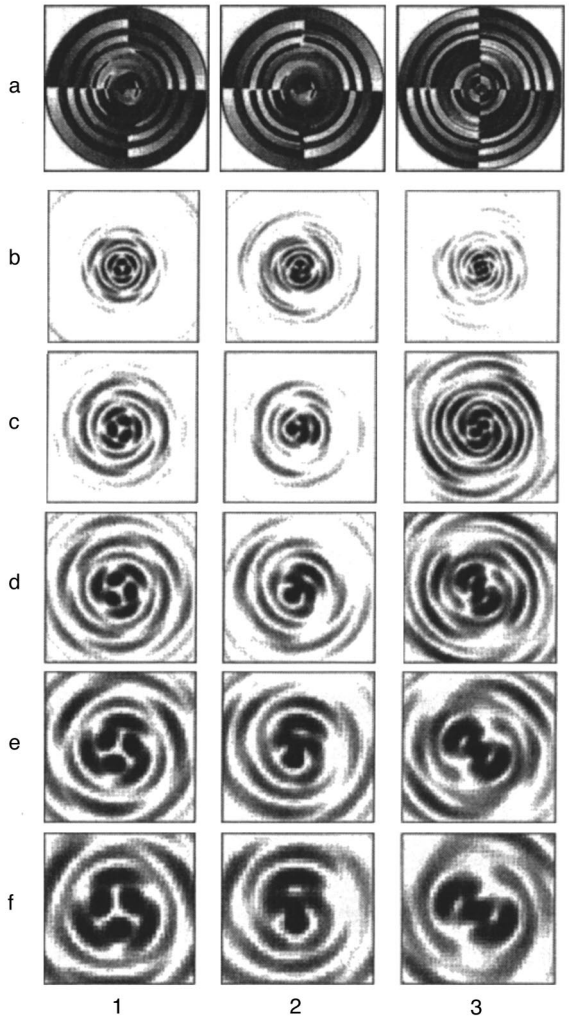

FIG. 1. Phases of diffractive optical elements forming multimode Gauss–Laguerre beams (a) and normalized transverse intensity distributions at different distances from the diffractive optical element (b–f).

[1] V. A. Soifer and M. A. Golub, *Laser Beam Mode Selection by Computer Generated Holograms*, CRC Press, Boca Raton, 1994.

[2] V. V. Kotlyar, I. V. Nikol'skiĭ, and V. A. Soĭfer, Opt. Spektrosk. **75**, 918 (1993).

[3] V. V. Kotlyar, I. V. Nikol'skiĭ, and V. A. Soĭfer, Pis'ma Zh. Tekh. Fiz. **19**(20), 20 (1993) [Tech. Phys. Lett. **19**, 645 (1993)].

[4] V. V. Kotlyar, I. V. Nikolsky, and V. A. Soifer, Optik **98**, 26 (1994).

[5] V. V. Kotlyar, S. N. Khonina, and V. A. Soifer, J. Mod. Opt. **42**, 1231 (1995).

[6] A. Yariv, *Optical Electronics in Modern Communications*, Oxford University Press, New York, 1997, 5th edition [Russian translation, Sov. Radio, Moscow, 1986].

Translated by M. E. Alferieff

Anisotropic scattering of polarized light in a ferrofluid layer

A. V. Skripal' and D. A. Usanov

Saratov State University
(Submitted January 22, 1997)
Pis'ma Zh. Tekh. Fiz. **23**, 7–10 (September 12, 1997)

Previously unknown effects wherein the scattering of plane-polarized light in a ferrofluid layer depends on the orientation of the electric field of the polarized radiation relative to the direction of the applied magnetic field are found experimentally, and their physical nature is explained. [S1063-7850(97)00209-7]

The scattering of polarized light in ferrofluids has been studied primarily in dilute colloidal solutions.[1,2] The character of the scattering of radiation incident on a thin layer of a concentrated ferrofluid was analyzed in Refs. 3 and 4. However, the analysis of the results did not include an investigation of the effect of the relative orientation of the electric field vector of the incident light and the magnetic field applied to the ferrofluid.

It can be conjectured that this effect will be strongest in the scattering of light by agglomerates of ferroparticles smaller than or comparable in size to the wavelength of the incident radiation. Our objective in the present work was to investigate the effect of the relative orientation of the electric field vector of the light wave and the magnetic field on the scattering of plane-polarized optical radiation in a ferrofluid.

The scattering of linearly polarized light in a layer of a water-based ferrofluid containing magnetite particles coated with sodium oleate and having a solid-phase concentration $\varphi = 0.1$ was detected with the apparatus shown schematically in Fig. 1. The electric field vector of the 0.6328 μm polarized radiation from a He–Ne laser *1* was oriented either parallel ($E_\parallel$) or perpendicular ($E_\perp$) to the direction of the magnetic field $\overline{H}$ applied in the plane of the ferrofluid layer *2*. The laser radiation was directed onto the ferrofluid layer *2*, which was sandwiched between glass plates. The laser radiation scattered by the ferrofluid layer was detected with a photodetector *6* placed at an angle $\theta = 5°$ with respect to the direction of incidence of the laser radiation.

Figure 2 shows the intensity of the scattered light as a function of the applied magnetic field for $E_\parallel$ (curve 1) and $E_\perp$ (curve 2). As one can see from Fig. 2, for weak magnetic fields the scattering of light is stronger for the case when the electric field vector is oriented parallel to the magnetic field. As the intensity of the applied magnetic field increases, the difference in the intensities of the scattered radiation for $E_\parallel$ and $E_\perp$ vanishes. As one can see from Fig. 2, the threshold magnetic field $H_{n\parallel}$ for the parallel orientation of the vectors $\overline{E}$ and $\overline{H}$, which is determined as shown in the same Fig. 2, turns out to be much lower than the threshold magnetic field for the perpendicular orientation of the electric and magnetic field vectors ($H_{n\perp}$). Since the threshold magnetic field for the onset of anisotropic light scattering is a function of the size of the agglomerates of ferroparticles,[3] the difference in the values of the threshold magnetic fields $H_{n\parallel}$ and $H_{n\perp}$ can be explained by the difference in the sizes of the ferroparticle agglomerates in directions parallel to and orthogonal to the magnetic field.

The difference in the values of the threshold magnetic fields in Fig. 2 is characteristic for structuring of a ferrofluid in the bulk. Indeed, the appearance of light scattering corresponds to the formation of structures in the liquid which are comparable in size to the wavelength of light (fractions of a micron). For a liquid layer of the order of several tens of microns thick this corresponds to the conditions for the formation of agglomerates in the bulk of the ferrofluid.

In summary, we have established that when linearly polarized light is scattered by a thin ferrofluid layer in a magnetic field oriented parallel to the boundaries of the flat layer

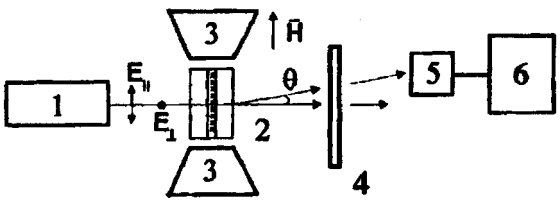

FIG. 1. Schematic diagram of the experimental apparatus: *1* — Laser, *2* — ferrofluid layer between two glass plates, *3* — poles of an electromagnet, *4* — screen, *5* — photodetector, *6* — display.

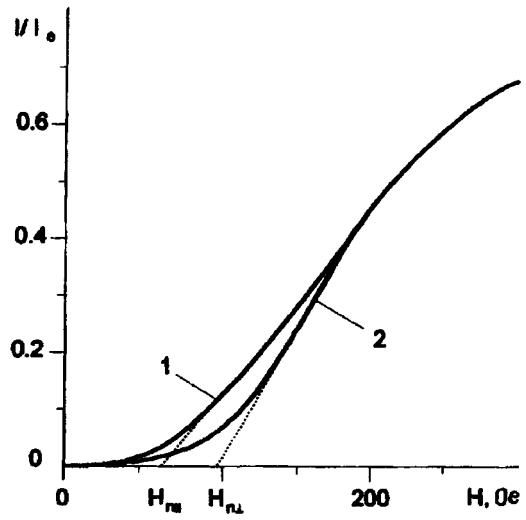

FIG. 2. Normalized scattered light intensity versus magnetic field intensity for different orientations of the electric field vector: *1* — Parallel to the magnetic field, *2* — perpendicular to the magnetic field.

 1063-7850/97/090659-02$10.00

a large difference is observed in the dependence of the intensity of the scattered light on the magnetic field intensity between the cases of parallel and perpendicular orientation of the electric field vector of the polarized laser radiation relative to the direction of the magnetic field. The observed anisotropic light scattering can be explained by the difference in the sizes of the ferroparticle agglomerates in directions parallel to and perpendicular to the electric field vector of the laser radiation for different orientations of the magnetic field.

[1] Yu. N. Skibin, V. V. Chekanov, and Yu. L. Raĭkher, Zh. Éksp. Teor. Fiz. **72**, 949 (1977) [Sov. Phys. JETP **45**, 496 (1977)].
[2] V. I. Drozdova, Yu. N. Skibin, and G. V. Shagrova, Magn. Gidrodin., No. 2, 63 (1987).
[3] É. Ya. Blum, M. M. Maĭorov, and A. O. Tsebers, *Ferrofluids* [in Russian], Zinatne, Riga, 1989.
[4] D. A. Usanov, A. V. Skripal', S. A. Ermolaev, and V. V. Panov, Pis'ma Zh. Tekh. Fiz. **21**(17), 1 (1995) [Tech. Phys. Lett. **21**, 677 (1995)].

Translated by M. E. Alferieff

Temperature dependence of the intensity and phase of reflected light in a liquid-crystal structure with surface plasmons

V. F. Nazvanov and D. I. Kovalenko

Saratov State University
(Submitted February 20, 1997)
Pis'ma Zh. Tekh. Fiz. **23**, 11–15 (September 12, 1997)

The results of a theoretical calculation of the temperature dependence of the amplitude coefficient and phase of reflected radiation with wavelength $\lambda = 6328$ Å in a liquid-crystal structure with surface plasmons are reported for the first time. The computational results could be helpful for developing temperature sensors and optically coupled thermal imagers based on liquid-crystal structures with surface plasmons. © *1997 American Institute of Physics.*
[S1063-7850(97)00309-1]

In our opinion the problem addressed here is a pressing one. Great interest has been shown in surface plasmons in recent years in connection with their application in surface spectroscopy, optical microscopy, the development of optical sensors for various physical quantities, electrically and optically controlled light modulators including liquid-crystal modulators, and other devices.[1–3] The working principle and the construction of an optical temperature sensor employing surface plasmons in a structure (Kretschmann geometry) made from a material with a strongly temperature-dependent refractive index are described in Ref. 4, where amorphous hydrogenated silicon layers deposited on a silver film in a glow discharge were used as such a material.

This letter reports the results of the first calculation of the temperature dependence of the amplitude coefficient and phase of reflected radiation with wavelength $\lambda = 6328$ Å in a liquid-crystal structure with surface plasmons.

It is well known[5,6] that the physical properties of liquid crystals, specifically, the birefringence, are temperature-dependent. This property is widely used for determining the optimal working temperature and the measure of performance of liquid-crystal light modulators for the visible and infrared regions of the spectrum,[7,8] the development of liquid-crystal sensors of temperature fluctuations,[9] and optically coupled thermal imagers.[10] Finally, heat effects in liquid crystals are very important in thermally induced optical bistability phenomena in liquid-crystal structures both with[11] and without[12] surface plasmons. Thus the relevance of the present work is not in doubt.

We employed the following liquid-crystal structure: glass prism — layer of silver — SiO_x — a plane-oriented layer of a nematic liquid crystal. Just as in Ref. 3, we employed the matrix method for the calculations. In the calculations, the dielectric constant of the glass, silver, SiO_x, and liquid crystal (type E7) were taken to be 3.24, $-17+i0.7$, $2.61+i0.02$, and $2.305+0.0033(T-45\ ^\circ\mathrm{C})$ (Ref. 13), respectively, and the silver and SiO_x layers were taken to be 470 and 250 Å thick, respectively.

The computational results are displayed in Figs. 1 and 2. Figure 1a shows the amplitude reflection coefficient R for p-polarized $\lambda = 6328$ Å radiation as a function of the angle of incidence φ at different temperatures below the point of transition of the liquid crystal to an isotropic liquid, and Fig. 1b shows the corresponding results for the phase φ of the reflected radiation. As expected, heating of the liquid crystal resulted in a shift of the resonance curve and, correspondingly, of the jump in phase to larger angles of incidence

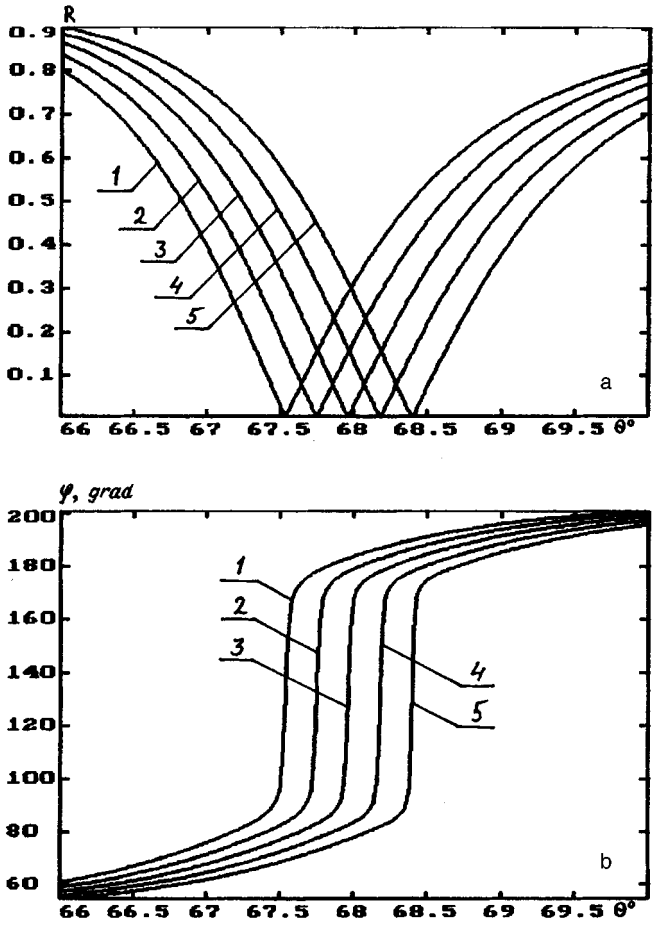

FIG. 1. a — Energy reflection coefficient versus angle of incidence of radiation with $\lambda = 6328$ Å. The curves were constructed at different temperatures: *1* — 45 °C, *2* — 47.5 °C, *3* — 50 °C, *4* — 52.5 °C, *5* — 55 °C. b — Phase shift between the *p* and *s* components of the reflected radiation as a function of the angle of incidence of $\lambda = 6328$ Å radiation. The curves were constructed at different temperatures: *1* — 45 °C, *2* — 47.5 °C, *3* — 50 °C, *4* — 52.5 °C, *5* — 55.5 °C.

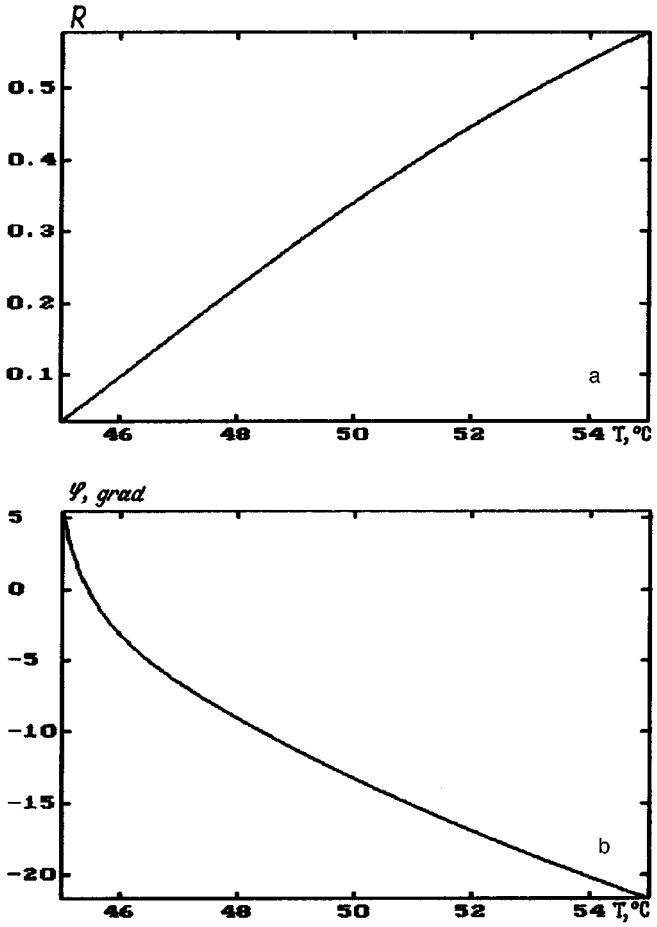

FIG. 2. a — Energy reflection coefficient versus temperature. The curve was constructed for an angle of incidence of 67.5° for radiation with $\lambda = 5328$ Å. b — Phase shift between the *p* and *s* components of the reflected radiation versus temperature. The curve was constructed for an angle of incidence of 67.5° for radiation with $\lambda = 6328$ Å.

(angles of the minimum of the resonance curves of the surface plasmons).

The results presented in Fig. 1 served as the basis for finding the temperature dependences $R(T)$ and $\varphi(T)$ displayed in Figs. 2a and 2b, respectively. As one can see from Fig. 2a, as the temperature of the liquid crystal varies over the range 45–55 °C, the intensity of the reflected light increases (by a factor of ~ 5) with temperature. The same is also true of the change in phase of the reflected radiation (Fig. 2b).

When such an apparatus is used as a temperature sensor and for measuring the reflection coefficient of radiation at a fixed angle θ_c less than the angle θ_p of the minimum in the resonance curve, the sensitivity of such a sensor,

$$S = \left[\frac{dR}{d\theta}\cdot\frac{d\theta}{dT}\right]_{\theta=\theta_c} \approx \left[\frac{dR}{dT}\cdot\frac{d\theta_p}{dT}\right],$$

is found to be of the order of 0.1605 deg^{-1} according to the data in Fig. 2a. For remote temperature sensing this apparatus can be joined to a fiber-optic waveguide.[4]

In summary, this letter reports the results of the first theoretical calculation of the temperature dependence of the amplitude coefficient and phase of reflected *p*-polarized radiation ($\lambda = 6328$ Å) in a liquid-crystal structure with surface plasmons. The computational results could be helpful in the development of liquid-crystal temperature sensors and other devices (for example, optically coupled thermal imagers).

[1] K. R. Welford, Opt. Quantum Electron. **23**, 1 (1991).
[2] V. F. Nazvanov and O. A. Afonin, Pis'ma Zh. Tekh. Fiz. **20**(7), 26 (1994) [Tech. Phys. Lett. **20**, 271 (1994)].
[3] V. F. Nazvanov and D. I. Kovalenko, Pis'ma Zh. Tekh. Fiz. **21**(14), 60 (1995) [Tech. Phys. Lett. **21**, 565 (1995)].
[4] B. Chadwick and M. Gal, Jpn. J. Appl. Phys. Pt. I **32**, 2716 (1993).
[5] L. M. Blinov, *Electro-Optical and Magneto-Optical Properties of Liquid Crystals*, Wiley, New York, 1983 [Russian original, Nauka, Moscow, 1978].
[6] P.-G. de Gennes, *The Physics of Liquid Crystals*, Clarendon Press, Oxford, 1974 [Russian translation, Mir, Moscow, 1977].
[7] S.-T. Wu, Anna M. Lackner, and U. Efron, Appl. Optics **28**, 3442 (1987).
[8] V. V. Belyaev, V. G. Chigrinov, N. F. Kovtonyuk, and A. B. Kuznetsov, Zh. Tekh. Fiz. **61**, 105 (1991) [Sov. Phys. Tech. Phys. **36**, 1254 (1991)].
[9] Yu. V. Bocharov, I. N. Gurova, O. A. Kapustina *et al.*, Sensors and Actuators A **28**, 179 (1991).
[10] R. G. Humphreys and H. A. Tarry, Infrared Phys. **28**(2), 113 (1988).
[11] R. A. Innes and J. R. Sambles, Optics Commun. **64**, 288 (1987).
[12] L. Vicari, F. Bloisi, and F. Simoni, Appl. Phys. B **53**, 314 (1991).
[13] R. A. Innes and J. R. Sambles, J. Phys.: Condens. Matter **1**, 6231 (1989).

Translated by M. E. Alferieff

Shock effects accompanying degradation of a molecular beam

A. A. Morozov, M. Yu. Plotnikov, and A. K. Rebrov

Institute of Thermal Physics, Siberian Branch of the Russian Academy of Sciences, Novosibirsk
(Submitted March 26, 1997)
Pis'ma Zh. Tekh. Fiz. **23**, 16–21 (September 12, 1997)

The relaxation zone of a low-intensity molecular beam in a gas at rest is investigated in detail by Monte Carlo simulation. It is established that the degradation of such beams is accompanied by strong shock effects which are manifested in the formation of zones where the temperature is much higher than that of the background gas. © *1997 American Institute of Physics.* [S1063-7850(97)00409-6]

Dissipation (degradation) of a molecular beam is a typical translational-relaxation process characterized by nonisotropic distribution functions of the molecular velocities and kinetic energy and the temperature. In the case of complete degradation of a beam the initial beam motion of the molecules gives way to radial diffusion from a fictitious source.[1]

No systematic investigations of the beam degradation process have been made in the literature. In the present work we attempted to obtain information about the structure of the entire relaxation zone in the case of complete degradation of a low-intensity beam, for which it can be assumed that the energy relaxation of the beam molecules occurs in a heat bath with constant temperature in space and time. To particularize the analysis of the characteristic features of the relaxation processes, the initial data specified injection of monatomic molecules all with the same velocity.

An efficient tool for solving the problem stated above is direct statistical simulation.[2] The method was modified for the case of a background gas of molecules having a Maxwellian velocity distribution function. The hard-sphere model was adopted for the interaction potential of the molecules. Numerical experiments were performed in a wide range of masses of the injected light ($m_1/m_2<1$) and heavy ($m_1/m_2>1$) molecules. Here m_1 and m_2 are the masses of the injected and background gas molecules, respectively. The parameters of the problem were the mass ratio m_1/m_2 and the velocity ratio $S=u_1/V$, where u_1 is the initial velocity of the injected gas and $V=\sqrt{2kT_2/m_2}$ is the most probable thermal speed of the background gas. The spatial motion of the molecules was tracked in a cylindrical volume with total absorption of the injected molecules at its boundary. Injection was assumed to occur along the axis of the cylinder. The dimensions of the volume were chosen so that the boundaries of the volume would not greatly affect the region of relaxation of the injected molecules. Cylindrical coordinates were introduced in accordance with the geometry of the problem: The z axis is oriented along the injection direction and r is the distance from the axis. Distances were measured in units of the mean free path $l=1/(n\sigma\sqrt{2})$ of a background gas molecule (n is the number density and σ is the collision cross section of the molecules in the background gas) and the velocity and temperature were measured in units of the most probable thermal speed and temperature of the background gas. Depending on the specific formulation of the numerical experiment, the trajectories of 10^6 to 10^7 injected molecules were tracked. The information accumulated about the state of the molecules in the cells was used to determine the density, average mass velocity, energy, and overall temperature and also the components T_z (E_z) and T_r(E_r) of the temperature (energy) of the injected molecules parallel and perpendicular to the axis of the cylinder, respectively. This made it possible to analyze the directional relaxation of momentum, energy, and temperature. A systematic analysis of the directional temperature distribution (kinetic energies of the molecules relative to the average macroscopic velocity) established that the directional temperatures in the relaxation zone can be much higher than the temperature of the background gas and can depend on the parameters of the problem m_1/m_2 and S. The calculations were performed for $m_1/m_2=0.1$–20 and $S=0.5$–10.

To illustrate the structure of the relaxation zone, the isochors of the injected gas for the case $m_1/m_2=1$ and $S=1$ are shown in Fig. 1. A substantial deviation from spherical symmetry occurs inside the region bounded by the 0.08 isochor. According to the calculations, the remnant of the initial δ-function velocity distribution of the injected molecules along the line of injection vanishes toward the boundary of this region. The temperature of the molecules near the line of injection for $S=1$ exhibits a characteristic feature: Its value T_z in the injection direction, on approaching the temperature of the background gas at a distance of 5–10 mean free paths, passes through a diffuse maximum which is 3–4% higher than the temperature of the background gas. The temperature T_r in the radial direction, perpendicular to the line of injection, increases monotonically to the temperature of the background gas. In the case studied the energy of injected molecules was equal to 2/3 of the average energy of the background molecules. If the energy of the injected molecules is higher than that of the background molecules, then a region with temperature higher than the background temperature arises in the relaxation zone, and the temperature in the injection direction is much higher than the overall temperature $T=(T_z+2T_r)/3$. This is clearly seen in Fig. 2a from the computational results for $m_1/m_2=1$ and $S=\sqrt{10}$, which corresponds to a 10 times higher energy of the injected molecules than in the preceding case. The maximum value is $T_z\sim 4.2$. Using the well-known gas-dynamic relations for an adiabatic flow, we shall compare this value to the temperature behind an infinitely strong planar shock wave ($M=\infty$). The Mach number and the temperature behind such a wave

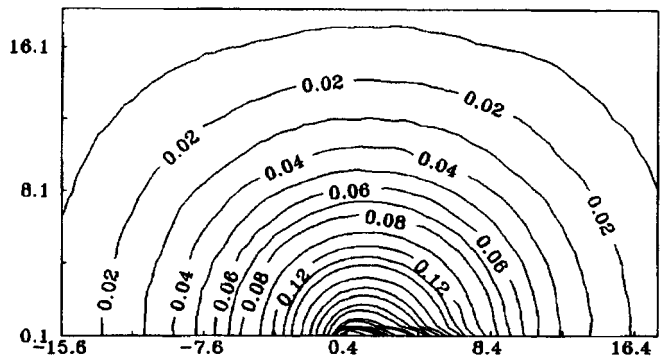

FIG. 1.

are $M=\sqrt{(\gamma-1)/2\gamma}$ and $T=T_0(1+M^2(\gamma-1)/2)$, respectively. From the relation $5/2kT_0=m_1S^2V^2/2$ the stagnation temperature is $T_0=0.4S^2T_2m_1/m_2$. In this case T is given by the expression $T=0.375S^2T_2m_1/m_2$. For $S=\sqrt{10}$ and $m_1/m_2=1$ we obtain $T=0.375T_2$ and $T_0=4T_2$. These values are close to the value obtained in the numerical simulations. The model of stagnation in an infinitely strong shock wave, while sharing certain features of the relaxation process with the case studied in the calculations, cannot claim to give a realistic modeling. For this reason, the quantitative agreement between the temperatures can be interpreted only qualitatively as corresponding to a shock character of the degradation of the beam and of the plane-parallel molecular flow with $M=\infty$ in the shock wave.

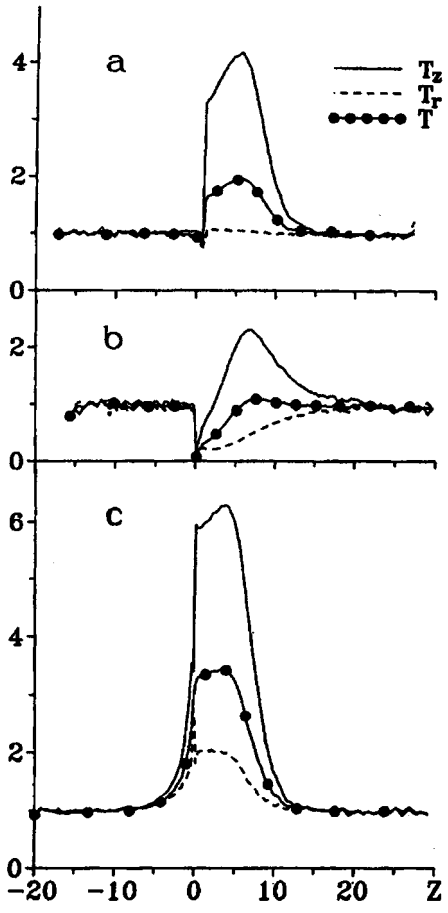

FIG. 2.

The temperature in the radial direction, perpendicular to the line of injection, relaxes quite rapidly to the background gas temperature. For this reason, the fact that at a distance of about 10 mean free paths the overall temperature of the injected gas is higher than the background temperature is due to the energy of motion along the direction of injection.

At a given energy of the injected gas the temperature behind an infinitely strong shock wave, in accordance with the expression $T=0.375S^2T_2m_1/m_2$, remains unchanged. However, for injection of particles with $m_1\neq m_2$ the maximum temperature is substantially different for different values of m_1/m_2. Figure 2b displays the computational results for the case $S=1$ and $m_1/m_2=10$. In this case the relaxation zone becomes more extended, and the maximum temperature along the line of injection is substantially lower (2.3 instead of 4.2). The maximum overall temperature is only slightly higher than the background temperature.

If molecules with a mass of one-tenth the mass of the background molecules are injected at energies corresponding to the latter two cases (Fig. 2c), a similar shock effect is observed, and the maximum temperature T_z is even higher than in the case $m_1=m_2$: $(T_z)_{\max}\sim 6$. Therefore a strong shock effect occurs in all three cases in a range of two orders of magnitude in the mass ratio for a given energy of the molecules.

The following nontrivial conclusions can be drawn from the computational results:

1) When the energy of the injected molecules is higher than that of the background molecules, the shock effect — the increase in the temperature of the injected gas — intensifies as the mass of the injected molecules decreases at a constant energy;

2) If $m_1/m_2>1$, then $(T_z)_{\max}$ is less than the corresponding value for $m_1/m_2=1$ and, conversely, if $m_1/m_2<1$, then $(T_z)_{\max}$ is greater than in the case $m_1/m_2=1$.

In other words, in the case when a heavy gas is scattered in a light one the temperature of the heavy gas does not reach the temperature behind an infinitely strong shock wave; in the case when a light gas is scattered in a heavy one the maximum temperature of the light gas in the direction of injection can be much higher than the temperature behind a shock wave with $M=\infty$.

This work was supported by the Russian Fund for Fundamental Research (Project 95-01-1371).

[1] B. L. Paklin and A. K. Rebrov, Prikl. Mekh. Tekh. Fiz. **36**, 3 (1995).
[2] G. A. Bird, *Molecular Dynamics and the Direct Simulation of Gas Flows*, Clarendon Press, Oxford, 1994.

Translated by M. E. Alferieff

Tunneling contact under the action of a nanosecond voltage pulse

I. A. Dorofeev and V. Ya. Kosyev

Institute of Physics of Microstructures, Russian Academy of Sciences, Nizhniĭ Novgorod
(Submitted March 27, 1997)
Pis'ma Zh. Tekh. Fiz. **23**, 22–27 (September 12, 1997)

The initial stage of current flow through a tunneling gap subjected to a short voltage pulse is examined and the dynamics of the contact between a tip and a sample surface under the action of pulses with durations ranging from 1 μs to 1 s is investigated. © *1997 American Institute of Physics.* [S1063-7850(97)00509-0]

It is well known that local modification of a solid surface can be effected by a pulsed increase in the voltage across a tunneling gap.[1,2] To develop a mechanism for the change in the surface properties of a material it is necessary to have information about the dynamics of the tunneling contact during the action of a voltage pulse. In a number of works, for example, in Refs. 3–5, the behavior of a tunneling contact under the action of pulses ranging in duration from 1 μs to 1 s was investigated experimentally, and it was shown that as the amplitude of the pulses increases, the probability of mechanical contact between the tip and the sample increases. In the present letter we report the results of an experimental investigation of the passage of short pulses ranging in duration from 20 ns to 1 μs through a tunneling contact.

The experimental arrangement is presented in Fig. 1. Square pulses with amplitudes up to 10 V and a $\sim$10 ns rise time from a G5-60 pulse generator *1* were applied directly to a tunneling contact. The pulses were detected (*2* a digital-to-analog converter) with closed tunneling-microscope feedback. A pulsed current flowed through the sample and the tunneling gap and was taken from the input of the preamplifier *3* of the microscope and fed into an rf signal amplifier *4*, which minimized the distortion of the signal shape, matching the resistance of the circuit and coaxial line.

The lower and upper limits of the transmission band of the detecting circuit were determined, respectively, by the frequency of the high-frequency input filter and by the the maximum frequency of the oscillograph. The two-cascade rf power amplifier was based on KP 905 and KP 907 insulated-gate field-effect transistors and had a limiting amplification frequency of 1.5 GHz. The first cascade of the amplifier consisted of a wide-band common-source voltage amplifier. The second cascade, which is not coupled galvanically with the first one, is a source-follower amplifier with a 50 Ω load resistance. The circuit elements were connected with a coaxial cable with a characteristic impedance of 50 Ω.

The following samples were investigated: bulk silver and iron, 500 Å thick chromium and nickel films deposited on a polished silicon surface or glass, carbon–nickel–carbon three-layer structures on a silicon substrate with layer thicknesses 25 Å/30 Å/25 Å and 25 Å/500 Å/25 Å, respectively. The films were deposited by vacuum laser sputtering. Tungsten wire tips, prepared by electrochemical etching in an alkali solution, were used. Prior to the measurements, the bulk metal samples were treated in a 40% solution of hydrofluoric acid and then carefully washed in distilled water. The experiments were performed in air at atmospheric pressure.

The quality of the entire radioelectronic channel was checked as follows. The microscope tip was pressed into a bulk metal sample and then a voltage pulse was applied across this short-circuited contact. The voltage pulse passed through the entire detection system and was recorded on an oscillograph. Oscillogram *1* in Fig. 2 characterizes the quality of the signal which has passed through the short-circuited contact formed by a tungsten tip and the bulk metal sample. An identical signal was observed in the case of a short-circuited contact formed by a tungsten tip and a 500 Å metal film on glass. We note that these pulses were virtually identical to the pulses of the same duration at the output of the generator. The bottom oscillograms show the change in the shape of a pulse passing through a tunneling contact between a tip and a three-layer structure (25 Å/30 Å/25 Å) with $l_t = 1$ nA and $U_t = 0.1$ V (curve *2*) and a short-circuited contact between the tungsten tip and a three-layer structure (curve *3*). All curves are for the same polarity, but for clarity the curves *2* and *3* have been inverted. Comparison of curves *2* and *3* shows that the large changes in shape, duration, and amplitude of a pulse are due not only to the presence of a tunneling gap but can also be affected by the properties of the structure and the substrate. Investigations showed that the silicon substrate (type KDB, resistance 20 mΩ/cm as measured by a contact method) gave the main contribution. We attribute this to electron transport through the Schottky barrier at the metal–semiconductor contact at the location where the sample is fastened to the microscope table and in the tip–sample interaction zone during current flow. Note that the shape and amplitude of the pulse passing through the tunneling contact at given values of U_t and l_t (curve *2*) depends on the location of the tip above the structure and on the parameters of the tip.

In our experiments the probability of mechanical contact between the tip and the sample was observed to increase with the pulse amplitude in the entire experimental range of pulse durations. The contact is apparently due to the thermal expansion of the tip and the sample as a result of heating by the flowing current. In subsequent experiments we measured the time it took for the tip to exceed the tunneling distance or the time over which the resistance of the tunneling contact decreased by several orders of magnitude. We estimated that the resistance of a tunneling contact of tungsten to a three-layer structure, for example, dropped by six orders of magnitude, from 10^8 Ω to 10^2 Ω, including the resistance per

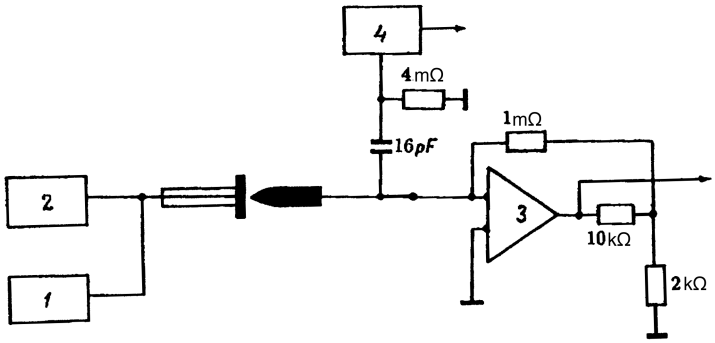

FIG. 1.

unit length of the structure, at the given values of U_t and l_t. This evidently could be judged from the delay of the leading edge of a pulse which has passed through a tunneling contact relative to the leading edge of a pulse which has passed through the short-circuited contact.

An oscillogram of a pulse which has passed through the short-circuited contact of the tungsten tip with a bulk metal sample and an oscillogram of a pulse which has passed through the tunneling contact are presented in Fig. 3a (curves *1* and *2*, respectively). Similar signals obtained with the three-layer structure C (25 Å)/Ni (30 Å)/C (25 Å) are shown in Fig. 3b. In this figure the curves 2 reflect the variance of the delay of the leading edge of a pulse which has passed through the tunneling contact as a function of the location of the tip above the surface under study. In both cases the tunneling contact was formed with $U_t = 0.1$ V and $l_t = 1$ nA. It follows from the experiments performed that the vacuum gap between the tungsten tip and these samples decreases to zero (right up to mechanical contact) over 8–30 ns with $U_t = 0.1$ V and $l_t = 1$ nA. Here we shall not discuss in detail the question of what constitutes a microscopic mechanical contact, but according to our measurements its linear size is of the order of or less than the electron mean-free path length if the action was accomplished by pulses with an amplitude of several volts.

We note that the delay of a pulse which has passed through a tunneling contact increases with the tip–sample distance, specifically, as U_t increases.

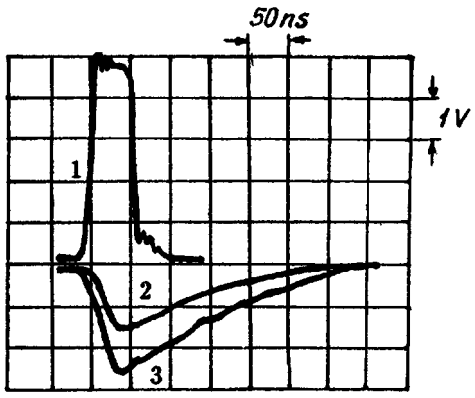

FIG. 2.

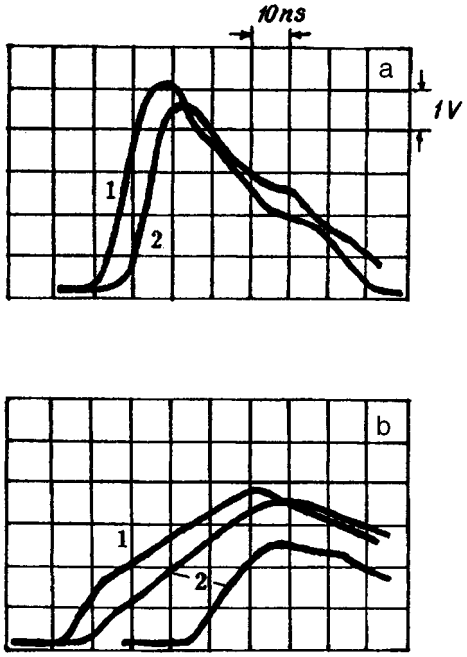

FIG. 3.

In summary, in the present work we investigated the initial stage of current flow through a tunneling gap under the action of a short pulse. The current through the tunneling contact increases rapidly with increasing voltage across the tunneling gap. This increases the heating occurring in the tip and in the sample. For tip and sample at low (room) temperatures, heating is due mainly to the Nottingham effect. Joule heating starts to dominate at temperatures near the inversion temperature of the Nottingham effect. An increase in temperature is inevitably accompanied by expansion of the materials, a decrease in the tunneling gap, and a further increase in the current with additional heating of both the tip and the sample. The process thereby acquires the character of a thermal deformation instability, whose development time we recorded in our experiments. Comparing the oscillograms of signals which have passed through the short-circuited contact shows that after the gap is short-circuited the potential on the tip increases to practically the same value as the potential on the sample. A part of the voltage evidently falls across the thin film, whose impedance is high for the high-frequency components of short pulses with short rise times. It should be noted that the initial tip–sample distance, determined by the values of U_t and l_t, is also determined by the emission characteristics of the surface of different samples, even when the same tip is used. For this reason, in our case the initial tunneling gap width, like the gap closure time, will be different for different samples.

This work was supported in part by the Russian Fund for Fundamental Research.

[1] H. J. Guntherodt and R. Weisendanger, *Scanning Tunneling Microscopy I, II, III*, Berlin, 1992.
[2] G. G. Vladimirov and A. A. Gryazev, Vestnik SbPGU, Ser. 4, No. 1, 24 (1993).

[3] C. S. Chang, W. B. Wu, and T. Tsong Tien, Phys. Rev. Lett. **72**, 574 (1994).
[4] G. G. Vladimirov, A. V. Drozdov, and A. N. Rezanov, Pis'ma Zh. Tekh. Fiz. **22**(18), 67 (1996) [Tech. Phys. Lett. **22**, 764 (1996)].
[5] I. A. Dorofeev, V. Ya. Kosyev, and A. A. Petrukhin, Pis'ma Zh. Tekh. Fiz. **22**(23), 30 (1996) [Tech. Phys. Lett. **22**, 962 (1996)].

Translated by M. E. Alferieff

Photoconducting properties of sillenites grown in an oxygen-free atmosphere

Yu. B. Afanas'ev, V. V. Kulikov, E. V. Mokrushina, A. A. Petrov, and I. A. Sokolov

A. F. Ioffe Physicotechnical Institute, Russian Academy of Sciences, St. Petersburg
(Submitted April 23, 1997)
Pis'ma Zh. Tekh. Fiz. **23**, 28–33 (September 12, 1997)

Crystals with the sillenite structure, grown in an oxygen-free (argon) atmosphere, are investigated by the ac photovoltage method. It is found that the photoconductivity in red light is sharply higher (by two orders of magnitude) than in crystals grown in the presence of oxygen. Such crystals can be used in interferometric devices. © *1997 American Institute of Physics.* [S1063-7850(97)00609-5]

Crystals with sillenite structure possess a complicated system of energy levels[1] that depends on many factors. Specifically, the properties of the crystals can be altered by lightly doping them with different elements. In the present work we investigated samples of bismuth silicate and titanate ($Bi_{12}SiO_{20}$ and $Bi_{12}TiO_{20}$) crystals grown in an argon atmosphere.[2]

The parameters of the crystals were determined by the ac photovoltage method.[3–5] In this method a sample is exposed to an interference pattern produced by two mutually coherent light beams, one of which is phase-modulated with frequency ω, and the ac component J_ω of the current flowing through the sample is measured. Measurements of the frequency dependence $J_\omega(\omega)$ makes it possible to determine parameters of the material, such as the photoconductivity and the lifetime of photoinduced charge carriers, as well as to calculate some other quantities. As was shown in Refs. 4 and 5, the maximum amplitude $|J_\omega|_{\max}$ of the current and the form of the reduced function $J'_\omega=|J_\omega|/|J_\omega|_{\max}$ are given by the expressions

$$|J_\omega|_{\max}=\frac{S\Delta\sigma_0 E_d}{2p}m^2, \tag{1}$$

$$J'_\omega=\frac{\omega' q}{\sqrt{[1+(\omega')^2]^2+(\omega')^2 q}}, \tag{2}$$

where S is the area of the electrodes, Δ is the amplitude of the phase modulation of the light, σ_0 is the average specific photoconductivity, $E_d=K\times kT/e$ is the diffusion field, k is Boltzmann's constant, T is the absolute temperature, e is the electron charge, $K=2\pi/\Lambda$, Λ is the period of the interference pattern, m is the contrast of the interference pattern, $\omega'=\omega/\omega_m$, $|J_{\omega(\omega_m)}|=|J_\omega|_{\max}$, and p and q are dimensionless quantities that depend on the parameters of the material and the value of K.

The expression (19) of Ref. 5, which takes account of the dependence of the material parameters on the light intensity (single-level model approximation), yields

$$\omega_m^2=\frac{1}{\tau\tau_M}\left(1+\frac{\tau+\tau_M K^2 L_d^2}{\tau_I}\right), \tag{3}$$

$$q=\frac{1}{\omega_m}\left(\frac{1}{\tau_M}+\frac{1+K^2L_d^2}{\tau}+\frac{1}{\tau_I}\right), \tag{4}$$

$$p=q\,\omega_m\omega_m^2\tau^2\tau_M, \tag{5}$$

where τ is the lifetime of the photoinduced charge carriers, τ_M is the Maxwellian relaxation time, τ_I is the lifetime of the photoionized state of the donor, and L_d is the diffusion length of the photoinduced charge carriers. The quantity q determines the form of the function $J'_\omega(\omega')$: As q increases, the pronounced maximum transforms into a wide shelf (see Fig. 1).

In the limit $\tau_I\to\infty$ expressions (3)–(5) correspond to a simplified formula for J_ω (Ref. 4) that neglects the dependence of the material parameters on the light intensity.

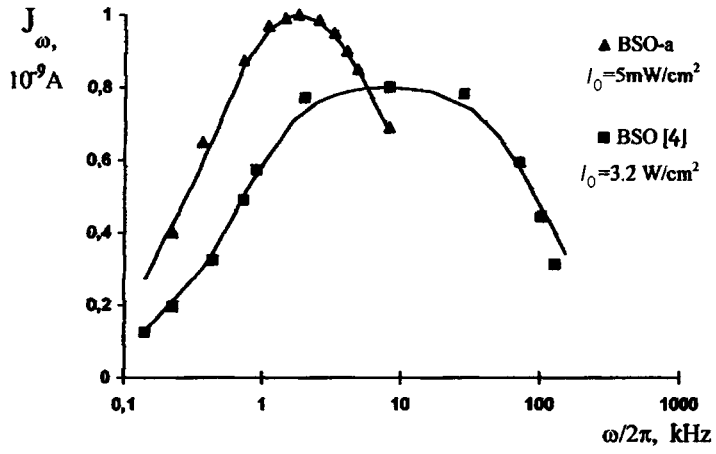

FIG. 1. Comparison of the frequency dependences of the ac photovoltage signal for $\lambda=0.63$ μm and $K=0.5$ μm^{-1} in bismuth silicate crystals grown in oxygen-free and ordinary atmospheres. (BSO-a: $S=0.15$ cm^2, $m=0.67$, $\Delta=0.2$; BSO (Ref. 3): $S=0.04$ cm^2, $m=0.9$, $\Delta=0.1$). The solid lines are theoretical curves calculated from Eq. (2) with $q=3.5$ and 9.0, respectively.

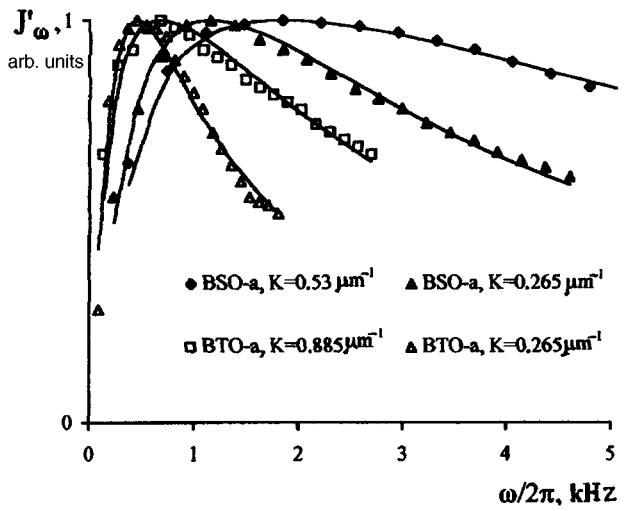

FIG. 2. Frequency dependences of the reduced photovoltage signal for both experimental samples with different values of the spatial frequency. The solid lines are theoretical curves calculated with $q=3.52$ and 2.75 for BSO-a and $q=3.2$ and 2.3 for BTO-a (q increases with K).

In the present work we investigated two samples with the approximate dimensions $5\times5\times5$ mm (BSO-a and BTO-a). The samples were prepared from $Bi_{12}SiO_{20}$ and $Bi_{12}TiO_{20}$ crystals, respectively, grown in an argon atmosphere. Two parallel faces of each sample were polished, and 0.25 cm^2 electrodes were deposited on the other two parallel faces. A He–Ne laser ($\lambda=0.63$ μm) with an output power of 1.8 mW was used in the experiments. One of the beams that produce the interference pattern on the surface of the crystal was phase-modulated with an amplitude of 0.2 rad by a ML-102 electrooptic modulator. A NE 4–56 spectrum analyzer with a 3 Hz band was used to measure the frequency dependence of the photovoltage signal. The total light intensity on the crystal was $I_0=5$ mW/cm^2.

The experimental values of $|J_\omega|_{\max}$ with $K=0.265$ μm^{-1} and $m=0.67$ for BSO-a and BTO-a were equal to 1.0×10^{-3} μA and 0.2×10^{-3} μA, respectively. It should be noted that under such weak illumination with red light ($\lambda=0.63$ μm) an ac photovoltage signal is not observed at all in sillenites grown in an ordinary atmosphere. A light intensity $I_0=3.3$ W/cm^2 was required to obtain a signal of the same magnitude in the standard BSO crystal with $\lambda=0.63$ μm and $K=0.5$ μm^{-4} (Ref. 4). The curves displayed in Fig. 1 were obtained for BSO-a and standard bismuth silicate with illuminations giving comparable maximum values of the signal for the two crystals.

Figure 2 displays curves of J'_ω, measured for the BSO-a and BTO-a samples for two different values of K, versus frequency. The solid lines are theoretical curves calculated from Eq. (2). The values of ω_m were determined directly from measurements; q was used as an adjustable parameter to obtain the best fit of the theoretical curves to the experimental data.

The values obtained for ω_m and q for two different spatial frequencies enabled us to obtain, using expressions (3) and (4) as a system, the values of all four characteristics of the material which are engaged in this process (τ, τ_M, τ_I, and I_d). Knowing these parameters and using the well-known relations $\tau=1/\gamma N_I$, $\tau_M=\varepsilon\varepsilon_0/e\mu\tau g_0$, $\tau_I=1/\gamma\tau g_0$, and $L_d=(\mu\tau E_d K)^{1/2}$ (here g_0 is the density of charge carriers excited by light per unit time), it is also possible to estimate the mobility μ of the photoinduced charge carriers, the volume density N_I of the free traps, the probability γ of trapping of free charge carriers by a trap, and the quantum yield β, which shows the fraction of the absorbed light expended on photoexcitation. We used the well-known value of the dielectric constant for sillenites $\varepsilon=56$ and the directly measured values of the absorption coefficient α. The computational results are presented in Table I. For comparison, the parameters of standard BSO which were obtained on the basis of the data in Ref. 4 are also given in Table I. The values of α and N_I are taken from Ref. 6 and the value of β is taken from Ref. 7.

It should be noted that this computational method employs only the reduced functions $J'_\omega(\omega')$, so that the experimental values of the maximum photovoltage signal constitute independent information. For comparison, the quantities $|J_\omega|_{\max}$ were calculated from expressions (1) and (5) using the parameters presented in Table I. The values obtained for BSO-a and BTO-a are, respectively, 1.3×10^{-3} and 0.16×10^{-3} μA, in good agreement with the experimental data. On the other hand, expressions (3)–(5) neglect the complicated structure of the energy levels of the material. According to the data obtained, for BTO-a $\tau>\tau_I$, which cannot be explained in a single-level model.

As one can see from Table I, the values obtained for the carrier mobility and the probability of carrier trapping by a trap in BSO-a and BTO-a crystals do not differ much from the corresponding values for standard BSO. At the same time, the density of free traps is found to be more than two orders of magnitude lower and, correspondingly, the lifetime and diffusion length of photoinduced charge carriers are higher. Furthermore, these crystals exhibit somewhat higher absorption and, importantly, a higher quantum yield. As a result, in respect to the photoconductivity coefficient σ_0/I_0

TABLE I. Parameters of sillenites grown in an oxygen-free atmosphere (BSO-a and BTO-a) compared with the parameters of an ordinary BSO crystal.

	τ, ms	τ_M, ms	τ_I, ms	L_d, μm	μ, $cm^2/V\cdot s$	β	N_I, cm^{-3}	γ, cm^3/s	α, cm^{-1}
BSO-a	0.15	0.4	0.3	3.86	0.04	0.9	3×10^{12}	2×10^{-9}	0.9
BSO[3,6,7]	0.003	0.2*	1.4*	0.6	0.05	0.1	0.8×10^{15}	4×10^{-10}	0.4
BTO-a	3	0.25	0.7	5.8	0.004	0.5	7×10^{12}	4.5×10^{-11}	1.4

*Values corresponding to illumination intensity $I_0=3.2$ W/cm^2.

in red light the argon sillenites are closer to semiconductor crystals[8] than to ordinary sillenites.

A sharp increase in photocurrent in vacuum-annealed sillenites in the red region of the spectrum has been observed previously.[1] This was attributed to the compensation of traps by donor centers bound with oxygen vacancies which arise during annealing. The results of our work confirm this conclusion, and they yield the first quantitative estimate of the properties of photocarriers in sillenites with nonstoichiometric oxygen contents. Such crystals can probably be used successfully in adaptive interferometers based on the ac photovoltaic effect.[9,1]

[1] O. A. Gudaev, V. A. Gusev, V. A. Detinenko, A. P. Eliseev, and V. K. Malinovskiĭ, Avtometriya, No. 5, 38 (1981).

[2] V. I. Berezkin, A. A. Petrov, Yu. B. Afanas'ev, and I. V. Mikheev, in *Proceedings of the All-Union Conference on Growing Crystals by Stepanov's Method* [in Russian], March 1985, Leningrad, pp. 148–152.

[3] M. P. Petrov, L. A. Sokolov, S. I. Stepanov, and G. S. Trofimov, J. Appl. Phys. **68**, 2216 (1990).

[4] I. A. Sokolov and S. I. Stepanov, Electron. Lett. **26**, 1275 (1990).

[5] I. A. Sokolov and S. I. Stepanov, Optik **93**, 175 (1993).

[6] E. V. Mokrushina, A. A. Nechitailov, and V. V. Prokofiev, Opt. Comm. **123**, 592 (1996).

[7] R. Grousson, M. Henry, and S. Mallick, J. Appl. Phys. **56**, 224 (1984).

[8] S. I. Stepanov, I. A. Sokolov, G. S. Trofimov, V. I. Vlad *et al.*, Opt. Lett. **15**, 1239 (1990).

[9] I. A. Sokolov, V. V. Khorenko, and S. I. Stepanov, Ferroelectrics **160**, 317 (1994).

[10] D. M. Pepper, G. J. Dunning, Y. Owechko, R. A. Cronkite *et al.*, *Proc. CLEO'96*, 1996, p. 352.

Translated by M. E. Alferieff

Possibility of quasicontinuous measurement of the evolution of the electron temperature of a plasma by the Thomson scattering method

M. Yu. Kantor

A. F. Ioffe Physicotechnical Institute, Russian Academy of Sciences, St. Petersburg
(Submitted May 22, 1997)
Pis'ma Zh. Tekh. Fiz. **23**, 34–40 (September 12, 1997)

A method is proposed for increasing the frequency of Thomson scattering measurements of the electron temperature of a plasma to 100 kHz. The approach makes it possible to raise the diagnostic sensitivity under stationary discharge conditions by three orders of magnitude. The possibilities of the method are confirmed experimentally. © *1997 American Institute of Physics.* [S1063-7850(97)00709-X]

1. INTRODUCTION

In plasma investigations it is necessary to make repeated measurements of the electron temperature with a high repetition rate. This requirement arises in the study of fast transient processes in the plasma of large tokamaks (for example, the L–H transition, internal disruptions), in measurements performed in plasma systems with a short discharge time, as well as in a number of diagnostic methods. The main obstacle to performing such measurements by the Thomson scattering method is the lack of suitable multipulse probe lasers. The development of Thomson diagnostics in this area might involve the use of the free-lasing mode in a laser with a high pulse repetition rate. In addition, the radiation energy is also much higher in the free-lasing mode than in a Q-switched mode because of lower cavity losses and higher admissible radiation energy density on the optical components.

2. FREE-LASING MODE OF A PROBE LASER

These advantages of Thomson scattering can be realized through the use of in-cavity and multipass laser probing of the plasma.[1,2] Figure 1 displays an optical diagram of the proposed system. The active element *3* is placed in a cavity formed by a nontransmitting mirror *1* and a multipass system consisting of two concave mirrors *5, 6* and a focusing lens *4*. The tokamak chamber *7* is located between the mirrors of the multipass system. An objective *2* consisting of positive and negative lenses serves to decrease the divergence of the laser beam.

The laser radiation in free lasing is chaotic. However, the average radiation intensity I and the pulse repetition frequency ν are determined by the pump and the properties of the cavity and the active element (see, for example, Ref. 3). The radiation energy density per pulse is determined as $\omega_P = I/\nu$. These quantities show good shot-to-shot reproducibility. For a three-level laser they are given by

$$I=(\omega_S/\tau_S)^*(P-1)^*\alpha/\gamma, \quad \nu=(\alpha(P-1)/2\tau_S\tau_R)^{1/2}/\pi,$$
$$\omega_P=(\pi\omega_S/\gamma)^*(2\tau_R(P-1)\alpha/\tau_S)^{1/2}, \quad \alpha=\sigma N_{\mathrm{Cr}} l. \quad (1)$$

Here ω_S is the saturation energy density of ruby, τ_S is the lifetime of the upper laser level, P is the excess of the pump power above threshold, N_{Cr} is the Cr-ion density in the crystal, l is the length of the active element, γ represents the total logarithmic loss of radiation in the cavity, and τ_R is the round-trip time through the cavity. The analogous quantities for a four-level laser assume the form

$$I=(\omega_S/\tau_S)^*(P-1); \quad \nu=(\gamma(P-1)/2\tau_S\tau_R)^{1/2}/\pi;$$
$$\omega_P=\pi\omega_S(2\tau_R(P-1)/\tau_S\gamma)^{1/2}. \quad (2)$$

The intensity of the radiation in an individual free-lasing pulse is 3 to 10 times higher than the average level. After leaving the active element the radiation is intensified in the multipass system. If the logarithmic loss upon N passes of the beam between the mirrors *5* and *6* equals γ_{MPS}, then the radiation gain is

$$N_{\mathrm{eff}}=(1-\exp(-\gamma_{MPS}))/(1-\exp(-\gamma_{MPS}/N)). \quad (3)$$

Let us estimate the parameters of the radiation in this system for a typical ruby laser with $\alpha=10$, $P=4$, lasing duration 2 ms, and aperture of the active element 2 cm^2. For 30 passes of the beam and $\gamma=0.5$, the radiation gain is $N_{\mathrm{eff}}=24$. For a mirror separation of 2 m the round-trip time τ_R equals approximately 200 ns. In this case the average probe power will be 2.8 MW: The pulse repetition frequency equals 50 kHz and the energy per pulse is 58 J. Such radiation parameters make it possible to use the free-lasing mode in the Thomson diagnostics of plasmas.

3. EXPERIMENTAL RESULTS

The method was checked using a probe system consisting of a ruby rod 240 mm long and a multipass system consisting of two mirrors 120 mm in diameter and with a radius of curvature of 1000 mm.[2] The surfaces of all the optical elements except for the end faces of the ruby were coated with an antireflection coating. Since there is no information about the resistance of this crystal to radiation damage in the free-lasing mode, the intensity of the radiation in the active element was limited to a level known to be safe: 1 MW/cm^2. For high-quality elements this limitation can be removed.

The radiation loss in the cavity was equal to 33%, neglecting scattering in the ruby and losses in the multipass system. The latter losses have a large effect on the probe efficiency. For this reason, lasing in the case of low and high losses in the multipass system was studied in this work. In the first case, less than 1% of the radiation was absorbed per

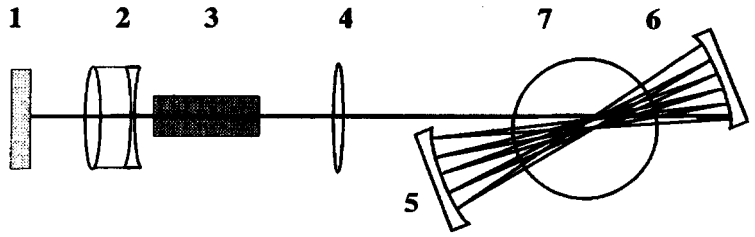

FIG. 1. Optical-laser probing scheme. *1* — 100% mirror, *2* — correcting objective, *3* — active element, *4* — focusing lens, *5*, *6* — mirrors of the multipass system, *7* — plasma.

pass between the mirrors. This made it possible for up to 80% of the radiation to return into the active element upon 30 passes of the beam and to increase the probe energy by a factor of 25 ($N_{\text{eff}}=25$).[2] For 4% losses, after 24 passes one-third of the radiation returned from the multipass system, and N_{eff} was equal to 15.

Figures 2 and 3 show lasing under these conditions. The lasing parameters agree well with the estimates (1). The pulse repetition frequency is close to 30 kHz in both cases. The probe energy per pulse equals approximately 50 J in the first case and decreases to 25 J in the second case. The total probe energy was equal to 3200 and 1500 J, respectively. In the case of high radiation losses, the pump level had to be increased by 80%.

Despite the fact that the probe system was not adequately optimized for the free-lasing mode, high parameters of the probe radiation were obtained in the experiments. Extrapolation of the experimental curve of the lasing parameters versus the pump energy shows that removing the restriction on the beam intensity would increase the probe energy to 7 kJ and the pulse repetition frequency to 50 kHz. Optimization of the system would make it possible to increase the energy in an individual pulse to 100 J and the repetition frequency to 100 kHz. For a wide range of problems in plasma physics, this means that it would be possible to perform quasicontinuous measurements of the electron temperature.

4. ERROR IN THE MEASUREMENT OF THE ELECTRON TEMPERATURE

As one can see, the probe energy in an individual laser pulse is an order of magnitude higher than in the standard Thomson diagnostics systems. However, the probe power is an order of magnitude lower than the typical values. For this reason the probe power (together with the photodetectors that are employed for detecting the scattered light) largely determines the error in the temperature measurements.

Photomultipliers are employed when a ruby laser is used for probing a plasma. In this case the error in measuring the temperature depends mainly on the average number N_S of photons collected in the spectral channel, the quantum yield η of the photomultiplier, and the ratio K of the background plasma emission to the scattered radiation flux:

$$\delta T/T \sim ((1+2K)/\eta N_S)^{1/2}. \tag{4}$$

In this region of the spectrum the plasma emission will be of the same order of magnitude as the scattered radiation with a probe power of 10 MW. If the transmission of the radiation collection system equals 25%, then with a density of 3×10^{13} cm^{-3} and a 50 J laser pulse 3×10^5 photons will be collected in the scattering spectrum from a 1 cm^3 plasma volume into a solid angle of 0.003 sr. Model calculations show that when using a photomultiplier with a S20 photocathode, whose quantum yield varies from 3 to 10% in the range from 700 to 600 nm, the error in measuring the tem-

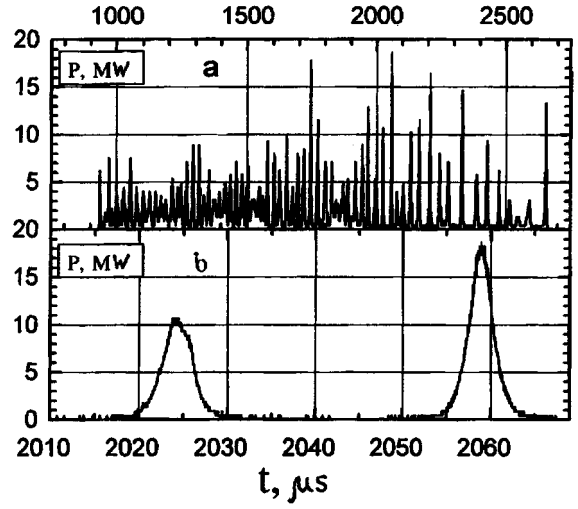

FIG. 2. Lasing of a laser with low radiation loss in the multipass system. a — General form, b — characteristic pulses $U_{\text{pump}}=3.6$ kV.

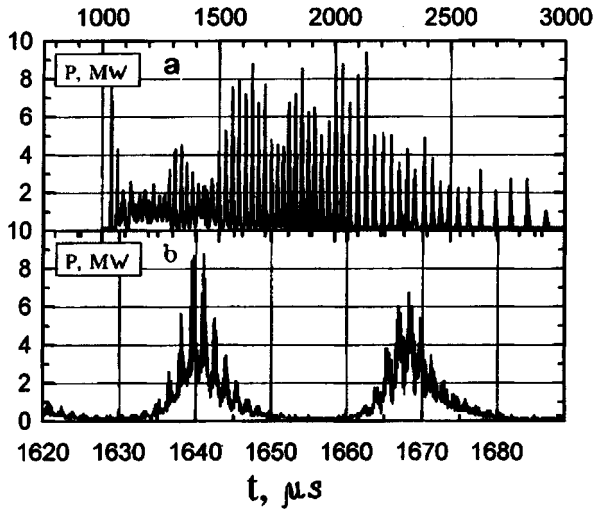

FIG. 3. Lasing of a laser with high radiation loss in the multipass system. a — General form, b — characteristic pulses $U_{\text{pump}}=4.8$ kV.

perature will be 5% at a background radiation level of the plasma $K=1$. As the plasma emission changes, the error in the measurements changes according to Eq. (4), remaining at the 10% level even when the background is ten times stronger than the scattering signal.

When a neodymium-activated glass laser is used for probing a plasma, avalanche multipliers with a high quantum efficiency in the infrared region of the spectrum are employed to detect the scattered radiation. In contrast to photomultipliers, they exhibit an appreciable internal noise of the order of 10^{-13} W/(Hz)$^{1/2}$. When detecting microsecond scattering signals in a frequency band of several megahertz, the sensitivity of the avalanche diodes equals several thousands of photons per microsecond. This limits the application of a neodymium laser at low plasma density, despite the weak level of the plasma emission in the infrared region. At high density this laser will have definite advantages because the conversion of pump energy into radiation is much more efficient.

The proposed system opens up new possibilities for the Thomson scattering method, chief among which is the possibility of carrying out a detailed study of fast transient processes in plasmas. Under steady-state discharge conditions, with the scattered signals accumulated over the free-lasing time of the laser, the new system increases the diagnostic sensitivity by approximately three orders of magnitude. When periodic-pulse pumping of the laser is used, one can add to these possibilities that of making measurements of the evolution of the electron temperature of a plasma over a long time scale at a repetition frequency of tens of hertz.

This work was supported by the Russian Fund for Fundamental Research (Grant No. 97-02-18084).

[1] M. Yu. Kantor, D. V. Kouprienko *et al.*, *23rd EPS Conference on Controlled Fusion and Plasma Physics*, Kiev, 1996, Vol. III, p. 1100.
[2] M. Yu. Kantor and D. V. Kuprienko, Pis'ma Zh. Tekh. Fiz. **23**(8), 65 (1997) [Tech. Phys. Lett. **27**, 321 (1997)].
[3] O. Svelto, *Principles of Lasers*, Plenum Press, New York, 1976 [Russian translation, Mir, Moscow, 1979].

Translated by M. E. Alferieff

Effect of spatial modulation of the interference pattern on the output characteristics of holograms in optically active piezoelectric crystals

A. A. Firsov and V. V. Shepelevich

Mozyr' State Pedagogical Institute
(Submitted March 18, 1997)
Pis'ma Zh. Tekh. Fiz. **23**, 41–47 (September 12, 1997)

The effect of optical activity, the piezoelectric effect, and energy redistribution between light beams on the visibility of an interference pattern is investigated in the case of a two-wave interaction in an optically active cubic piezoelectric crystal. It is shown that the modulation of the visibility of the holographic grating substantially changes the output characteristics of a hologram. © *1997 American Institute of Physics.* [S1063-7850(97)00809-4]

Cubic photorefractive crystals of the type $Bi_{12}SiO_{20}$ (BSO) are distinguished by high photosensitivity, good optical quality, and reversibility of the information writing process.[1] One of the most important applications of such crystals is for intensifying a signal light beam at the expense of a pump beam during the mutual transformation of these beams on the dynamic holographic grating formed.

Our objective in the present work was to investigate the effect of optical activity, the piezoelectric effect, and energy redistribution between light beams propagating through a crystal on the modulation coefficient of the recorded holographic grating and on the output characteristics of the holograms that are produced.

We shall employ a steady-state model of linear generation and recombination of charge carriers.[1] We shall assume that the writing occurs in the diffusion regime and we shall neglect thermal excitation. Then the modulation coefficient will equal the visibility of the interference pattern.[1] The change in the modulation coefficient of the grating is taken into account in the numerical solution of the system of coupled-wave equations.[2]

Let the light beams R and S which are incident on the crystal be linearly polarized in a direction perpendicular to the plane of incidence and let the transmitting holographic grating be untilted. The vector of the holographic grating is assumed to lie in the plane of the (110) crystal cut and to make an angle θ with the crystal direction [001]. The constants which are employed for the BSO crystal in this work can be found in Ref. 2.

Plots of the visibility V of the interference pattern versus the crystal thickness d for $\theta=55°$ and Bragg angle $\varphi=4°$ are displayed in Fig. 1. Curves *1* and *2* in Figs. 1a and 1b do not take into account the effect of energy redistribution in the light beams. Curve *1* was obtained assuming a fixed grating and curve *2* takes into account the effect of optical activity in the formation of the grating, as is manifested in the appearance of a periodic modulation of the grating visibility with a spatial period equal to a 180° rotation of the plane of polarization. Curves *3–6* were constructed with allowance for the effect of energy redistribution in the light beams.

Since in Fig. 1a the initial intensities of the light beams are the same, when energy exchange is taken into account the visibility, on average, decreases with increasing crystal thickness. Also, when the optical activity is neglected the piezoelectric effect in the given case decreases the energy exchange (curve *5* compared to curve *6*). Taking into account the piezoelectric effect together with the optical activity (the latter making it possible to obtain a result averaged over different polarizations on account of the rotation of the plane of polarization by the crystal) gives very large energy exchange when the light beams incident on the crystal have a polarization $\psi=90°$ and an angle $\theta=55°$, and hence it leads to very low values of the grating visibility V (curve *4*).

The effects described above are even stronger when the

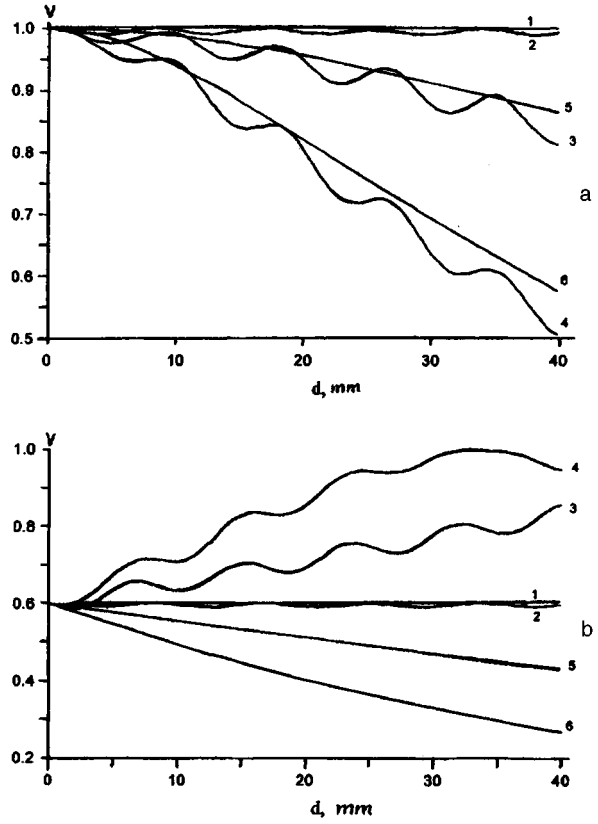

FIG. 1. Curves of the visibility of the interference pattern versus crystal thickness for different ratios of the initial intensities (I_{R_0}/I_{S_0}) of the incident light beams. a) $I_{R_0}/I_{S_0}=1$; b) $I_{R_0}/I_{S_0}=9$; *1, 5, 6* — without optical activity ($\alpha=0.372$ rad/mm); *2, 3, 4* — with optical activity; *1, 2, 3, 6* — without the piezoelectric effect; *4, 5* — with the piezoelectric effect.

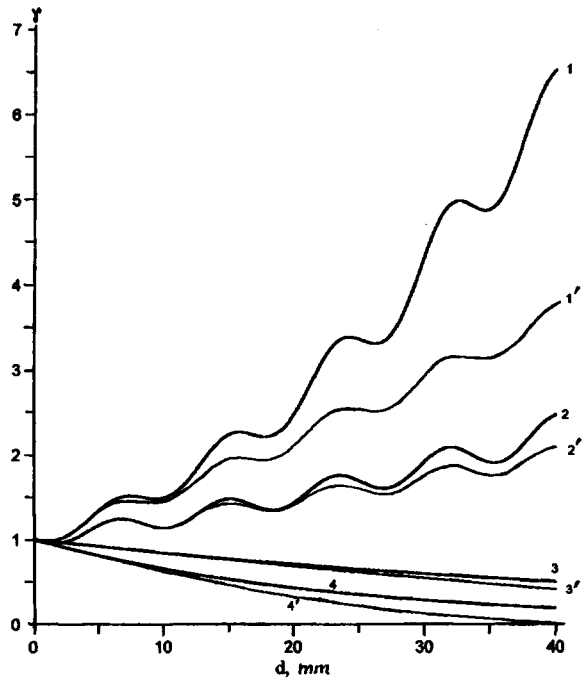

FIG. 2. Relative intensity γ of the signal light beam versus the crystal thickness d. $I_{R_0}/I_{S_0}=9$. *1, 1′* — with optical activity and the piezoelectric effect; *2, 2′* — with optical activity but without the piezoelectric effect; *3, 3′* — without optical activity but with the piezoelectric effect; *4, 4′* — without optical activity and without the piezoelectric effect.

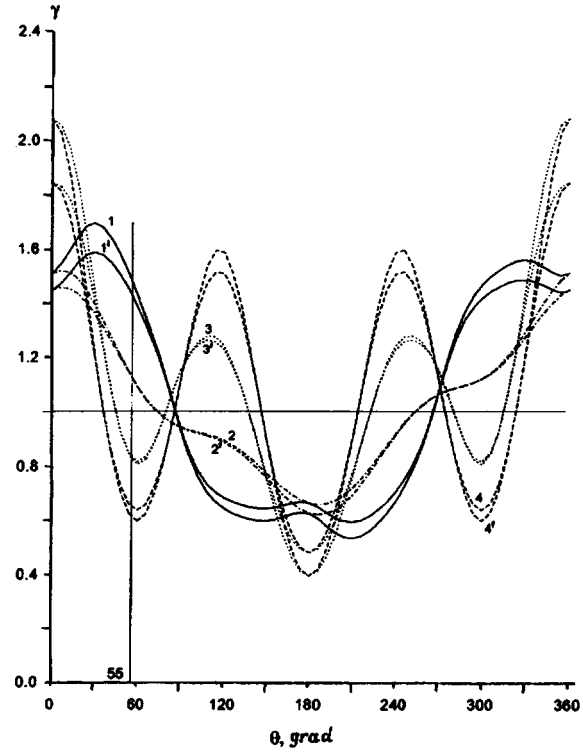

FIG. 3. Relative intensity γ of the signal light beam versus the angle θ; *1, 1′* — with optical activity and the piezoelectric effect; *2, 2′* — with optical activity but without the piezoelectric effect; *3, 3′* — without optical activity but with the piezoelectric effect; *4, 4′* — without optical activity and without the piezoelectric effect.

interacting waves have different initial intensities (Fig. 1b). Since energy transfer is directed in this case on the average (averaging with respect to polarization) from the R wave to the S wave, optical activity leads to a physical realization of a mechanism of such averaging (on account of the rotation of the plane of polarization). For this reason, curves *4* and *3* in Fig. 1b are characterized by an increase in visibility. For crystal thickness $d\approx 35$ mm the intensities of the R and S waves become equal ($V=1$), and once again the visibility starts to decrease, $I_S>I_R$. If optical activity is neglected, then energy transfer is directed from the S wave to the R wave. For this reason, the visibility decreases with increasing crystal thickness. In this case, just as Fig. 1a, if the optical activity is neglected, the piezoelectric effect decreases the energy transfer.

Curves of the relative intensity $\gamma=I_S/I_S^0$ of the signal light beam S as a function of the crystal thickness with $\theta=55°$ and Bragg angle $\varphi=4°$ are presented in Fig. 2. Here I_S^0 is the intensity of light beam S on exit from the crystal when the grating has not yet been recorded, and I_S is the intensity of light beam S on exit from the crystal after the writing process has reached a stationary state. The curves were constructed with allowance for the reflection of the light beams at the boundaries of the crystal. The curves drawn with a heavy line represent the relative intensities with allowance for the effect of the redistribution of energy between the light beams on the visibility of the interference pattern. The fine lines show the relative intensities obtained in the fixed-grating approximation. It is evident from this figure that in the absence of optical activity (plots *3, 3′* and *4, 4′*) a small decrease of the relative intensity of the S wave occurs (energy is pumped into the R wave). Switching on the optical activity changes the direction of energy transfer, and the intensity of the S wave increases severalfold. Here, as in Fig. 1b, the averaging of the different polarization states of the interacting waves plays the main role. A sharp intensification of energy transfer occurs as a result of the presence of energetically favorable polarization states of the R and S waves with energy transfer directed from the R wave to the S wave. In the process of averaging over the thickness of the crystal, these states make the main contribution to the resulting curves $\gamma(d)$. It should be noted that the piezoelectric effect in this case plays a large role, more than doubling the value of $\gamma(d)$.

Here we are dealing with an interesting effect wherein optical activity is transformed from a standard minor ''noise'' factor into a factor capable of sharply improving the important energy characteristics of a holographic device.

Since we have examined only one orientation of the holographic grating ($\theta=55°$), it is of interest to analyze the function $\gamma(\theta)$ with a fixed thickness of the crystal (Fig. 3). Here the curves of the relative intensities γ of the signal light beam versus the angle θ for Bragg angle $\varphi=4°$, crystal thickness $d=10$ mm, and $I_{R_0}/I_{S_0}=9$ are shown. The curves labeled with primed numbers were constructed in the fixed-grating approximation and the curves labeled with unprimed numbers were constructed with allowance for the effect of energy redistribution between the light waves on the visibil-

ity of the interference pattern. The values of the energy transfer which correspond to $\theta = 55°$ are indicated by a vertical straight line. It is evident from this figure that the optical activity of the crystal substantially increases the intensification of the signal light wave not only for $\theta = 55°$ but also for many other angles θ.

In summary, the intensification of a signal light wave at the expense of the energy of a reference wave in a definite range of orientations of the grating vector for certain fixed polarizations of the interacting waves can be substantially increased when the optical activity of the crystal is taken into account. Taking into account the energy redistribution occurring between the light waves during the writing process in the case of a thick crystal can almost double the intensification of the light waves.

We are grateful to the Ministry of Education of the Republic of Belarus for financial support.

[1] T. J. Hall, R. Jaura, L. M. Connors, and P. D. Foote, Progr. Quantum Electron. **10**, 77 (1985).
[2] V. V. Shepelevich, N. N. Egorov, and Victor Shepelevich, J. Opt. Soc. Am. B **11**, 1394 (1994).

Translated by M. E. Alferieff

ActiveX control for a semiconductor plate in a waveguide

E. O. Popov and S. O. Popov

A. F. Ioffe Physicotechnical Institute, Russian Academy of Sciences, St. Petersburg
(Submitted May 15, 1997)
Pis'ma Zh. Tekh. Fiz. **23**, 48–56 (September 12, 1997)

The scattering of electromagnetic waves by a thin semiconductor plate placed at the center of the transverse cross section of a rectangular waveguide is studied. The relation between the electrodynamic parameters (reflection, absorption, and transmission coefficients) and the characteristics of the semiconductor material (carrier density, carrier mobility, and scattering time) is determined. The idea of the visual library, physical ActiveX (p-ActiveX), for modeling of physical processes is set forth. A description of this library is presented for a wide range of workers engaged in the development of microwave devices with a semiconductor plate as the active element, and a computer file containing this library is provided.(The names ActiveX and Windows are registered trademarks of the Microsoft Corporation.) [S1063-7850(97)00909-9]

1. INTRODUCTION

Investigations of the microwave characteristics of semiconductors, such as the density, lifetime, and scattering time of the charges, at microwave frequencies have the advantage over dc measurements that they can be performed by a contactless method. This feature is especially important for measurements at low temperatures. In power-measuring devices, thin resistive strips serve as sensitive elements acting as mixers at short wavelengths. To employ microwave methods it is necessary to establish a relation between the electrodynamic parameters (impedance, reflection coefficient) of the semiconductor samples placed in a waveguide or cavity and semiconductor characteristics (carrier density, mobility). Such relations have been obtained for a cylindrical semiconductor rod placed at the center of a waveguide[1] and for a sample in the form of a plane parallelepiped which is small compared with the wavelength in the waveguide and is placed in a plane parallel to the narrow wall of the waveguide.[2] References 3 and 4 were devoted to the construction of a model of a zero-thickness impedance shunt, but a numerical solution was obtained only for an asymptotic expression. In Ref. 5 the problem of scattering of electromagnetic waves by a structure consisting of thin resistive strips connected in parallel and placed in a rectangular waveguide was studied. The power absorption coefficients for the incident wave as a function of wavelength and the geometric dimensions of the structure were calculated in a wide range of variation of the resistance of the strips. The maximum dissipation by a single strip was obtained with the resistance $R_{\square}=0.1$ kΩ.

A flat sample is preferable for investigating processes associated with nonequilibrium photoconductivity, since it is difficult to illuminate the surface of a cylindrical rod uniformly. Furthermore, the greatest perturbation of the fields in a waveguide, which determines the sensitivity of the method, is produced by a sample placed in the transverse cross section of the waveguide. For this reason, in the present letter a thin semiconductor plate placed at the center of the transverse cross section of a waveguide is studied.

Investigations of the use of a semiconductor material as the active element in waveguide technology are now especially important.[6] In contrast to the use of plates in bolometric power meters, in the case at hand the semiconductor plates must withstand high dissipated power levels. Therefore it is important to find the geometric and physical parameters of a semiconductor plate which are required in order to realize a specific device and to study the admissible power dissipation levels in the active element.

Another important feature of this work must be clarified. The development of ActiveX controls for microwave power absorption, reflection, and transmission for a semiconductor plate placed in a rectangular waveguide can serve as a kind of physical library, similar to the libraries of numerical mathematical methods, provided that, of course, the latter are converted into visual libraries which are independent of the programming language. Once a sufficient of number of physical ActiveX controls for the mathematical modeling of different phenomena and devices are developed it will be possible to assemble a prototype of a real apparatus, similar to the operation of some programs for illustrating the operation of a network and for emulating technological processes (LabView). The most striking example of the application of modeling of physical processes (optical phenomena) are the dynamic-link libraries developed by Silicon Graphics (Open GL), and the ActiveX library based on them.

2. EQUIVALENT CIRCUIT OF A SEMICONDUCTOR PLATE

Let a semiconductor plate of thickness δ, width d, and height b be placed at the center of a waveguide, as shown in Fig. 1. The incident wave

$$E_x=\sin(\pi y/a)e^{-jk'z}, \tag{1}$$

where $k'=\sqrt{k^2-(\pi^2/a^2)}=2\pi/\lambda_g$, where $k=2\pi/\lambda$, excites in the strip currents I_x which emit in both directions electromagnetic waves that can be represented as a sum of the fundamental waves and higher-order harmonics. Let $I(y')dy'$ be the current in the section $(a-d)/2<y'<(a+d)/2$ (Ref. 7). Then the field of the wave reflected from the plate can be expressed in the form $(z=0)$

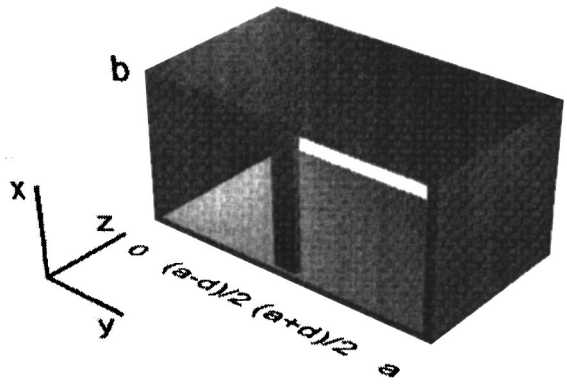

FIG. 1. Semiconductor plate at the center of a waveguide.

$$E_{-}=-i\frac{2\pi z_0}{a\lambda}\int_{\frac{a-d}{2}}^{\frac{a+d}{2}} I(y')\sum_{m=1}^{\infty}\frac{1}{\Gamma_m}\sin\frac{m\pi y}{a}\sin\frac{m\pi y'}{a}dy', \tag{2}$$

where a is the dimension of the wide wall of the waveguide, λ is the wavelength in free space, z_0 is the characteristic impedance of free space, and $\Gamma_m=\sqrt{(m\pi/a)^2-(2\pi/\lambda)^2}$ is the propagation constant of a H_{m0} mode in the waveguide. The current flowing through an element of the plate with coordinate y' and cross-sectional area $\delta dy'$ is expressed by the well-known formula[7]

$$I(y')=\sigma E_s(y')A, \tag{3}$$

where σ is the conductivity of the semiconductor, $E_s(y')$ is the field at the surface of the plate, the coefficient $A=2(1-\cos k\delta)/k\sin k\delta$ determines the distribution of the field inside the plate, and k is the propagation constant of the electromagnetic wave in the semiconductor. The field distribution can be obtained by solving Maxwell's equations taking into account the expression[1] for the current density in the semiconductor plate

$$\nabla^2 J+k^2 J=0, \tag{4}$$

where

$$k^2=\frac{\omega^4\varepsilon\mu\tau^2+\omega^2\varepsilon\mu-\omega^2\mu\sigma_{ac}\tau-i\omega\sigma_{ac}}{1+\omega^2\tau^2}. \tag{5}$$

The boundary conditions at the surface of the plate $(a-d)/2<y'<(a+d)/2$ are written in the form of an integral equation

$$E_s(y)=E_{+}(y)+\alpha\sum_{m=1}^{\infty}\frac{\beta_m}{\Gamma_m}\sin\frac{m\pi y}{a}, \tag{6}$$

where $E_{+}(y)=E_0\sin(\pi y/a)$ is the incident H_{10} wave, $\alpha=-i(2\pi\sigma z_0/a\lambda)A$, and

$$\beta=\int_{\frac{a-d}{2}}^{\frac{a+d}{2}} E_s(y')\sin\frac{m\pi y'}{a}dy'.$$

Since the plate is narrow, we assume that the field along the Y axis at the surface does not differ much from the average value $\overline{E_s}$. An expression for $\overline{E_s}$ can be obtained by averaging the left- and right-hand sides of Eq. (6) over the surface of the plate:

$$\overline{E_s}\approx\frac{E_0}{1-\alpha\left(\frac{d}{\Gamma_1}+\overline{\Sigma}\right)}, \tag{7}$$

where $\overline{\Sigma}$ is the average value of the sum

$$\sum_{m=1}^{\infty}\frac{a}{m\pi}\sin\frac{m\pi y}{a}\int_{\frac{a-d}{2}}^{\frac{a+d}{2}}\sin\frac{m\pi y'}{a}dy'. \tag{8}$$

We note that only terms with odd m are nonzero and $\Gamma_m\approx m\pi/a$ for $m\geqslant 3$. To contract the series we employ the expression[6]

$$\sum_{2}^{\infty}\frac{1-\cos 2mx}{m^3}\approx -2x^2\ln 2x+3x^2-(1-\cos 2x).$$

Substituting the expression for the field at the surface into Eq. (2), we easily determine the reflection coefficient of the semiconductor plate for the fundamental mode

$$r=-\frac{1}{1-\frac{\Gamma_m}{d}\left(\frac{1}{\alpha}-\overline{\Sigma}\right)}. \tag{9}$$

Comparing expression (9) with the reflection coefficient for an inductive resistance connected in series with a resistance, connected in parallel to an equivalent line with characteristic impedance $z_g=[(2b/a)(\Lambda/\lambda)]z_0$, the inductive resistance and the resistance of a semiconductor plate can be expressed as

$$X=\frac{z_g\pi}{d\Lambda}\left(-\frac{\mathrm{Re}\,\alpha}{|\alpha|^2}+\overline{\Sigma}\right), \tag{10}$$

$$R=-\frac{z_g\pi}{d\Lambda}\left(\frac{\mathrm{Im}\,\alpha}{|\alpha|^2}\right).$$

Using the expressions for A and α, it can be shown that at frequencies at which the penetration depth of the electromagnetic wave $\delta_{m\omega}\gg\delta$ the resistance R equals the dc resistance of the plate

$$R=\frac{b}{\delta\sigma d}.$$

For a low nonequilibrium carrier density, when the penetration depth of the microwave radiation is much greater than the skin depth, the form of the distribution of A can be simplified, making the assumption that A is constant over the depth of the plate.

The meaning of $\overline{\Sigma}$ can be easily determined by passing to the limit $\sigma\to\infty$, i.e., by making the plate metallic. In this case $\alpha\to\infty$ and the reflection coefficient assumes the form of the reflection coefficient for a purely inductive strip connected in parallel in the equivalent circuit. Having calculated the average value of the sum (8), we obtain the expression

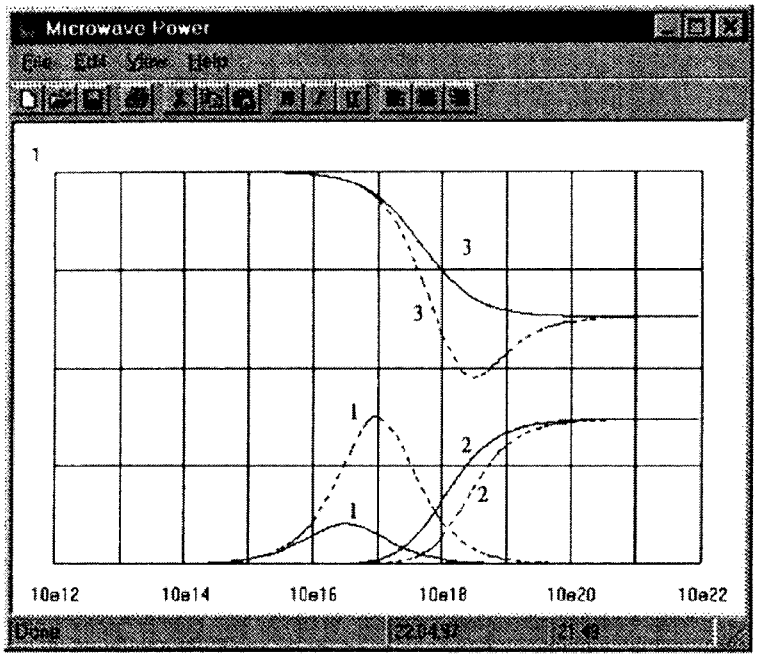

FIG. 2. Microwave absorption (1), reflection (2), and transmission (3) coefficients for two values of the parameters $\omega\tau=2.9$ (solid lines) and $\omega\tau=0.005$ (dashed lines).

$$\frac{X}{z_g}=\frac{a}{2\Lambda}\left(-3\ln 2+\ln\frac{8a}{\pi d}\right),$$

which agrees well with the well-known result obtained in Ref. 7.

Knowing the parameters of the equivalent circuit, we can now determine the power absorbed by the semiconductor plate. The power absorption coefficient is described, taking account of expression (10), by the equation

$$A^2=\frac{P_{pacc}}{P_+}=\frac{\dfrac{R}{z_g}}{\left(\dfrac{1}{2}+\dfrac{R}{z_g}\right)^2+\left(\dfrac{X}{z_g}\right)^2}\ . \tag{11}$$

Similarly, we obtain for the reflection coefficient

$$|R|^2=\Gamma\Gamma^*=\frac{1}{\left(1+2\dfrac{R}{z_g}\right)^2+\left(2\dfrac{X}{z_g}\right)^2}\ . \tag{12}$$

The change in the losses is determined by the change in the conductivity σ. The microwave conductivity of the semiconductor equals

$$\sigma=\frac{\sigma_{ac}}{1+i\omega\tau}, \tag{13}$$

where τ is the carrier scattering time and $\sigma_{ac}=\mu ne$ is the low-frequency conductivity.

The well-known critical value of the density for which the maximum microwave absorption is observed makes it possible to determine some characteristics of a semiconductor, for example, the trapping coefficient with continuous photoconduction. For carrier density n much greater than the equilibrium density, n decreases according to a hyperbolic law[8]

$$n=\frac{n_0}{1+\gamma n_0 t}, \tag{14}$$

where γ is the trapping coefficient and n_0 is the initial nonequilibrium density. The trapping coefficient can be determined from the following expression by measuring the times t_1 and t_2 corresponding to maximum microwave absorption as a function of the moment of illumination of the plate by a short light pulse with two values of the intensity J and ηJ:

$$\gamma=\frac{1}{n_{\max}}\ \frac{1-\eta}{t_1-\eta t_2}. \tag{15}$$

Thus, the relations obtained establish the relationship between the characteristics of the semiconductor and the microwave power losses in a flat semiconductor plate placed at the center of the waveguide. For specified dimensions of the plate, the absorbed power can be calculated as a function of the carrier density and mobility in the semiconductor. The inverse problem can also be solved.

3. DESCRIPTION OF ActiveX

A library consisting of a standard extension of OLE (object linking and embedding) controls was developed on the basis of the method presented above. After a given control element is linked, a number of properties, the most important ones being the parameters of the waveguide system and the semiconductor plate, are available to the designer. The following characteristics can be specified by easily varying the corresponding control properties of SemiconductivePlate'': the carrier mobility and initial carrier density, the magnetic permeability and dielectric permittivity of the semiconductor material, carrier lifetime, geometric dimensions of the plate, dimensions of the wide and narrow walls of the waveguide, and the frequency of the microwave signal. After the Count

Data method is applied, the corresponding properties of the control element ''SemiconductivePlate. Absorption, SemiconductivePlate. Reflection and SemiconductivePlate. Transition'' will contain self-evident values of the coefficients. An example of the operation of this method is given in Fig. 2 for a 45×90 mm waveguide at 3 GHz, $d=5$ mm, $\delta=10^{-5}$ m with the parameters taken from Ref. 9 for a silicon plate with initial density 10^{12} cm^{-3}. As an illustration, the curves of the microwave absorption, reflection, and transmission coefficients are constructed for two values of the parameters $\omega\tau$. The solid lines correspond to $\omega\tau=2.9$ (4.2 K) and the dashed lines correspond to $\omega\tau=0.005$ (room temperature). The file mwpower.ocx of this ActiveX control can be obtained at the address popov@ssdkorovin.ioffe.rssi.ru.

[1] D. Robert and R. D. Larrabie, J. Appl. Phys. **36**, 1597 (1965).
[2] B. V. Zubov, A. A. Manenkov, V. A. Milyaev, G. N. Mikhaĭlova, T. M. Murina, and A. Seferov, Fiz. Tverd. Tela (Leningrad) **18**, 706 (1976) [Sov. Phys. Solid State **18**, 406 (1976)].
[3] Kh. A. Gerb, P. M. Fridberg, and I. M. Yakover, Radiotekh. Élektron. **25**, 2079 (1980).
[4] Kh. A. Gerb, P. V. Nikolaev, P. M. Fridberg, and I. M. Yakover, Radiotekh. Élektron. **29**, 1917 (1984).
[5] S. V. Biryukov and I. M. Starobin, Élektronnaya Tekhnika Ser. Élektronika SVCh **1**(415), 28 (1989).
[6] S. G. Tantawi, T. G. Lee, R. D. Ruth, A. E. Vlieks, and M. Zolotorev in *Proceedings of the 1995 Particle Accelerator Conference*, Dallas, 1995, Vol. 3, IEEE, pp. 1584–1586.
[7] L. Lewin, *Advanced Theory of Waveguides*, Illiffe, London, 1951 [Russian translation], Izd. Inostr. Lit., Moscow, 1954].
[8] S. M. Ryvkin, *Photoelectric Effects in Semiconductors*, Consultants Bureau, New York, 1964 [Russian original, Izd. Fiz.-Matem. Lit., Moscow, 1963].
[9] A. Dargys and J. Kundrotas, *Handbook of the Physical Properties of Ge, Si, GaAs, and InP*, Vilnius, 1994.

Translated by M. E. Alferieff

Characteristic features of the copper–oxygen interaction, electron pairs, and the asymmetric π bond in high-T_c superconductors

M. V. Krasin'kova

A. F. Ioffe Physicotechnical Institute, Russian Academy of Sciences, St. Petersburg
(Submitted May 15, 1997)
Pis'ma Zh. Tekh. Fiz. **23**, 57–63 (September 12, 1997)

The experimental data on the structural features and bond character in layers of high-T_c superconductors and related materials are analyzed. Correlations are found between T_c and the orthorhombic distortion parameter and between T_c and the incommensurability of the layers in the structure. It is pointed out that the electric field around the CuO_2 plane is asymmetric. On the basis of this analysis it is proposed that the unusual properties of high-T_c superconductors are due to the mixed covalent–ionic bond character in the CuO_2 layers, a consequence of which is the presence of electron pairs in the layer. It is shown that in the presence of asymmetry of the electric field around the CuO_2 planes these pre-existing electron pairs can give rise to superconductivity via the asymmetric delocalized π bond. © *1997 American Institute of Physics.* [S1063-7850(97)01009-4]

Analysis of the experimental data on the structure of high-T_c superconductors and related materials has shown that for all their diversity, there are a number of specific features that are characteristic for all compounds.

Plane–square, or nearly so, coordination of the copper, linear coordination of the oxygen, and a strong Cu–O bond are observed in the CuO_2 layers in all materials. These layers have a negative charge, which is produced by electron transfer from neighboring layers.

If the charge of a CuO_2 layer equals $2-$ and the Cu in the layer has an undistorted (according to x-ray data) plane–square coordination, then materials with such layers are insulators.

Conduction appears in these materials only after orthorhombic distortions, which destroy the plane–square coordination of the Cu, appear in them. It is not important how these distortions are produced — doping of neighboring layers by substitution or introduction of excess oxygen or even the addition of layers (TlO, BiO) which are incommensurate with other layers in the structure. In addition, even though the orthorhombic distortions are characterized by an average (over all layers) parameter $(b-a)/(b+a)$, which does not reflect the real picture of the distortions directly in a CuO_2 layer, a clear correlation is observed between T_c and this parameter — the larger the distortion, the higher T_c. A correlation is also observed between T_c and the incommensurability of the layers — the larger the difference between the sum of the ionic radii for ions in layers with the NaCl structure and the product of $2^{1/2}$ times the Cu–O distance in a CuO_2 layer, the higher T_c.

When orthorhombic distortions appear, the charge of a CuO_2 layer changes (decreases).

Finally, an important characteristic feature of all conducting materials in this family is the asymmetry of the electric field around a CuO_2 plane. In some cases it is determined by the structure ($YBa_2Cu_3O_7$, Tl- and Bi-containing compounds); in other cases the structure arises as a result of doping ($La_{2-x}Sr_xCuO_4$). The asymmetric field is produced by ions which possess the electron shell of an inert gas.

These experimental data all show that the explanation of the unusual physical properties of these materials must be sought in the characteristic features of the bond in the CuO_2 layer and the possible change in the bond character as a result of orthorhombic distortions. A characteristic feature of the bond in the CuO_2 layers is its mixed ionic–covalent character.

Linus Pauling was the first to call attention to the mixed character of the bond in the CuO_2 layers.[1] He proceeded from the small difference between the electronegativity of copper and oxygen. He suggested that in each CuO_4 coordination square in a CuO_2 plane two bonds must be covalent, resonating among the four positions (''one pure covalent bond'' $\leftrightarrow$ ''no bond''). P. W. Anderson showed[2] that the insulating state accompanying a resonance of the bond is not an obstacle for the appearance of superconductivity and can be transformed into a superconducting state by doping. He also introduced the concept of pre-existing pairs, which under certain conditions could give a superconducting state.[3]

Our analysis showed that the existence of electron pairs is indeed possible in the presence of a mixed ionic–covalent character of the Cu–O bond in a CuO_2 layer. Among the pairs are: electron pairs which give a σ bond between ions and participate in covalent–ionic resonance (insulating state); electron pairs which form a π bond between ions and also participate, together with pairs of σ bonds, in a resonance state propagating along a chain of ionically–covalently bound ions (metallic state); and, finally, after a transition from the ionic–covalent resonance state to a covalent σ-bond state in these chains, delocalized pairs of π electrons of an asymmetric π bond produced by the asymmetry of the electric field around the CuO_2 plane — these pairs are responsible for the superconducting state.

Before discussing high-T_c superconductors and related materials, I wish to say a few words about the mixed character of the bond. The bond is ordinarily regarded as a superposition of several equivalent states of the bond or, alter-

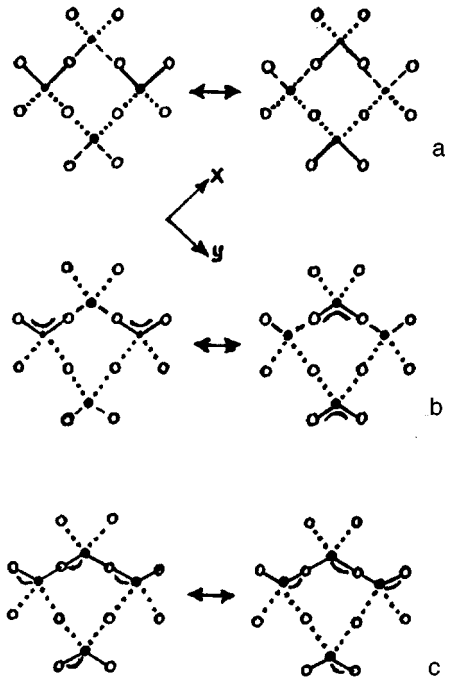

FIG. 1. Canonical forms producing a resonance state: a — Insulating state, b — metallic state, c — superconducting state. Filled circles — copper ions; open circles — oxygen ions; double arrow — resonance state; solid lines — σ bond; dashed lines — ionic bond participating in the resonance; dots — purely ionic bond; bent curves — π bond.

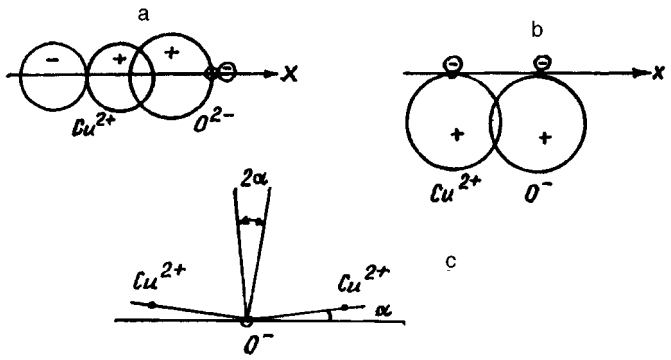

FIG. 2. Formation of a covalent bond: a — σ bond with polarization of an oxygen ion by a copper ion; b — π bond with polarization of copper and oxygen ions in an asymmetric electric field; c — rotation of the p_z orbital of O^- with formation of a σ bond with copper ions located to the left and right under conditions of a corrugated CuO_2 plane.

natively, as a resonance of several canonical forms.[4] The resonance state lowers the energy of and stabilizes the system. But the resonance state itself is very sensitive to lattice distortions which change the distance between the atoms or angles between the bonds. In the presence of lattice deformations the equivalence of the canonical forms vanishes. Some forms go out of resonance and the bonds become separated according to character and ordering.

A change in bond character is accompanied by a change in the physical properties of the material. In addition, the effect of bond character is so strong that the appearance of a very small amount of a phase with an altered bond character is sufficient to observe a change in the properties of the material. This is the reason for the main difficulties in interpreting the results of investigations of the physical properties of such materials, since the changes in the properties are detected but it is difficult to determine what has caused these changes.

For these reasons, it is difficult to indicate unequivocally on the basis of the currently existing experimental data all possible canonical forms participating in the resonance state in high-T_c superconductors, but the general picture of the change in bond character can be represented as follows (Figs. 1a–1c).

The insulating state (Fig. 1a) (stoichiometric La_2CuO_4, $YBa_2Cu_3O_6$) is characterized by ionic–covalent resonance between two canonical forms, each of which includes four copper coordination squares. Each square contains two O^{2-}–Cu^{2+}–O^{2-} ionic–covalent bonds, which participate in the resonance state, and two purely ionic bonds. The choice of these canonical forms was made from symmetry considerations with allowance for the experimentally observed antiferromagnetic (AF) ordering of the magnetic moments on the Cu^{2+} ions, the moments being oriented along the diagonals of the Cu_4O_4 squares and tilting slightly toward the CuO_2 plane.[5] The fact that AF ordering of this form is present in itself attests to the existence of a distinguished direction in a plane, possibly due to, for example, the anisotropy of the thermal vibrations of the ions. It can be conjectured that the separation of the bonds participating in the resonance state into purely ionic and ionic–covalent is due to the anisotropy of the thermal vibrations. It is evident from Fig. 1 that all the Cu^{2+} ions and half the O^{2-} ions are included in the resonance state, and these ions, which participate in the resonance, form zigzag-shaped chains extending along the CuO_2 plane. The O^{2-} ions, which do not participate in the resonance state, form a purely ionic bond between the chains. A covalent bond (σ bond) is formed by unoccupied p_x and p_y orbitals of Cu^{2+} and completely filled $p_x(p_y)$ orbitals of O^{2-} (Fig. 2a). Since O^{2-} cannot form two σ bonds at an angle of 180°, it forms only one bond, using alternately at resonance the positive and negative lobes of the same orbital. Therefore a covalent bond is formed by electron pairs, and they are ''localized'' within the hybrid orbitals of the bond. The unpaired electron of Cu^{2+} does not participate in the bond and is evidently in a p_z orbital.

The metallic state (Fig. 1b), which is observed when the orthorhombic distortions of the lattice are enhanced by doping, is characterized by increased corrugation of the CuO_2 layer (the figure shows the projection of the corrugated layer on the CuO_2 plane), elongation of the purely ionic bonds between the chains, and shortening of the bonds in the chains themselves as well as by a change in the charge state of oxygen in the chains from O^{2-} to O^-. The latter enables the formation of a resonating π bond between the O^-–Cu^{2+}–O^- ions. The π bond is formed by overlapping of the p_z orbitals of O^- and Cu^{2+}, each of which contains one electron. The formation of a π bond with a quite large distance between the ions is made possible by the deformation of the p_z orbitals of O^- and Cu^{2+} in the asymmetric electric field around the CuO_2 plane (increase in the volume of the lobe

turned toward the large positive charge) (Fig. 2b). In this state of the system, the resonance of the σ bond and the corrugation of the CuO_2 layer prevent delocalization of the π bond along the entire chain of bonds. As a result of the corrugation, the p_z orbital of O^-, on forming a σ bond with neighboring Cu^{2+} ions, should undergo oscillations in the direction of the diagonal of the Cu_4O_4 square by an angle equal to twice the slope angle of the σ bond with respect to the CuO_2 plane (Fig. 2c).

Superconductivity first appears as a result of delocalization of the π bond along the entire chain, when the oxygen and copper occupy an sp hybridization state. In the process, the ionic–covalent resonance state ceases. Stationary σ bonds between the ions also form along the entire chain (Fig. 1c). Evidently, the corrugation of the layer also vanishes, since Cu^{2+} in the sp hybridization state can form bonds at an angle different from 90°. Under the conditions of an asymmetric π bond, the π electrons remain paired. This is in contrast to a symmetric π bond, where the electrons are distributed between two lobes of the π orbitals.

In summary, the model proposed in this letter makes it possible to answer the main question of high-T_c superconductivity concerning the nature of the pairing. The pairing mechanism is an exchange interaction between Cu^{2+} and O^- ions in an asymmetric electric field, resulting in the formation of an asymmetric π bond. The continuous transition to superconductivity without appreciable structural changes is determined by the delocalization of pre-existing electron pairs. Thus the mixed character of the bond gives rise to the presence of electron pairs and the asymmetric field around the plane with the mixed bond character, polarizing the ions, gives rise to superconductivity via the asymmetric π bond. Superconductivity of this kind, by its very nature, is of a filamentary character.

Evidently, the above mechanism of conversion of a delocalized π bond into a superconducting π bond in an asymmetric electric field can also explain the superconductivity of fullerenes, intercalated graphites, and other high-T_c superconductors.

I wish to thank my colleagues A. P. Paugurt and N. V. Agrinskaya for a discussion and critical remarks.

[1] L. Pauling, Phys. Rev. Lett. **59**, 225 (1987).
[2] P. W. Anderson, Science **235**, 1196 (1987).
[3] A. Khurana, Physics Today **40**, No. 4, 17 (1987).
[4] L. Pauling, *The Nature of the Chemical Bond and the Structure of Molecules and Crystals*, Cornell University Press, Ithaca, New York, 1940 [Russian translation, Gostekhizdat, 1947].
[5] R. J. Birgeneau, M. A. Kastner, A. Aharony *et al.*, Physica C **153–155**, 515 (1988).

Translated by M. E. Alferieff

Solution of the problem of optical tomography for bounded scattering media in the two-flux radiation-transfer model

S. A. Tereshchenko and S. V. Selishchev

Moscow Electronics Institute (Technical University)
(Submitted September 6, 1996)
Pis'ma Zh. Tekh. Fiz. **23**, 64–67 (September 12, 1997)

The problem of optical tomography of scattering media is solved on the basis of an exact solution of the equations of the two-flux radiation-transfer model for a bounded medium. It is shown that after preliminary processing of the measurements the problem reduces to an inverse Radon transform, provided that the absorption and scattering coefficients are assumed to be proportional to the density of absorbing and scattering centers. © *1997 American Institute of Physics.* [S1063-7850(97)01109-9]

In solving the problem of transmission optical tomography of strongly scattering (turbid) media, an analysis of the transmission of a thin laser beam through such a medium is crucial. The mathematical model describing this process should, on the one hand, describe sufficiently accurately the physics of the passage of radiation through matter and, on the other, make it possible to employ well-developed methods for inverting the Radon transform[1] in order to reconstruct the two-dimensional (three-dimensional) distribution of the optical characteristics of the scattering medium. A promising approach is an extension of the Kubelka–Munk two–flux model[2], developed for the stationary case and used for describing the passage of radiation through uniform media, to the nonstationary case[3] and nonuniform media in order to solve the problem of optical tomography.[4]

In Ref. 4 the problem of optical tomography was solved on the basis of an analysis of radiation transfer in the approximation of a semi-infinite medium. Naturally, this introduced an inaccuracy into the reconstructed image. In the present letter the problem of optical tomography is solved on the basis of an exact solution for a bounded medium. This makes the application of the inverse Radon transform at the next stage more reasonable. Once again, the answer is obtained under the assumption that the main optical characteristics of the scattering medium (absorption and scattering coefficients) are proportional (with different proportionality constants) to the density of absorbing and scattering centers in the medium.

Let us introduce in the investigated plane of section of the three-dimensional object a stationary coordinate system (x,y) and a rotating coordinate system $(\xi,\zeta)=(x\cos\theta+y\sin\theta, -x\sin\theta+y\cos\theta)$, where θ is the angle of rotation of the rotating coordinate system relative to the stationary coordinate system. Then the propagation of an optical pulse along the ζ axis can be described in the two-flux approximation by the system of equations

$$\left.\begin{aligned}&\frac{1}{v}\frac{\partial}{\partial t}F_+(\zeta,t)+\frac{\partial}{\partial\zeta}F_+(\zeta,t)+m(\zeta)F_+(\zeta,t)\\&\quad -m_s(\zeta)F_-(\zeta,t)=0\\&\frac{1}{v}\frac{\partial}{\partial t}F_-(\zeta,t)-\frac{\partial}{\partial\zeta}F_-(\zeta,t)+m(\zeta)F_-(\zeta,t)\\&\quad -m_s(\zeta)F_+(\zeta,t)=0\end{aligned}\right\}, \tag{1}$$

$$\left.\begin{aligned}F_+(\zeta_0,t)=F_0(t)\\F_-(\zeta,t)=0\end{aligned}\right\}\quad\left.\begin{aligned}F_+(\zeta,0)=0\\F_-(\zeta,0)=0\end{aligned}\right\}, \tag{2}$$

where t is the time, v is the speed of light in the medium, $F_+(\zeta,t)>0$ is the energy flux density in the direction of the ζ axis, $F_-(\zeta,t)>0$ is the energy flux density in the opposite direction, $m_a(\zeta)=m_a(\xi,\zeta)$ is the radiation absorption coefficient of the medium, $m_s(\zeta)=m_s(\xi,\zeta)$ is the radiation scattering coefficient of the medium, $m(\zeta)=m(\xi,\zeta)=m_a(\zeta)+m_s(\zeta)$, ζ_0 is the point of entry of the laser beam into the scattering medium, ζ_1 is the point of exit of the laser beam from the scattering medium, and $F_0(t)$ is the initial shape of the laser pulse. Expression (2) gives the boundary and initial conditions.

Just as in Ref. 4, let $m_a(x,y)=An(x,y)$ and $m_s(x,y)=Sn(x,y)$, where $n(x,y)$ is the density of absorbing and scattering centers in the medium and A and S are coordinate-independent constants. This quite natural assumption reduces the two unknown functions $m_a(x,y)$ and $m_s(x,y)$ to the single function $n(x,y)$. Switching to the total energy of the corresponding pulses

$$U_+(\zeta)=\int_0^\infty F_+(\zeta,t)dt \quad\text{and}\quad U_0=\int_0^\infty F_0(t)dt,$$

we obtain for $U_+(\zeta)$ an ordinary differential equation

$$\frac{d^2}{d\zeta^2}U+(\zeta)-\frac{n_s'(\zeta)}{n_s(\zeta)}\frac{d}{d\zeta}U_+(\zeta)-A(A+2S)n^2(\zeta)U_+(\zeta)=0, \tag{3}$$

$$\left.\begin{aligned}&U_+(\zeta_0)=U_0\\&\frac{d}{d\zeta}U_+(\zeta)|_{\zeta=\zeta_1}=-(A+S)n(\zeta_1)U_+(\zeta_1)\end{aligned}\right\}. \tag{4}$$

The solution of Eq. (3) with the boundary conditions (4) is

$$U_+(\zeta)=U_0\left[C_1\exp\left(-\int_{\zeta_0}^{\zeta}\sqrt{A(A+2S)}n(\chi)d\chi\right)+C_2\exp\left(\int_{\zeta_0}^{\zeta}\sqrt{A(A+2S)}n(\chi)d\chi\right)\right], \tag{5}$$

where

$$C_1=\frac{[A+S+\sqrt{A(A+2S)}]}{[A+S+\sqrt{A(A+2S)}]-[A+S-\sqrt{A(A+2S)}]\varphi^2(\zeta_1)},$$

$$C_2=\frac{-[A+S-\sqrt{A(A+2S)}]\varphi^2(\zeta_1)}{[A+S+\sqrt{A(A+2S)}]-[A+S-\sqrt{A(A+2S)}]\varphi^2(\zeta_1)}. \tag{6}$$

Writing $q=U_+(\zeta_1)/U_0$, we find the projection data

$$p(\xi,\theta)=\int_{\zeta_0}^{\zeta_1}\sqrt{A(A+2S)}n(\chi)d\chi:$$

$$p(\xi,\theta)=-\ln\left(\frac{-\sqrt{A(A+2S)}+\sqrt{A^2+2AS+q^2S^2}}{q[A+S-\sqrt{A(A+2S)}]}\right). \tag{7}$$

Applying to the projection data the inverse Radon transform $\mathcal{R}^{-1}\{p(\xi,\theta)\}$ (Ref. 1) we can reconstruct the density distribution of the absorbing and scattering centers as

$$n(x,y)=\frac{1}{\sqrt{A(A+2S)}}\mathcal{R}^{-1}\{p(\xi,\theta)\}. \tag{8}$$

In summary, for the case studied above the problem of tomographic reconstruction of the density distribution $n(x,y)$ of absorbing and scattering centers in a medium reduces to solving an inverse Radon transform provided that the measurements are processed beforehand according to Eq. (7) in order to find the exact projection data.

This work was supported by the Russian Fund for Fundamental Research (Project 96-02-18900).

[1] F. Natterer, *The Mathematics of Computerized Tomography*, Wiley, New York, 1986 [Russian translation, Mir, Moscow, 1990].
[2] A. Ishimaru, *Wave Propagation and Scattering in Random Media*, Academic Press, New York, 1978, Vol. 1 [Russian translation, Mir, Moscow, 1981].
[3] S. A. Tereshchenko, V. M. Podgaetskiĭ, N. S. Vorob'ev, and A. V. Smirnov, Kvantovaya Élektron. (Moscow) **23**, 265 (1996).
[4] S. V. Selishchev and S. A. Tereshchenko, Pis'ma Zh. Tekh. Fiz. **21**(12), 24 (1995) [Tech. Phys. Lett. **21**, 451 (1995)].

Translated by M. E. Alferieff

Stochastic perturbation and relaxation of a classical Coulomb plasma

A. N. Tkachev and S. I. Yakovlenko

Institute of General Physics, Russian Academy of Sciences, Moscow
(Submitted May 5, 1997)
Pis'ma Zh. Tekh. Fiz. **23**, 68–76 (September 12, 1997)

It is shown that the dynamic mixing of phase trajectories in a system of classical Coulomb particles does not result in the recombination described by the kinetic equations. The effect of the imprecision of the computational method and the effect of permutation of the particle velocities on recombination relaxation is studied. The imprecision of the numerical integration of the dynamical equations results in a loss of reversibility of the solution and in anomalously slow (in exact calculations) relaxation. If the permutations of the particle velocities are made with a rate higher than the rate of Coulomb collisions, recombination relaxation proceeds in accordance with kinetic theory. © *1997 American Institute of Physics.* [S1063-7850(97)01209-3]

INTRODUCTION

In the works summarized in Refs. 1 and 2 it was concluded on the basis of an analysis of the results of computer simulations and various kinetic models that in the numerical modeling of the dynamics of many classical Coulomb particles, dissipative processes (and, in particular, recombination) occur only to the extent to which an external (with respect to the dynamical equations) stochastic perturbation acts on the system of particles. In the present letter we examine in detail the effects of two types of stochastic perturbation: imprecision of the computational method, and permutation of the particle velocities.

ON NUMERICAL MODELING

We investigated the temporal evolution of a system of n electrons and n ions confined in a cube with absolutely rigid walls, which limit the motion of the particles (see Refs. 1 and 2 for a more detailed discussion). The edge length a of the cube was chosen so as to obtain the desired charged-particle density: $N_e=N_i=n/a^3$. The particles were assumed to be permeable spheres with radius $r_0=0.05N_e^{1/3}$ and, accordingly, the ionization energy from the bottom of the well was equal to $\varepsilon_1=(2.4/20)e^2N_e^{1/2}$, where e is the electron charge. The ion mass was assumed to equal the proton mass.

Using the interparticle distance $N_e^{1/3}$ as the unit of length and the Langmuir period ($T_L=2\pi/\omega_L$, where $\omega_L^{-1}=\sqrt{(m_e/4\pi e^2N_e)}$ and m_e is the electron mass) as the unit of time, for a sufficiently low initial kinetic energy of the particles, after a time of the order of one tenth of the Langmuir period the plasma arrives in a metastable state in accordance with a universal time dependence of the kinetic energy of the particles.[3] For this reason, here the evolution of the system was followed up until the establishment of a metastable state, after which the particle coordinates and velocities obtained from a preliminary calculation were used as the initial conditions. Permutational stochastization was implemented in a number of calculations,[4] i.e., the velocity vectors of some electrons were randomly permuted with those of other electrons. The method of distinguishing nearest neighbors (see Refs. 1 and 2 for a more detailed discussion) with the modifications described in Ref. 5 was used in solving the problem numerically.

In studying the evolution of the system, the following were calculated: ε_ε — the relative change in the total energy of the system (this quantity characterizes to some extent the computational error); $K_i(t)$ and $K_e(t)$ — the kinetic energies of the electrons and ions; $U(t)$ — the potential energy of the system; $n_-(t)$ — the number of bound electrons (with energy $\varepsilon<1.5e^2(2N_e)^{1/3}T_e$). In the present work the temperature of the electrons was calculated as two thirds of their kinetic energy. The degree of ideality of the plasma is characterized by the quantity $\gamma=(e^2(2N_e)^{1/3}/T_e)$.

ON THE DYNAMIC MIXING OF PHASE TRAJECTORIES

The distances between the points of initially close trajectories of a system of particles in phase space were computed for a series of calculations. The calculations showed that an exponential divergence of the trajectories of both ions and electrons is observed over a time interval close to half the Langmuir period. Then the growth in the divergence slows down on account of the boundedness of both the coordinates and the velocities of the particles.

Calculations with a different number of particles show that for sufficiently large $n>50$ the slopes of the curves constructed on a semilogarithmic scale are quite close in the region of exponential growth. The exponent of the exponential determining the divergence of the electronic trajectories is proportional to $L\approx 15\pm 1$. This is the maximum Lyapunov exponent,[6,7] measured in units of the reciprocal of the Langmuir period. It characterizes the dynamic mixing time of the translational degrees of freedom.

Calculations were also performed with an order of magnitude higher temperature. The Lyapunov exponent was practically the same as before. Therefore the value found for the Lyapunov exponent $L\approx 15\pm 1$ is a universal dynamical characteristic of a classical Coulomb plasma.

LOSS OF REVERSIBILITY OF THE NUMERICAL SOLUTION

The accuracy of the solution of the dynamical equations in our calculations is quite high: $\varepsilon_\varepsilon\sim 10^{-6}$. A time $\tau\sim(1/L)\ln(10^6)\sim 1$ is required in order for the change pro-

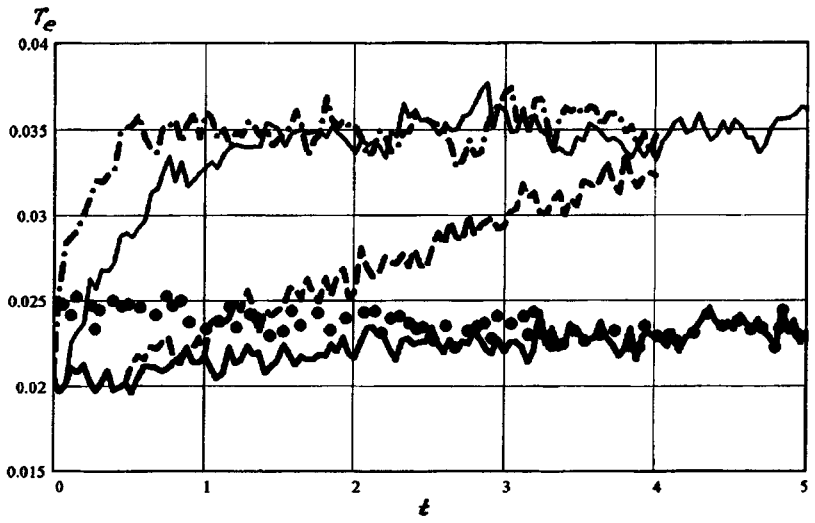

FIG. 1. Variation of the electron temperature. Initial parameters: $2n=1024$, $N_e=10^{14}$ cm^{-3} ($T_L=10^{-11}$ s); $K_e(0)=0.31n$ eV; $K_i(0)=0.041n$ eV, $U(0)=-0.0091n$ eV, $n_-(0)=107$. Time is measured in units of the Langmuir period and temperatures are measured in units of eV. The heavy curve corresponds to evolution in the absence of an external perturbation, motion in the positive time direction; the dotted curve corresponds to the reverse motion; the dashed curve corresponds to permutational stochastization over time intervals which are multiples of $\tau_p=0.5$; solid curve — $\tau_p=0.1$; dot-dash curve — $\tau_p=0.01$.

duced by this error in the state of the system to result in a divergence of the phase trajectory by an amount equal in order of magnitude to the change itself. This is the period of time over which a phase droplet of a size determined by the computational error spreads over the entire part of the energy surface made accessible in the phase space by the dynamical equations.

This is also confirmed by numerical calculations. For initially close trajectories the energy of the system is conserved, to a high degree of accuracy $\varepsilon\sim 10^{-4}\%$, over the entire computational time, and the other coarse parameters $K_i(t)$, $K_e(t)$, $U(t)$, and $n_-(t)$ start to differ only at $t\approx 1$ by an amount of the order of their characteristic change.

The imprecision of the numerical solution of the dynamical equations is accompanied by a loss of reversibility of the numerical calculations. This was demonstrated directly by reversing the system (reversing at some moment in time the velocities of all the particles). The calculations showed that the values of the coarse parameters $K_i(t)$, $K_e(t)$, $U(t)$, and $n_-(t)$ in the reversed motion start to differ from the values which they had before reversal in a time interval of the order of unity. An example of the irreversible behavior of the kinetic energy is given in Fig. 1 (dashed curve).

IRREVERSIBLE GROWTH OF A RECOMBINATION "TAIL"

The calculations show that over times $t\sim 1$ at which complete mixing of phase trajectories has occurred the dissipative recombination process has just barely even started. However, according to existing ideas, a recombination electron distribution function over the total energy should be established and the corresponding recombination flux should be formed even over the time $\tau_e\approx(3/4\sqrt{2\pi})\,(\sqrt{m_e}T_e^{3/2}/e^4N_e\Lambda)\approx 0.5T_L$ (here $\Lambda(\gamma)$ is the Coulomb logarithm). Furthermore, intense recombination heating of the electrons should occur.

However, the numerical calculations give a distribution that differs radically from both the recombination and Boltzmann distributions, and the recombination heating is anomalously small. The point is that the growth of a recombination "tail" in the electron energy distribution occurs only to the extent to which reversibility of the numerical solution is lost. This is shown by calculations of the distribution functions (see Fig. 2a) for different time intervals *before* and *after* reversal of the system. After reversal the number $n_-(t)$ of bound electrons does not return to the initial value but rather continues to increase.

Irreversible growth of the number of bound electrons corresponds to recombination relaxation which is anomalously slow in the exact calculations. For the calculations presented, the estimates give a recombination time that is tens of times shorter than the recombination time $\tau_{\rm rec}\approx 0.57(\lambda\cdot\gamma^{9/2})\approx 16$ that follows from the kinetic theory. The time for establishing a recombination distribution as observed in the calculations is longer than τ_e by approximately the same factor.

RECOMBINATION ACCOMPANYING PERMUTATIONAL STOCHASTIZATION

As was shown in Ref. 4, the permutation of the velocities of different electrons also results in the growth of a recombination tail in the distribution function. The results of the more detailed calculations presented here (Figs. 1 and 2) show that recombination relaxation proceeds at a rate corresponding to the kinetic theory only if the permutational stochastization is performed over time intervals τ_p of the free motion of the system which are much shorter than τ_e. For sufficiently long $\tau_p\approx 0.5T_L\approx\tau_e$ relaxation is several times slower than follows from the kinetic theory. In this case (just as in the case of relaxation due to loss of reversibility of the numerical solution) the recombination rate depends strongly on the intensity of the external stochastic perturbation (rate of permutations). In the case when the intervals of free motion decrease to $\tau_p=0.1T_L\approx(1/5)\tau_e$ the characteristic recombination time reaches the value $\tau_{\rm rec}$ determined by the kinetic theory, and further substantial acceleration of recombination does not occur even with a very large decrease in the free-motion interval — down to $\tau_p=0.01T_L\approx(1/50)\tau_e$.

In the case of a strong stochastic perturbation a Boltzmann distribution is established over a time of the order of

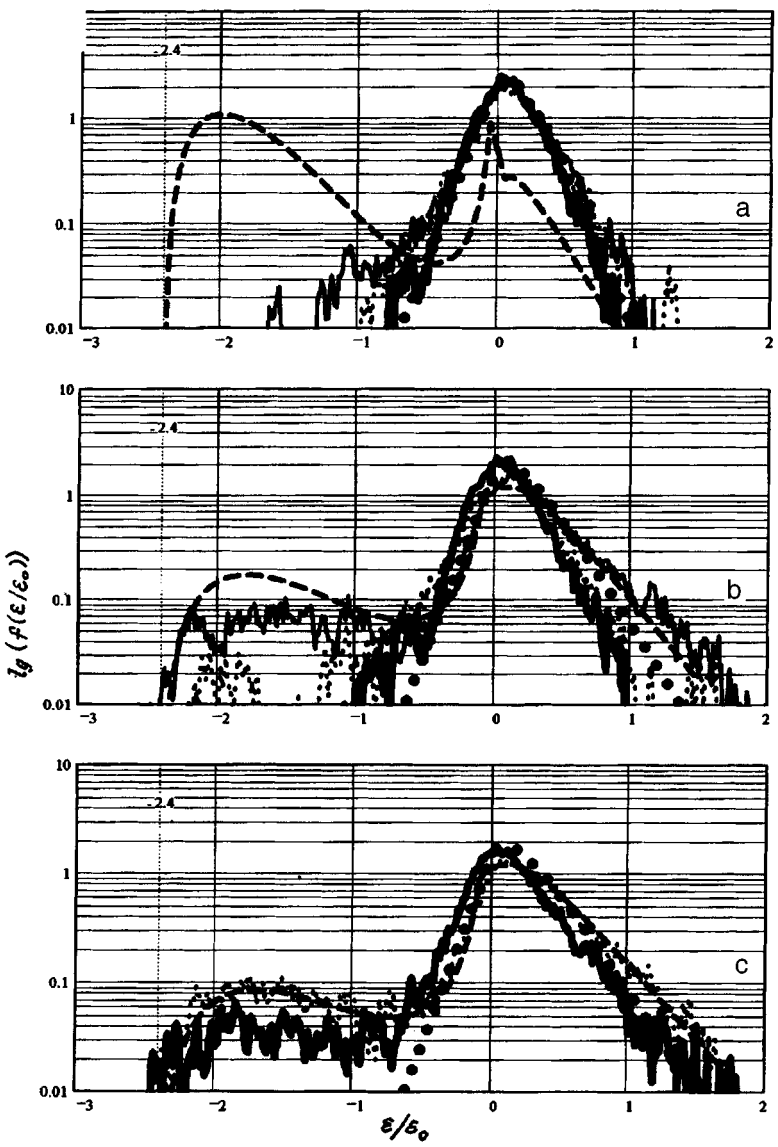

FIG. 2. Electron distribution function over the total energy ε for different time intervals. The distributions were obtained by averaging over a time segment of length corresponding to one Langmuir period. Energy is measured in units of $\varepsilon_0 = 20e^2 N_e^{1/3}$, which corresponds to the distance at which the charged spheres touch; the energy of the bottom of the well is indicated. a) Absence of permutational stochastization. At $t=5$ the system is reversed. Heavy line — averaging over the first Langmuir period; dotted line — averaging over the fifth period; solid line — averaging over the tenth period; heavy dotted line — microfield distribution:[1,2]

$$Y(y) = \frac{2C}{\sqrt{\pi}} \begin{cases} \sqrt{y}\,\exp(-y), & y > \alpha\gamma, \\ C_3 \exp(C_1 y + C_2 y^2/2), & |y| \leqslant \alpha\gamma, \\ C_4 \exp(\beta y/\gamma), & y - \alpha\gamma, \end{cases}$$

where $\alpha = 1.5$, $\beta = 0.4$; the constants ensure continuity and normalization of the function to unity; the dashed line corresponds to a Boltzmann distribution.[5] The microfield and Boltzmann distributions were constructed for the temperature $T_e = 0.023$ eV corresponding to the reversal point. b) Permutational stochastization over time intervals which are multiples of $\tau_p = 0.5$. Heavy line — averaging over the first Langmuir period; dotted line — averaging over the third Langmuir; solid line — averaging over the fourth period. The microfield and Boltzmann distributions were constructed for the temperature $T_e = 0.033$ eV corresponding to the last point in time in the calculation; c) permutational stochastization over time intervals which are multiples of $\tau_p = 0.1$. Heavy line — averaging over the first Langmuir period; dotted line — averaging over the fifth period. The microfield and Boltzmann distributions were constructed for temperature $T_e = 0.036$ eV corresponding to the last point in time in the calculation.

the recombination time (see Fig. 2c). A Boltzmann distribution is established not so much because of the formation of bound pairs as because of recombinational heating of the electrons. This is due to the large amount of energy released in a recombination event.

CONCLUSIONS

We shall now summarize.

1. The Lyapunov exponent for a classical Coulomb plasma is $L \approx 15/T_L$. Therefore the dynamic mixing of the phase trajectories takes place over a time of the order of several tenths of a Langmuir period. Appreciable loss of reversibility of the numerical solution and divergence of the coarse parameters of the plasma for initially close states arise at times an order of magnitude later, i.e., at times of the order of the Langmuir period.

2. The dynamic mixing of the phase trajectories occurs not over the entire energy surface but only on the part that corresponds to free-particle motion. This effect is to some extent analogous to the absence of mixing between some tori in the phase space of a system of weakly coupled harmonic oscillators (consequence of the well-known KAM theorem).[6]

3. Some types of stochastic perturbation of a dynamical system (specifically, the imprecision of the numerical solution and permutational stochastization) mix trajectories of the system that lie in different regions of energy space. This results in recombination.

The above-stated points confirm the concept of external stochastization, summarized in Refs. 1 and 2. We assume that collective plasma oscillations impede mixing of the translational and ionization degrees of freedom.[8] They give rise to an anomalous electron drift along the energy axis.[1,2] However, this question requires additional investigation.

[1] S. A. Maĭorov, A. N. Tkachev, and S. I. Yakovlenko, Usp. Fiz. Nauk **164**, 298 (1994).
[2] S. A. Mayorov, A. N. Tkachev, and S. I. Yakovlenko, Phys. Scripta **51**, 498 (1995).
[3] A. N. Tkachev and S. I. Yakovlenko, Pis'ma Zh. Tekh. Fiz. **21**(22), 90 (1995) [Tech. Phys. Lett. **21**, 946 (1995)].

[4] S. A. Maĭorov, A. N. Tkachev, and S. I. Yakovlenko, Pis'ma Zh. Tekh. Fiz. **17**(23), 33 (1991) [Sov. Phys. Tech. Phys. Lett. **17**, 836 (1991)].
[5] A. N. Tkachev and S. I. Yakovlenko, Kratk. Soobshch. Fiz., No. 9–10, 3 (1996).
[6] A. Lichtenberg and M. Lieberman, *Regular and Stochastic Motion*, Springer-Verlag, New York, 1983 [Russian translation, Mir, Moscow, 1984].
[7] S. A. Maĭorov, A. N. Tkachev, and S. I. Yakovlenko, Fiz. Plazmy **20**, 1107 (1994).
[8] A. N. Tkachev and S. I. Yakovlenko, Kratk. Soobshch. Fiz., No. 11–12, 67 (1995).

Translated by M. E. Alferieff

Thermomechanical effect in a hybrid-oriented nematic liquid crystal

R. S. Akopyan, R. B. Alaverdyan, É. A. Santrosyan, and Yu. S. Chilingaryan

Erevan State University
(Submitted December 20, 1996)
Pis'ma Zh. Tekh. Fiz. **23**, 77–81 (September 12, 1997)

The first experimental observation of a thermomechanical effect in a homeotropically planar-oriented nematic liquid crystal is reported. The effect consists of the appearance of a hydrodynamic flow induced by a longitudinal temperature gradient. The measured value of the thermomechanical coefficient agrees well with the theoretical estimate. © *1997 American Institute of Physics.* [S1063-7850(97)01309-8]

1. Thermomechanical effects in cholesteric liquid crystals were predicted and investigated experimentally in Refs. 1–3. These effects are due to the chirality of cholesterics, i.e., the absence of right-left symmetry in them. The first systematic theory of thermomechanical effects in deformed liquid crystals was constructed in Ref. 4, where a number of new thermomechanical effects were predicted. Spatial symmetry considerations show that these effects require a spatial nonuniformity of the unperturbed distribution of the director. The thermomechanical constants were also estimated. According to Ref. 5, first-order terms in the gradients of the velocity, director, and temperature are absent in the dissipative function because they are not invariant under time reversal. However, if it is assumed that the thermomechanical constants are pseudoscalar quantities, then the dissipative function in Ref. 4 remains invariant under time reversal. Furthermore, the experimental observation of a rotation of matter in nematic layers, which are in a field of a longitudinal temperature gradient, in a horizontal plane is reported in Ref. 6. The value of the pseudoscalar thermomechanical constant $\xi \sim 10^{-11}$ N/deg was calculated from the experimental data and is in good agreement with the theoretical calculations performed in Ref. 4.

In the present work the appearance of hydrodynamic flows as a result of a temperature gradient in a hybrid-oriented nematic liquid crystal (NLC) is studied experimentally and theoretically.

2. A hybrid-oriented NLC MBBA with a nematic phase interval of 20–47 °C was used in this work. A sandwich-type cell was arranged in a strictly horizontal plane and heated from below by a continuous transparent heater which provided uniform (to within ± 0.01 °C) heating in the horizontal plane and made it possible to observe textures in a polarization microscope (Fig. 1). The temperature difference between the bottom and top surfaces of the film was determined, just as in Ref. 6, as the difference of the temperatures of the transition into the isotropic phase in the bottom and top layers. The velocity **V** was determined as the maximum velocity of small (2–3 μm) aluminum oxide particles.

The geometry of the experiment is shown in Fig. 1a and 1b. The dotted lines represent the distribution of the director in the (x,z) plane. In the experiment, when the cell substrate, which set the planar orientation of the NLC, was on top (case *a*), a flow of the liquid crystal in the direction of the x axis was observed. When the cell was rotated around the z axis, the flow remained and was always directed along the easy-orientation axis $\mathbf{e}_x$ on the substrate that set the planar orientation of the NLC. The maximum flow velocity for a cell with thickness $L=120$ μm and temperature difference $\Delta=4.7$ °C between the top and bottom surfaces was of the order of $\mathbf{V}\sim 0.4$ μm/s. The flow of the NLC is established after the liquid crystal reaches the edge of the cell. This is apparently due to the appearance of capillary forces there. The liquid crystal does not return to its initial position after the temperature gradient is switched off.

The experimental results in the case when the substrate that sets the planar orientation of the NLC molecules is on the bottom (case *b*) are qualitatively different from case *a*. The following dynamics of the hydrodynamic flow is observed. After the temperature gradient $\nabla_z T$ is switched on, a flow of the NLC in the positive direction of the x axis arises. The liquid crystal gradually stops after $\sim$15–20 min without reaching the edge of the cell and then the liquid starts to flow in the opposite direction. After the NLC returns to its initial position, the process repeats.

In summary, in the case *b* an oscillation of the liquid arises and continues for a long time (motion was observed for more than 10 h) when the temperature gradient is maintained constant. The hydrodynamic oscillations of the liquid crystal stop when the temperature gradient is switched off. The coordinate x of the edge of the liquid and the maximum flow velocity **V** as functions of time are presented in Fig. 2.

3. To make a theoretical analysis and to obtain numerical estimates, we shall assume that the boundary conditions are homeotropic orientation $\mathbf{n}(z=0)=\mathbf{e}_z$ at the wall $z=0$ and planar orientation $\mathbf{n}(z=L)=\mathbf{e}_x$ at $z=L$. Here **n** is the director of the NLC. Let the external heat sources maintain a temperature $T=T_0+\Delta T$ in the sections $z=0$ and a temperature $T=T_0$ in the section $z=L$. Then the temperature gradient $dT/dz\sim\Delta T/L$ produces a thermomechanical flow of the NLC in the direction of the x axis. In the geometry described above it can be assumed that $n_y=0$, $V_y=V_z=0$, and $\partial/\partial x=\partial/\partial y=0$. In the stationary state $(\partial/\partial t=0)$ the Navier–Stokes equation has the form[4]

$$dG_{zx}^{TM}/dz+dG'_{zx}=0. \tag{1}$$

Here $G_{zx}^{TM}+G'_{zx}$ are the zx components of the viscous stress tensor

$$G'_{zx}=\eta dV_x/dz, \tag{2}$$

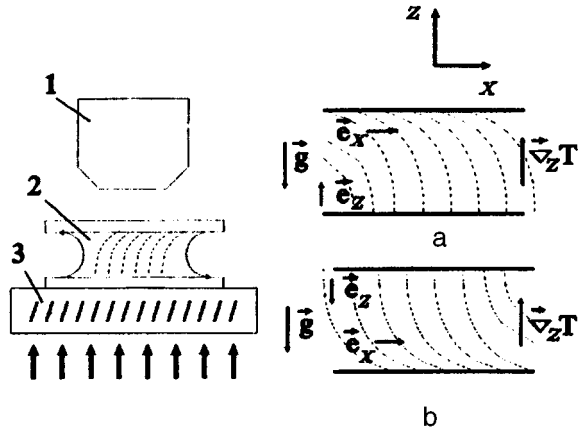

FIG. 1. Geometry of the experiment. 1 — Polarization microscope, 2 — cell with a nematic liquid crystal, 3 — transparent heater.

$$G_{zx}^{TM}=\pi dT/8Ldz[n_x^2(-2\xi_1-2\xi_5\xi_3-\xi_7)+n_z^2(\xi_7-\xi_3+\xi_{11}+2\xi_{12})+n_z^4(\xi_3-\xi_4-\xi_7+\xi_8-\xi_{11}-\xi_{12})+n_x^2n_z^2(\xi_3-\xi_4+\xi_7-2\xi_9+4\xi_{10}-4\xi_{12})], \quad (3)$$

where η is the viscosity, $dT/dz=\Delta T/L$ is the temperature gradient, and $\xi_1-\xi_{12}$ are the pseudoscalar thermomechanical constants. We obtain the solution of equations (1) for the thermomechanical flow velocity in the form

$$V_x=\xi\pi\Delta T/\eta L, \quad \xi=\xi_1-\xi_5+\xi_8+\xi_9+2\xi_{10}. \quad (4)$$

Using the experimental data $L=120$ μm, ΔT=4.7 °C, $\eta=1$ P, and $\mathbf{V}=0.4$ μm/s, we obtain for the thermomechanical coefficient $\xi=10^{-12}$ N/°C , in good agreement with the theoretical estimates.[4]

In summary, in the present work a thermomechanical effect in a hybrid–oriented nematic liquid crystal was observed for the first time. One of the twelve required relations between the twelve thermomechanical coefficients was obtained empirically: Another eleven independent experiments must be designed and performed in order to measure the coefficients experimentally. We intend to perform some of these experiments in the future (for example, the thermomechanical effect in a twist-nematic).

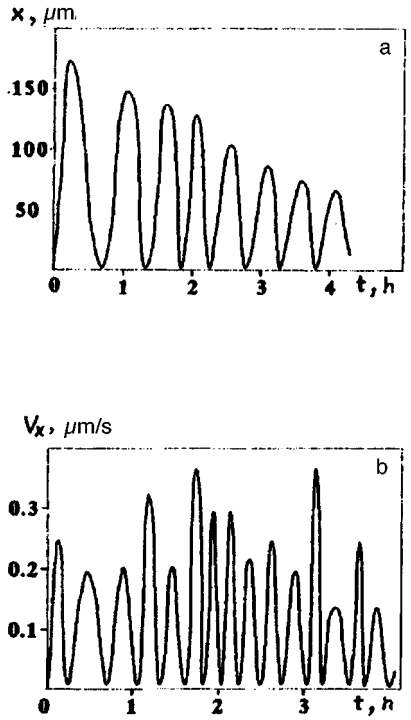

FIG. 2. Time dependence of the coordinate x of the edge of the liquid (a) and of the absolute value of the maximum velocity V_x (b).

[1] F. M. Leslie, Proc. R. Soc. Ser. A, 307 (1968).
[2] M. J. Stephen and J. P. Straley, Rev. Mod. Phys. **46**, 617 (1974).
[3] N. Eber and I. Janossy, in *Proceedings of the 4th Liquid Crystal Conference of Socialist Countries*, Tbilisi, USSR, 1981, Vol. 11, p. 125.
[4] R. S. Akopyan and B. Ya. Zel'dovich, Zh. Éksp. Teor. Fiz. **87**, 1660 (1984) [Sov. Phys. JETP **60**, 953 (1984)].
[5] H. R. Brand and H. Pleiner, Phys. Rev. A **5**, 7 (1987).
[6] O. D. Laverntovich and Yu. A. Hastishin, Ukr. Fiz. Zh. **32**(5), 710 (1987).

Translated by M. E. Alferieff

GaAs nanolayers obtained by pulsed cooling of a saturated fluxed melt

I. E. Maronchuk, A. I. Maronchuk, and A. V. Shorokhov

Kherson Industrial Institute, Kherson, Ukraine
(Submitted March 19, 1997)
Pis'ma Zh. Tekh. Fiz. **23**, 82–86 (September 12, 1997)

A new method is proposed for obtaining nanolayers. The method is based on pulsed cooling of a saturated fluxed melt. The layers obtained were investigated with the aid of photoluminescence. The results show a high quantum yield of luminescence and therefore high quality of the layers grown. © *1997 American Institute of Physics.* [S1063-7850(97)01409-2]

The method of pulsed cooling of a saturated fluxed melt that makes it possible to obtain submicron layers is described in Ref. 1. In the present letter we present photoluminescence spectra of nanolayers and quantum-size doped gallium arsenide superlattices obtained by this method.

To grow epitaxial layers by pulsed cooling, a plate with temperature $T_1 < T_0$, called the heat absorber, is placed against the back side of the substrate, which is at temperature T_0 in thermodynamic equilibrium with a saturated fluxed melt. Crystallization of an epitaxial nanolayer occurs on the front face of the substrate as a result of the pulsed cooling of the substrate. According to the analysis performed in Ref. 1 of the heat and mass transfer processes occurring under nonequilibrium conditions, the thickness of the layer obtained is determined by the temperature and thickness of the heat absorber in accordance with the expression

$$d = \frac{M_1 \rho_2 D}{M_2 \rho_1 m} \int_0^{t_0} \left. \frac{\partial T}{\partial z} \right|_{z=0} dt,$$

where m is the tangent of the slope angle of the liquidus line; $M_{1,2}$ and $\rho_{1,2}$ are the molar masses and density of GaAs and Ga; D is the diffusion coefficient of arsenic in gallium; the coordinate z is directed along the normal to the surface of the substrate and is measured from the crystallization front; and, t_0 is the growth time.

Growth was conducted on semi-insulating GaAs substrates with $\rho > 10^7\ \Omega \cdot$cm and (100) surface orientation. The substrates were subjected to the standard treatment in a polishing etchant. The growth apparatus made it possible to move the substrate between fluxed melts with different compositions and to obtain both nanosize and bulk (in the process of forced cooling of a saturated fluxed melt) epitaxial layers on 5×10 mm substrates.

To observe the luminescence properties of the nanolayers, undoped structures containing a single GaAs nanolayer between two bulk $Al_{0.7}Ga_{0.3}As$ layers with thickness of the order of 2 μm, similar to those described in Ref. 2, were grown. First, a bulk epitaxial $Al_{0.7}Ga_{0.3}As$ layer was grown on a GaAs substrate in the process of forced cooling of a saturated fluxed melt. Next, a GaAs epitaxial nanolayer was grown by pulsed cooling of a saturated GaAs solution in a gallium melt and a second bulk layer with composition $Al_{0.7}Ga_{0.3}As$ was grown on the surface of this nanolayer by the method of forced cooling. Thus, a single nanolayer was confined between two bulk layers of a wide-gap solid solution.

Doped superlattices were grown by pulsed cooling, moving the substrate between fluxed melts containing the *p*-type (germanium) and the *n*-type (tin) impurity and at each position putting the substrate in contact with the heat absorber with temperature T_1.

The photoluminescence of the heterostructures and superlattices obtained was excited at a temperature of 77 K by an argon laser with intensity ranging from 40 to 500 W/cm^2.

Figure 1 displays the photoluminescence spectrum of a GaAs nanolayer with an excitation intensity of 300 W/cm^2. The layer was obtained at temperature $T_0 = 700$ °C using a heat absorber with thickness $\delta = 3$ mm and temperature

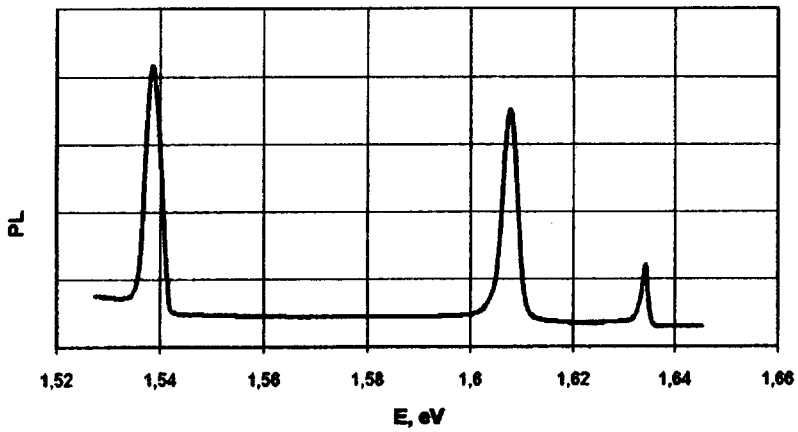

FIG. 1.

 1063-7850/97/090692-02$10.00

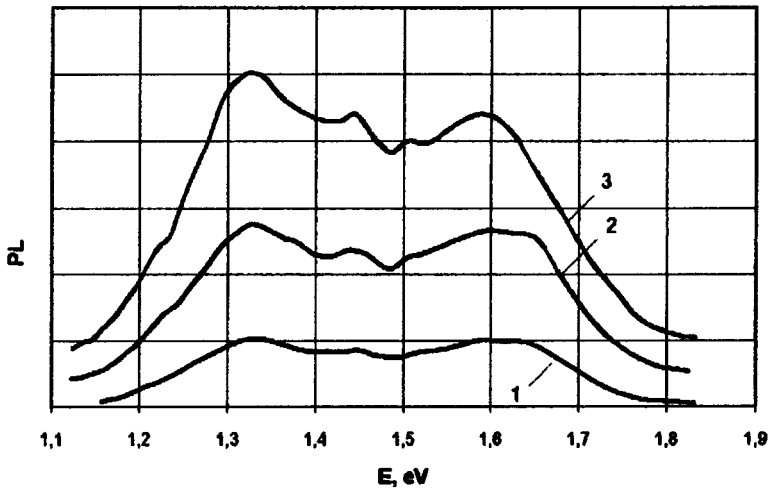

FIG. 2.

$T_1 = 660$ °C. The position of the maxima of the peaks agrees well with the result of a calculation of the energy spectra of particles in a potential well performed in the effective-mass approximation. The band with a maximum at 1.538 eV consists of unresolved peaks, formed by recombination of electrons and heavy and light holes in the first quantum state. The bands with maxima at 1.607 and 1.634 eV are due to transitions between the second electronic quantum level and the second heavy- and light-hole levels. The splitting between the energy levels makes it possible to determine the thickness of the nanolayer — 14 nm, which agrees with the computational results obtained with equation (1) for the indicated technological parameters (see Ref. 1, Fig. 1).

It was determined on the basis of the photoluminescence investigations at different points of the surface of the samples that the nonuniformity of the layers obtained does not exceed 1 nm on an area of 0.5 cm^2.

Figure 2 displays photoluminescence spectra of a superlattice containing 25 alternating *n*- and *p*-layers obtained at a temperature of 750 °C with a 3-mm thick heat absorber at a temperature of 715 °C. The layers were doped with Sn and Ge, respectively (doping level — 5×10^{18} cm^{-3}). The excitation intensities were 40 (curve *1*), 100 (curve *2*), and 200 W/cm^2 (curve *3*).

Photoluminescence is observed in the interval from 1.15 to 1.8 eV. The long-wavelength photoluminescence is due to recombination via an indirect (in real space) band gap between the electrons near the bottom of the subbands of the conduction band and the valence-band holes spatially separated from them. The intensity of the photoluminescence in this region of the spectrum is high because the lifetime of the excited carriers is substantially higher as a result of the spatial separation of the electrons and the holes. In consequence, the electron–hole recombination rate remains high even with an effective band gap less than the band gap E_g in gallium arsenide. The large width of the band in the region $E<E_g$ is explained by the fact that the contributions of the recombination of carriers from several subbands add.[3]

The photoluminescence intensity increases with excitation level linearly in the long-wavelength region and sublinearly in the short-wavelength region.

The photoluminescence in the short-wavelength region of the spectrum with energy $E>E_g$ is due to vertical recombination of electrons and holes from subbands in the conduction and valence bands. The sublinear dependence of the photoluminescence intensity on the excitation level in this region of the spectrum is due to the fact that the excited states in the top subbands are emptied by vertical recombination as well as by thermalization to the bottom subbands followed by tunneling recombination of spatially separated carriers.

The high intensity of the photoluminescence of nanostructures and doped superlattices obtained by pulsed cooling of a saturated fluxed melt shows that the density of point defects, which produce centers of nonradiative recombination, is low in them. Furthermore, the results obtained show that the parameters of the structures are highly uniform on a sample area of 0.5 cm^2.

[1] T. F. Kulyutkina, I. E. Maronchuk, and A. V. Shorokhov, Pis'ma Zh. Tekh. Fiz. **21**(20), 1 (1995) [Tech. Phys. Lett. **21**, 815 (1995)].
[2] Zh. I. Alferov, V. M. Andreev, A. A. Vodnev *et al.*, Pis'ma Zh. Tekh. Fiz. **12**, 1089 (1986) [Sov. Tech. Phys. Lett. **12**, 450 (1986)].
[3] M. Herman, *Semiconductor Superlattices* [Russian translation], Mir., Moscow, 1989.

Translated by M. E. Alferieff

Mass-spectrometric investigation of the formation of volatile products accompanying heating of a copolymer of trifluorochloroethylene with vinylidene fluoride

A. O. Pozdnyakov and B. M. Ginzburg

Institute of Mechanical Engineering Problems, Russian Academy of Sciences, St. Petersburg
(Submitted April 3, 1997)
Pis'ma Zh. Tekh. Fiz. **23**, 87–92 (September 12, 1997)

The mechanisms of thermal degradation of copolymers of trifluorochloroethylene with vinylidene fluoride are investigated at the molecular level by thermal desorption mass spectrometry. It is shown that HCl and HF are released in two stages. The low-temperature stage is not related with the destruction of the main chain and is due to the formation of rare intermolecular cross-links (one or two per two chains). The high-temperature stage is observed in the same temperature interval as are other products of thermal degradation which attest to depolymerization processes taking place. © *1997 American Institute of Physics.* [S1063-7850(97)01509-7]

Investigations of changes taking place in the molecular structure as a result of heating of solid polymer systems are of scientific and practical interest. The changes taking place in the molecular structure and properties of the KeI-F type copolymer of trifluorochloroethylene with vinylidene fluoride, widely used in practice as heat-resistant rubbers and coatings of different types, were studied in Refs. 1–3 by different physical and physicochemical methods.[4] It was found that there exist two temperature regions (200–300 °C and above 300 °C) with a different character of the thermal degradation. In the case of heating in vacuum, a decrease of solubility of the polymer (formation of a network), a change in color of the polymer, and release of the hydrogen halides HF and HCl were observed in the temperature range 200–300 °C. In Refs. 1–3 the change in color was attributed to the formation of a system of conjugate bonds in an intramolecular HF and HCl detachment reaction. In confirmation of the results, it was observed that when the copolymer is heated for a long period of time the change in the color of the polymer is accompanied by the appearance of absorption bands, characteristic for a system of conjugate bonds, in the IR spectra. The conjugate bonds were not observed in the case of heating at lower temperatures or at early stages of heating (5–10 h) at 300°C. It was concluded in Refs. 1–3 that the decrease in solubility of the polymer and the formation of a network are not due to the release of HF and HCl. A comparison of solubility changes with titrometric and potentiometric measurements of the quantities of HF and HCl that accumulated during heating led to the same conclusions. Furthermore, according to the data obtained, the products of thermal degradation at 340–380 °C did not contain ''monomeric substances'' of the copolymer, which led to the conclusion that, for all practical purposes, depolymerization reactions do not occur during the thermal degradation of KeI-F.[3]

It should be noted that the experimental methods employed in Refs. 1–3 (titration, potentiometry) did not permit recording the entire spectrum of the products of thermal degradation, the total amount of such products, or the continuous distribution of the yield with increasing temperature and they did not always permit an unequivocal identification of the nature of these products.

In the present work we employed thermal-desorption mass spectrometry,[5] which does not have these drawbacks. We studied the yield of practically the entire spectrum of volatile products released during heating of the copolymer of trifluorochloroethylene with vinylidene fluoride in the entire temperature interval, right up to complete decomposition of the copolymer. The high sensitivity of the method and its technical possibilities made it possible to obtain new experimental data on the structural transformations of the copolymer of trifluorochloroethylene with vinylidene fluoride which take place when the copolymer is heated. The results obtained gave not only new information but they also make it necessary, in our view, to reexamine some previously drawn conclusions.[1–3]

We employed the F-32 copolymer of trifluorochloroethylene with vinylidene fluoride ($M_n \cong 1.2\times 10^5$) with a 3:1 molar ratio of trifluorochloroethylene to vinylidene fluoride. A solution of the copolymer of trifluorochloroethylene with vinylidene fluoride in ethyl acetate (3 mass%) was used to obtain the films. The films were deposited on steel foils which were carefully degreased in organic solvents and annealed in high vacuum. The average film thickness (after removal of the solvent), determined according to the density of the material deposited on the substrate and the area occupied by the film, was equal to 5000 Å.

A magnetless MSKh-6 time-of-flight mass spectrometer, modified by attaching a special vacuum chamber for heating the sample, was used to study the volatile products of thermal degradation. The pressure in the chamber of the mass spectrometer before the experiment was maintained at 10^{-5} Pa. Under the experimental conditions the rate of formation dN_i/dt of the volatile products is related with the height of the peak by the linear relation $dN_i/dt = k_i A \cdot h_i$, where k_i is the relative sensitivity of the apparatus to the flow of the ith material and A is the absolute sensitivity of the apparatus. The absolute sensitivity of the apparatus to the flow of the methyl methacrylate vapors[5] and the tabulated values of the relative sensitivities of the compounds of interest to us were used to calculate dN_i/dt.

A panoramic mass spectrum of the volatile products formed during heating of the copolymer of trifluorochloroethylene with vinylidene fluoride in the range 300–450 °C is

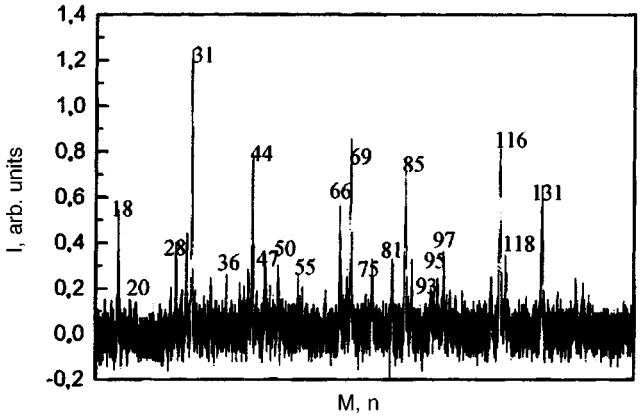

FIG. 1. Panoramic mass spectrum of volatile products which are given off from the copolymer of trifluorochloroethylene with vinylidene fluoride during heating in the temperature range 300–550 °C. The numbers near the peaks represent the mass in atomic mass units.

displayed in Fig. 1. The identification of the mass spectra makes it possible to ascribe the observed lines to trifluorochloroethylene (116, 31, 66), 1-propane, 3-chloro-1, 1, 2, 3, 3-pentafluorine (131, 69, 31), pentafluorochloroethane (85, 69, 31), and the hydrogen halides HF (20) and HCl (35, 36, 37, 38). The formation of these products was also observed in Ref. 6. The temperature dependence of the rate of formation of some of the main volatile products of degradation accompanying heating of the copolymer is shown in Fig. 2.

The peak yield of trifluorochloroethylene and the unimodal peaks due to 1-propane, 3-chloro-1, 1, 2, 3, 3-pentafluorine, and pentafluorochloroethane, observed in the same temperature interval but not shown in the figure, are evidently due to the depolymerization of the main chain.

In contrast to the yield of the products of thermal degradation of macromolecules, HF and HCl are released in two stages. The high-temperature stage is observed in the same temperature range as are the products of thermal destruction of the chains. The low-temperature stage (170–320 °C) of HF and HCl release is not associated with depolymerization and can be explained by the formation of intermolecular cross-links, in agreement with the decrease in the solubility of the copolymer in the corresponding temperature range.[3] Assuming that each HF and HCl molecule corresponds to the formation of one cross-link and knowing the molecular mass and the weight of the polymer investigated, we find that there are one or two cross-links per two macromolecules. The number of cross-links on fluorine atoms is higher than that on chlorine atoms, apparently because the copolymer contains more fluorine-containing units. Taking account of the fact that intramolecular cross-links (for example, between neighboring sections of the macromolecules in crystallites with folding chains) can form in addition to intermolecular cross-links, the number of intermolecular cross-links can be even less than one per two molecules. Therefore the network formed is very sparse. It is obvious that not all macromolecules participate in the network and, in addition to the network, there exists a soluble part of the sample, as is confirmed by the published data.[3]

In summary, in the present work it has been shown by a

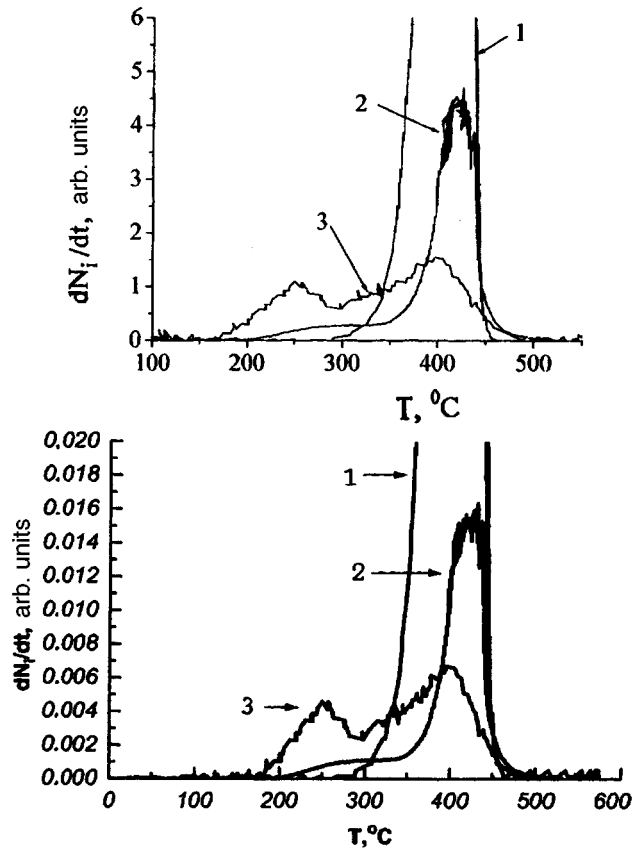

FIG. 2. Temperature dependence of the rate of formation of some products of thermal degradation of the copolymer of trichlorofluorethylene with vinylidene fluoride: *1* — trifluorochloroehtylene CF_2CFCl ($m/e=116$ Da); *2* — HCl ($m/e=36$ Da); *3* — HF ($m/e=20$ Da).

direct method that the hydrogen halides HF and HCl are released in two stages during thermal degradation of the copolymer of trifluorochloroethylene with vinylidene fluoride. The low-temperature stage is not related with the destruction of the main chain and apparently gives rise to the formation of sparse intermolecular cross-links. The high-temperature stage of the release of hydrogen halides occurs in the same temperature interval as the release of other products of thermal degradation which attest to the depolymerization processes taking place.

This work was performed as part of the Russian Scientific and Technical Program ''Fullerenes and Atomic Clusters'' (Project Tribol).

[1] T. G. Degteva, Vysokomol. Soedin. **3**, 671 (1961).
[2] T. G. Degteva, I. M. Sedova, and A. S. Kuz'minskiĭ, Vysokomol. Soedin. **5**, 378 (1963).
[3] T. G. Degteva, I. M. Sedova, and A. S. Kuz'minskiĭ, Vysokomol. Soedin. **5**, 1485 (1963).
[4] Yu. A. Panshin, S. G. Malkevich, and Ts. S. Dunaevskaya, *Fluoroplastics* [in Russian], Khimiya, Leningrad, 1978.
[5] A. V. Amelin, Yu. A. Glagoleva, O. F. Posdnyakov, and V. R. Regel', Prib. Tekh. Éksp., No. 4, 152 (1968).
[6] R. H. Boyd, in *Thermal Stability of Polymers*, edited by R. T. Conley, Marcel Dekker, New York, 1970, p. 47.

Translated by M. E. Alferieff

Observation of improved confinement at the center of a FT-2 tokamak plasma with rapid current rise and lower-hybrid heating

V. N. Budnikov, V. V. Bulanin, V. V. D'yachenko, N. A. Zhubr, L. A. Esipov, E. R. Its, S. I. Lashkul, A. Yu. Popov, A. Yu. Stepanov, I. E. Sakharov, and A. S. Tukachinskiĭ

A. F. Ioffe Physicotechnical Institute, Russian Academy of Sciences, St. Petersburg; St. Petersburg State Technical University

(Submitted May 15, 1997)
Pis'ma Zh. Tekh. Fiz. **23**, 1–6 (September 26, 1997)

The problem of optimizing the conditions for central lower-hybrid heating has stimulated experiments with improved confinement at the center of the discharge in analogy to discharges with an inverted shear of the q profile. To this end, a current pulse rising rapidly from 22 to 30 kA over 0.5 ms was used in the FT-2 tokamak during lower-hybrid heating. In these experiments a substantial increase in the lifetime of the energy in the ionic component was observed. A decrease of the fluxes of high-energy charge-exchange atoms and a suppression of the microoscillations of the plasma determined in the central regions of the discharge are observed. These and other data were used together with the computer simulation to clarify the mechanism leading to the improvement of energy and particle confinement at the center of the discharge. The influence of variations in both the q profile and the electric fields, which accompanied the rapid current rise, on the transport processes is studied. © *1997 American Institute of Physics.* [S1063-7850(97)01609-1]

A transition of the plasma in a FT-2 tokamak into a regime with improved confinement was observed in experiments on lower-hybrid heating. The transition was identified, on the basis of all indications, as a transition into the H mode with the appearance of a transport barrier at the periphery of the discharge.[1,2] This showed that despite the small size of the setup ($R=0.55$ m, $a=0.08$ m, $B_t=2.2$ T, $I_{pl}=2$ kA, $t_p=50$ ms) the plasma manifests the same properties in the bifurcation of the state that are characteristic for large setups. This fact as well as the problem of optimizing the conditions for lower-hybrid heating stimulated new experiments with an attempt to organize improved confinement at the center of a discharge in analogy to super shot or hot-ion-mode type discharges or a discharge with an inverted shear of the q profile (see, for example, Refs. 3 and 4).

For these purposes, a current pulse rising rapidly from 22 to 30 kA ($\Delta t_I=2.5$ ms and rise time $\Delta t=0.5$ ms) was used in the FT-2 tokamak during lower-hybrid heating ($P_{\rm rf}=90$ kW, $f=920$ MHz, $\Delta t=4$ ms). The following were observed in these experiments:

1. A substantial (by a factor of 1.5–2) decrease in the flux of high-energy charge-exchange atoms with $E>1000$ eV with the flux determined by the thermal ions in the plasma remaining unchanged or increasing. Such fluxes of neutrals with energies $E=1900$, 1300, and 650 eV for the cases of one rf heating and $\Delta I+$ rf simultaneously are compared in Fig. 1. The figure also displays oscillograms of I_{pl}, U_{pl}, and the plasma emission in the H_β line.

2. A large (by approximately a factor of 2–3) increase in the lifetime of the energy in the ionic component. This time was determined according to the growth and decay of the central ionic temperature. In a number of experiments it was comparable to the particle lifetime. Figure 2 displays the changes in the central ionic component for three different scenarios of the discharge: (a) one rapid current rise ΔI, (b) only one additional rf heating, and (c) rf and ΔI together.

3. A characteristic increase in the plasma density. This increase is explained by an increase in the particle lifetime at the center of the discharge. The dense central core remained for more than 5 ms even in the postheating stage. The plasma density profiles $n_e(r)$ for four times (ohmic heating, at the end of the rf pulse, and 5 and 10 ms after the additional heating was switched off) are displayed in Fig. 3.

4. Factor of 2–3 increase in the rate of revolution of the plasma. This result was obtained in the course of a cross-correlation analysis of the signals from MHD probes.

5. Substantial suppression of the microoscillations of the plasma in the central regions of the discharge, as determined by scattering of CO_2 laser radiation. The measurements were performed in the frequency range 100–800 kHz. Diagnostics made it possible to investigate fluctuations of the electron density in the wave number range $k_\perp=12-30$ cm^{-1}. The CO_2 laser radiation was detected at small scattering angles in a volume extending in the vertical dirtection along the probing laser pulse. Signals obtained by probing along the central chord and along a chord displaced by 6 cm to the side were compared in the experiment. Suppression of plasma oscillations detected along the central chord was observed with a rapid rise in the current as well as with $\Delta I+$ rf. Measurements of the scattered radiation with probing along the peripheral chord showed that the fluctuation level does not change here. In the case of rf heating alone, however, the microoscillations of the plasma were not suppressed either at the center or at the periphery.[5]

Thus in our experiment with a rapidly rising current all indications of a transition to improved confinement at the center of the discharge are observed, just as in large setups, such as TFTR, DIII–D, and Tore Supra.[3,4] In all of these cases improved confinement at the center of the plasma column was observed at the stage of plasma current growth with

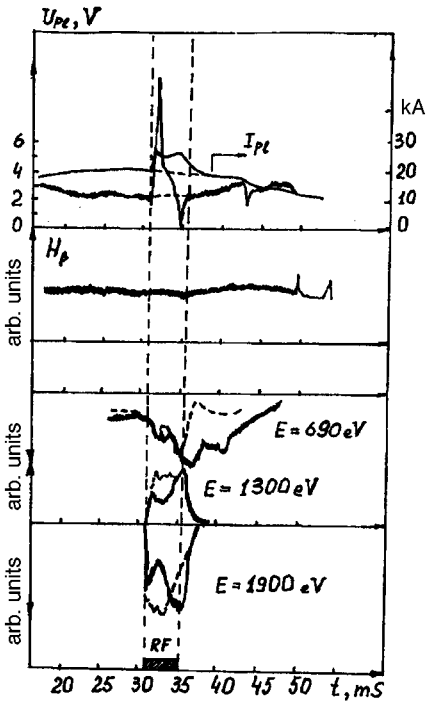

FIG. 1. Oscillograms of the main parameters of the discharge: plasma current — I_{pl}; voltage on the circumference of the plasma filament — U_{pl}; H_β line radiation from the plasma and fluxes of charge-exchange neutrals with energies $E=1900$, 1300, and 650 eV, presented for two different cases of longitudinal heating: rf (light dashed line) and combined rf + ΔI.

additional heating or in the entrainment-current regime. In these works it was shown experimentally that a negative shear of the q profile forms in the discharge. The decrease in heat transfer could be due to this fact. In our case, such direct measurements were not available, but a simulation with the ASTRA code shows that under the experimental conditions in a FT-2 tokamak after $\Delta\tau=1-2$ ms an appreciable flattening of the current density profile occurs at the center, and this could result for the region $r\leqslant 2$ cm in low values of the

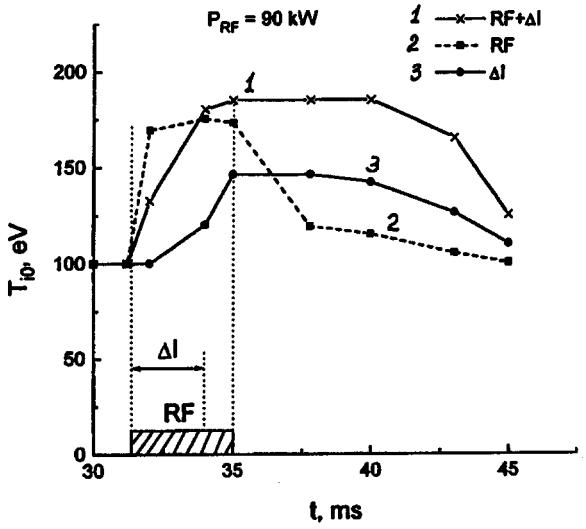

FIG. 2. Behavior of the ion temperature in three cases: rapid current rise — ΔI; rf + ΔI; and, on rf heating.

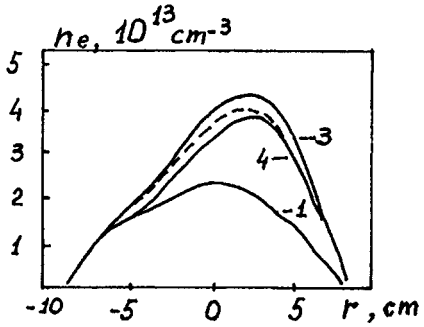

FIG. 3. Plasma density profiles $n_e(r)$ in the rf + ΔI experiment for four times: *1* — 30th ms, ohmic heating; *2* — 35th ms (dashed curve); *3* — 37th ms; and, *4* — 40th ms.

shear $s=(r/q)(dq/dr)\sim 0$. This makes it possible to attribute the observed phenomena to restructuring of the profile of the current channel. At the same time, it is interesting that the decrease in the fluxes of the fast component of the charge-exchange neutrals, just as suppression of the fluctuations, starts earlier, i.e., immediately after the current starts to rise. This suggests that as the current in the plasma increase, processes associated not only with the diffusion of longitudinal electric fields, which change the current density profile, but also processes due to a sharp change in the radial distribution of these fields themselves appear. We conjecture that in this case the Ware pinch should play an important role.[6] Specifically, at the initial stage of current rise there arises a gradient $\nabla_r E_\parallel$ such that the longitudinal electric field at the periphery of the discharge becomes several times greater than its value at the center. In this case, for such large $E_\parallel$ the inward-directed flux of locked particles $\sim\sqrt{\varepsilon}cE_\parallel/B_p$ can compensate and even exceed their diffusion losses. At the same time, the longitudinal velocity of the ensemble of locked ions should also increase. Intensification of the pinching as well as an increase in the longitudinal velocity could appreciably change the fraction of locked ions. This can explain the drop in the fluxes of high-energy charge-exchange atoms, measured with an analyzer in the $\Delta I+$ rf experiment (paragraph 1 above). The processes associated with the pinching of charged particles could ultimately influence the distribution of the radial electric fields and the confinement times in the plasma.

It is evident from the facts presented above that the plasma processes accompanying a rapid rise in the current are complicated and require a more accurate theoretical and experimental study.

We thank F. X. Soldner (JET, UK) and V. A. Rozhanskiĭ (St. Petersburg State Technical University, Russia) for a discussion of the experimental results.

This work was sponsored by the Russian Fund for Fundamental Research, Project No. 95-02-04072, and INTAS–RFBR Grant 95-1351.

[1] V. N. Budnikov *et al.*, in *Proceeding of the 23rd EPS Conference on Controlled Fusion and Plasma Fusion*, Kiev, 1996, pp. 779–782.
[2] V. N. Budnikov, Pis'ma Zh. Tekh. Fiz. **23**(1), 53 (1997) [Tech. Phys. Lett. **23**, 32 (1997)].

[3] S. H. Batha *et al.*, Phys. Plasma **3**(4), 1348 (1996).
[4] E. J. Strait *et al.*, Phys. Rev. Lett. **75**, 4421 (1995).
[5] M. V. Andrejko, L. G. Askinazi, V. N. Budnikov *et al.*, IAEA-CN-64/AP2-13, Montreal, 1996.
[6] V. Rojanskii and M. Tendler, *Reviews in Plasma Physics*, edited by B.B. Kadomtsev, Consultants Bureau, N.Y., 1996, Vol. 19, p. 147.

Translated by M. E. Alferieff

Phase effects in a semiconductor laser with diffraction extraction of radiation

M. A. Kaliteevskiĭ, E. L. Portnoĭ, and G. S. Sokolovskiĭ

A. F. Ioffe Physicotechnical Institute, Russian Academy of Sciences, St. Petersburg,
(Submitted April 25, 1997)
Pis'ma Zh. Tekh. Fiz. **23**, 7–11 (September 26, 1997)

Phase effects arising in a semiconductor laser with diffraction extraction of radiation and a distributed Bragg reflector on the substrate side are taken into account exactly quantitatively and the possibilities of using these effects in lasers is analyzed. It is shown that the phase effects studied can be used to increase the laser efficiency substantially. © *1997 American Institute of Physics.* [S1063-7850(97)01709-6]

Semiconductor injection lasers with diffraction surface extraction of radiation possess a number of advantages over lasers in which radiation is extracted through the ends.[1,2] Some of the main advantages are a large surface for extracting radiation and a large output aperture associated with this surface. This results not only in a small divergence of the laser radiation[2] but it also removes a fundamental limitation on the radiation power of a laser due to ''catastrophic'' degradation of the output mirrors.[3] Diffraction gratings used for extracting radiation and for producing feedback make it possible to obtain unimodal radiation and to decrease the lasing line width.[4]

At the same time these lasers have some drawbacks, the main one being losses of the radiation diffracted in the direction of the substrate.[3] It should be noted that in many cases, on the basis of technological considerations, gratings operating in the second diffraction order are used to obtain feedback. In this case the efficiency of the device is also reduced by radiation losses in the first diffraction order.[5,6] Both problems can be solved if a multilayer Bragg mirror is placed under the waveguide layer. In the process, despite the apparent simplicity of the proposed solution, investigators[7–10] neglect the fact that it is necessary to take account of the phase relations between the waves diffracted in air, in the direction of the multilayer Bragg mirror, and the waves rereflected by the mirrors accurately. Our objective in the present Letter is to take into account quantitatively exactly the relations mentioned above and to analyze the possibility of using the observed effects in lasers.

Let us consider diffraction of a waveguide mode by a surface grating. The wave diffracted in air at the angle θ_0 is the result of a superposition of two waves (Fig. 1): the wave diffracted in air at the angle θ_0 (the amplitude of the wave is A_0) and the wave diffracted in the direction of the substrate at the angle θ_1 and rereflected by the Bragg reflector (the amplitude of the wave is A_1). We shall consider diffraction angles which are not less than $\pi/2$.

The phase difference $\Delta\varphi_{01}$ between these two waves is (Fig. 1)

$$\Delta\varphi_{01}=2dN_mK_0\sin\theta_1+2d\overline{n}K_0\frac{1}{\cos\theta_1}+\Delta\varphi_b(\theta_1), \quad (1)$$

where N_m is the effective refractive index of the waveguide mode, $\overline{n}$ is the ''averaged'' refractive index of the waveguide and the layers bounding it, d is the distance between the diffraction grating and the multilayer Bragg reflector, K_0 is the wave vector of light in the vacuum, and $\Delta\varphi_b(\theta_1)$ is the phase of the reflection coefficient of the Bragg reflector.

For light at normal incidence the phase difference is

$$\Delta\varphi_\perp=2d\overline{n}K_0+\Delta\varphi_b(0). \quad (2)$$

The phase $\Delta\varphi_b(\theta_1)$ near the Bragg-interference frequency of the Bragg reflector is virtually independent of the angle of incidence θ_1[11] and at the Bragg-interference frequency in the case of light at normal incidence it equals 0 or π depending on the order of alternation of the layers in the Bragg reflector.[11]

The resulting intensity $I=|A_0+A_1|^2$ depends on the phase difference of the waves A_0 and A_1, i.e. the Bragg reflector can both increase and suppress the diffraction extraction of radiation.[10]

It should be noted that the wave reflected from the Bragg reflector partially escapes from the system, is partially specularly reflected, and is partially diffracted into a waveguide mode propagating in the direction of the initial waveguide mode.

The idea of using a monolithic epitaxial structure with a multilayer Bragg reflector to produce a laser with diffraction surface extraction of radiation, where feedback is obtained with a diffraction grating operating in the second diffraction order so as to realize a one-frequency lasing regime and a multilayer Bragg mirror is used to suppress radiation losses in first order as well as to increase the diffraction extraction

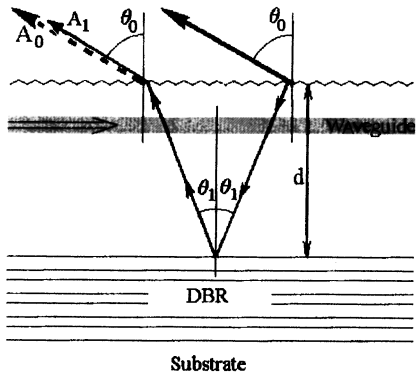

FIG. 1. Diagram illustrating the calculation of the phase relations in a system waveguide–surface grating–multilayer Bragg mirror.

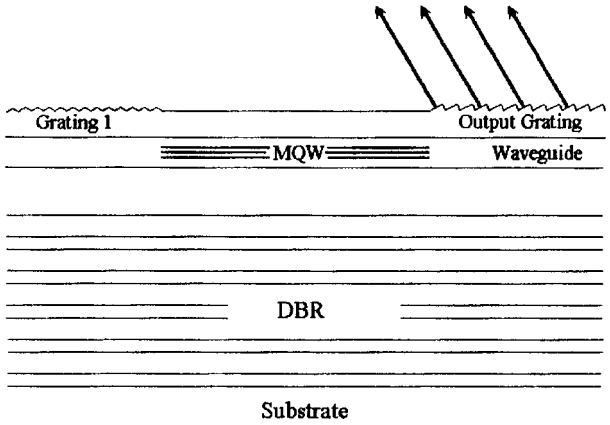

FIG. 2. Schematic diagram of the construction of the laser.

of radiation (Fig. 2), seems obvious. The spacing a of the diffraction grating, used to obtain feedback, is determined by the relation

$$a_1=\frac{2\cdot\pi}{N_m\cdot K_0}, \tag{3}$$

and the spacing of the diffraction grating through which radiation is extracted satisfies the condition

$$\frac{\pi}{N_m\cdot K_0}<a_2<\frac{2\cdot\pi}{N_m\cdot K_0}. \tag{4}$$

To suppress radiation losses in first diffraction order by the grating used to obtain feedback and to increase at the same time the efficiency of radiation extraction in the proposed structure the increase in the phase of the wave diffracted by a right angle must differ by $(2m+1)\pi$, where m is an integer, from the increase in the phase of the wave diffracted at an angle θ_1. Using the relations (1) and (2), this condition can be written as

$$2dN_mK_0\ \sin\ \theta_1+2d\overline{n}K_0\left(\frac{1}{\cos\theta_1}-1\right)$$
$$+\Delta\varphi_b(\theta_1)-\Delta\varphi_b(0)=(2m+1)\pi. \tag{5}$$

For small angles θ_1 only the first term in this formula differs appreciably from zero and the formula (5) in the case $\Delta\varphi=\pi$ and $N_m\approx\overline{n}$ becomes

$$d\approx\frac{\lambda}{4\cdot\sin\ _1}, \tag{6}$$

where λ is the wavelength in the material.

Thus, for the angle $\theta_1=5°$ the thickness d of the waveguide must be of the order of 2.5 wavelengths of the light in the material. For a GaAs/AlGaAs ($\lambda=0.9$ μm, $N_m\approx\overline{n}\approx3.5$) laser with radiation extraction angle $\theta_0\approx20°$ the diffraction angle in the substrate direction is $\theta_1\approx5°$. In this case the condition (5) holds for $d\approx0.6$ μm.

We thank the Russian Fund for Fundamental Research for support (Grant No. 96-02-17836-a).

[1] Zh. I. Alferov, V. M. Andreev, R. F. Kazarinov, E. L. Portnoĭ, and R. A. Suris, Inventor's Certificate USSR No. 392875, Applications No. 1677436 with priority from July 19, 1971. Bull. Izobret. No. 1, p. 259 (1977)].
[2] Zh. I. Alferov, S. A. Gurevich, R. F. Kazarinov, M. N. Mizerov, E. L. Portnoĭ, R. P. Seĭsyan, and R. A. Suris, Fiz. Tekh. Poluprovodn. **8**, 832 (1974) [Sov. Phys. Semicond. **8**, 541 (1974)].
[3] S. Yu. Karpov, V. I. Kuchinskiĭ, and E. L. Portnoĭ, Pis'ma Zh. Tekh. Fiz. **6**(3), 361 (1980) [Sov. Phys. Tech. Phys. Lett. **6**, 155 (1980)].
[4] Zh. I. Alferov, A. D. Vlasov, V. I. Kuchinskiĭ, M. N. Mizerov, E. L. Portnoĭ, and A. I. Uvarov, Pis'ma Zh. Tekh. Fiz. **3**(19), 987 (1977).
[5] S. Yu. Karpov, Zh. Tekh. Fiz. **48**, 1774 (1978) [Sov. Phys. Tech. Phys. **23**, 1009 (1978)].
[6] S. Yu. Karpov, V. I. Kuchinskiĭ, E. L. Portnoĭ, and V. B. Smirnitskiĭ, Zh. Tekh. Fiz. **48**, 362 (1978) [Sov. Phys. Tech. Phys. **23**, 214 (1978)].
[7] R. F. Kazarinov and C. H. Henry, IEEE J. Quantum Electronics **QE-21**, 144 (1985).
[8] C. H. Henry, R. F. Kazarinov, R. A. Logan, and R. Yen, IEEE J. Quantum Electronics **QE-21**, 151 (1985).
[9] A. Hardy, D. Welch, and W. Streifer, IEEE J. Quantum Electronics **25**, 2096 (1989).
[10] D. Mehuys, R. Parke, R. G. Waarts, D. F. Welch, A. Hardy, W. Streifer, and D. R. Scifres, IEEE J. Quantum Electronics **27**, 1574 (1991).
[11] E. L. Ivchenko, M. A. Kaliteevski, A. V. Kavokin, and A. I. Nesvizhski, J. Opt. Soc. Am. B **13**, No. 5. (1996).

Translated by M. E. Alferieff

Power characteristics of 2.2 μm LEDs for spectroscopic applications

A. A. Popov, V. V. Sherstnev, and Yu. P. Yakovlev

A. F. Ioffe Physicotechnical Institute, Russian Academy of Sciences, St. Petersburg
(Submitted April 7, 1997)
Pis'ma Zh. Tekh. Fiz. **23**, 12–18 (September 26, 1997)

The results of an investigation of the basic electric and power characteristics of 2.0–2.28 μm LEDs for spectroscopic measurements of nitrogen-containing molecules are reported. Room-temperature continuous-mode LEDs were produced from a double symmetric as well as nonsymmetric heterostructure based on the solid solutions GaInAsSb. Continuous-wave optical power ~1.7 mW of the LED was achieved by optimizing the structure. © *1997 American Institute of Physics.* [S1063-7850(97)01809-0]

The spectral range 2.0–2.8 μm is distinguished by the fact that it is attractive for producing portable gas analyzers based on spectroscopy methods. The most important such analyzers are used for the analysis nitrogen-containing molecules, such as N_2O (2.11 μm, 2.26 μm), NO_2 (2.19 μm), ammonia NH_3 (2.25 μm), and so on, whose absorption lines lie in the region 2.0–2.28 μm.[1] The radiation sources in such analyzers can be semiconductor LEDs, whose spectral power density and quantum efficiency are higher than those of thermal radiation sources. Infrared LEDs make it possible to produce compact analyzers which are distinguished by the fact that they do not have additional optical filters and mechanical modulators.

Since the emission range of LED heterostructures based on strained layers of the compounds InGaAs/InP[2] is limited to wavelengths shorter than 2 μm, the most promising material for LEDs in the spectral region 2.0–2.28 μm are the solid solutions GaInAsSb/GaSb.[3] GaSb/GaInAsSb/GaAlAsSb heterostructures have already enabled us to achieve a quantum efficiency of radiative recombination up to 4% at room temperature.[4] This spectral range was also covered by radiation from a tunable LED,[5] but the radiation power achieved was less than 0.1–0.2 mW. The investigation reported below is an application of our works in the field of infrared semiconductor emitting heterostructures based on GaSb.

In the present work we made a comparative investigation of different constructions of LEDs for the wavelength range near 2.2 μm that differ both by the magnitude of the electronic confinement and the thickness of the active region. This made it possible to produce LEDs operating at room temperature in the continuous-wave mode with a high optical spectral power density.

Two types of double heterostructures were produced by liquid-phase epitaxy (LPE) on a *n*-GaSb (100) substrate (Fig. 1). The heterostructure of the first type (*S*) consisted of a symmetric GaAlAsSb/GaInAsSb/GaAlAsSb heterostructure. The structure consisted of four epitaxial layers. The active *n*-GaInAsSb layer was confined between two wide-gap emitters *N*- and *P*-GaAlAsSb (2.5 μm thick). The narrow-gap heavily doped *p*-GaSb layer (0.5 μm thick) was grown on top in order to produce a low-resistance contact. The active GaInAsSb layer was characterized by an indium content of 0.16 ($E_g=0.57$ eV) and was doped with Te to density $(1-2)\times10^{17}$ cm^{-3}. The wide-gap GaAlAsSb confining layers were grown with an Al content of 0.50 ($E_g=1.11$ eV) and doped with Te and Ge to density $(2-4)\times10^{18}$ cm^{-3} and $(6-8)\times10^{18}$ cm^{-3} for the *N* and *P* layers, respectively. All layers were lattice matched to the GaSb substrate. The structure of the second type (*NS*) was distinguished by the fact that it did not contain a *N*-GaAlAsSb layer and was a nonsymmetric double heterostructure. The technology of epitaxy of heterostructures based on multicomponent GaSb solid solutions was reported earlier in Ref. 6.

Circular mesa diodes obtained by photolithography and deep chemical etching into the substrate were investigated. The diameter of a mesa (300 μm) determined the emitting surface area ($S=7\times10^{-4}$ cm^2). A crystal of one LED was a 500×500 μm square. The semiconductor crystal was mounted on a standard TO-18 case. A parabolic reflector was mounted on the TO-18 case. This made it possible to collimate the LED radiation into an angle of 10–12 deg. The total dimensions of the LED with the parabolic reflector were 9 mm in diameter and 5.5 mm in length.

The investigations were performed on an apparatus arranged in a synchronous detection scheme based on a MDR-2 monochromator and a GaInAsSb photodiode. The output radiation was collected in an IMO-2M optical power meter.

The current–voltage characteristics of the LEDs exhibited a diode character. The current–voltage characteristics of the two types of structures differed from one another by the cutoff voltage, equal to 0.23 V for the *NS* structure and 0.27 V for the *S* structure. For both structures with forward bias the series resistances were equal to ~1.3–1.4 Ω and the current–voltage characteristics had two sections with an inflection point near 35 mA (the voltage $U\sim0.33-0.35$ V). For low biases the current–voltage characteristic could be described by the formula $I=I_0\exp(eU/kT)$, where e is the electron charge, T is the temperature, and I_0 is the saturation current, which was equal to 1.1 and 0.28 μA for the *S* and *NS* structures, respectively, for the first section and 22 and 4.5 μA for the second section.

The spectral and power characteristics of the diodes were tested in the continuous-wave mode at room temperature. For both structures the spontaneous emission spectrum had the temperature-broadened contour typical for infrared LEDs. Emission was observed under forward bias when the

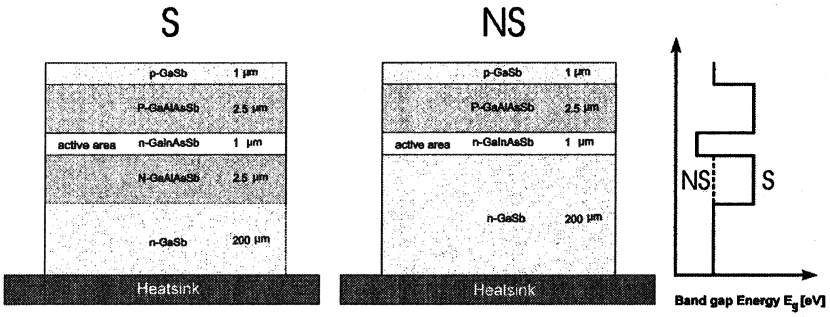

FIG. 1. Diagram of the experimental LED double heterostructures. Radiation was extracted perpendicular to the substrate through the wide-gap layers. The type *S* heterostructure differed from the *NS* type structure by the absence of a wide-gap *N*-GaAlAsSb region. A planar energy diagram of the heterostructures is displayed on the right side; the dotted line shows how they differ.

current amplitude exceeded 5 mA. A rapid increase in power was observed for injection currents above 10 mA. We note only the following observed features of the spontaneous recombination spectra.

The spectrum of the symmetric structure *S* consisted of a single emission band with a maximum at the wavelength $\lambda = 2.173$ μm with a current of 120 mA; the width of the spectrum (FWHM) was equal to 0.23 μm. On cooling to liquid-nitrogen temperature ($T = 77$ K) the maximum shifted in the short-wavelength direction to $\lambda = 1.989$ μm with an average rate of 0.82 nm/K. The FWHM of the spectrum decreased to 0.07 μm. It should be noted that the total temperature shift $\Delta h\nu(\Delta T)$ (0.53 meV) of the maximum was 17 meV less than the computed temperature broadening of the band gap $\Delta E_g(\Delta T)$ (70 meV).

The emission spectrum of the nonsymmetric structure *NS* had the following differences. At a current of 120 mA the maximum was shifted by 20 nm in the long-wavelength direction. The FWHM increased to 0.28 μm. The shift of the maximum to liquid-nitrogen temperature by -0.196 μm also was less than the computed temperature dependence of E_g (by 14 meV). The emission spectrum was characterized by a large increase of the FWHM (0.105 μm) at liquid nitrogen temperature as well. For both structures the position of the emission maximum was virtually independent of the injected current. A shift in the long-wavelength direction at an average rate of 0.05 nm/mA was observed.

The current dependence of the output optical power is displayed in Fig. 2. The optical power *P* increased in the entire current range for both heterostructures and can be described by a power law function $P \sim I^n$. For the symmetric structure *S*, on the initial section $P \sim I$ up to currents $I = 90$ mA and saturated to $P \sim I^{0.87}$ for large pump values. For the nonsymmetric structure *NS* the corresponding values of *n* were of the order of 0.93 and 0.76 for low and high currents, respectively. The dependence was characterized by a higher output power in the entire current range for type-*S* LEDs. The maximum continuous power of 1.7 mW was achieved with an injection current of 120 mA. For high continuous currents the current-voltage characteristic saturated. The symmetric LED heterostructures *S* were investigated as a function of the thickness of the active region from 0.5 to 1.6 μm (Fig. 2b). The maximum optical power was reached with an active region of the order of 0.7 μm thick. Increasing and decreasing the thickness resulted in lower output power. We note that the optimal thickness was significantly less than the carrier diffusion length (~ 2 μm) in GaInAsSb solid solutions.

The characteristics presented show the dependence of the spectral and power characteristics of the LED double heterostructures based on the narrow-gap compounds GaInAsSb on the *N* emitter. The lower value of the slope of

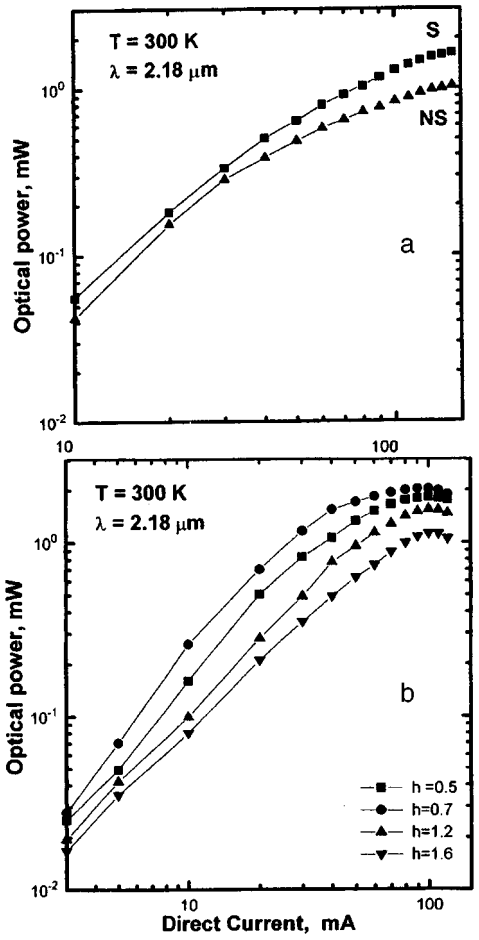

FIG. 2. Power characteristics of LEDs. The curves were obtained with a dc current and room temperature. a — Comparison of the characteristics of LEDs based on symmetric (*S*) (V22712) and nonsymmetric (*NS*) (V22707) double heterostructures, differing by the value of N/n of the heterobarrier. In both structures the active region was 0.8 μm thick. *N*-GaAlAsSb (50% Al) serves as the emitter for the symmetric (*S*) structure and *N*-GaSb (0% Al) serves as the emitter for the nonsymmetric (*NS*) structure. b — Optimization of the output optical power as a function of the thickness of the active region.

the power dependence ($n<1$) indicates the presence of nonradiative losses due to both carrier leakage through the heterobarrier and the existence of a mechanism competing with recombination in the volume of the active region. Specifically, this is due to the leakage of charge carriers through the heterobarrier; this leakage is especially large for holes in a *NS* type structure. The weak temperature dependence of the energy of the maximum of the radiative recombination is characteristic for tunneling radiative recombination. Its presence together with recombination in the volume of the active region could result in a broadening of the emission spectrum, as is observed in a nonsymmetric structure, since a decrease in the height of the *N* emitter results in an increase of the recombination time as $\tau\sim(\Delta E_c)^{-1/2}$.[3] Increasing the voltage applied to this structure rectifies the band bending at the $N-n$ junction and is responsible for the change in the slope for the nonsymmetric structure *NS* at low currents. The change from a linear current dependence ($n\sim1$) to a sublinear dependence ($n<1$) could be due to activation of nonradiative recombination. It should be noted, however, that its coefficient is less than the coefficient corresponding to Auger recombination in the bulk ($n\sim2/3$), indicating a weakening of this channel for nonradiative losses in the experimental symmetric structures. We note that on the whole the spectral and electric characteristics of such structures correspond to recombination in the active region next to the heteroboundary. However, according to the spectral and power differences, the symmetric semiconductor heterostructure GaAlAsSb/GaInAsSb/GaAlAsSb, characterized by the presence of large conduction band offsets comparable in magnitude to the band gap in the active region, is most attractive for achieving maximum spectral power density. This parameter turned out to be exceptionally important for practical applications of infrared LEDs of this class in spectroscopy.

In summary, we report in this Letter the development of 2.0–2.28 μm LEDs for the detection of nitrogen-containing molecules. Our investigations showed the advantages of a symmetric-type LED heterostructure, which was characterized by a higher optical power and smaller width of the emission spectrum in the entire range of continuous pump currents. The basic room-temperature electric and radiative characteristics of the LEDs in the wavelength range 2.2 μm on the basis of dual applications to nitrogen-containing molecules were presented.

[1] L. S. Rothman, R. R. Gamache, R. H. Tipping, C. P. Rinsland, M. A. H. Smith, D. Chris Benner, V. Malathy Devi, J.-M. Flaud, C. Camy-Peyret, A. Goldman, S. T. Massie, L. R. Brown, and R. A. Toth, J. Quant. Spectrosc. Radiat. Transfer **48**, 469 (1992).

[2] M. R. Murti, B. Grietens, C. Van Hoof, and G. J. Borghs, J. Appl. Phys. **78**, 58 (1995).

[3] A. A. Andaspaeva, A. N. Baranov, A. A. Guseinov, A. N. Imenkov, N. M. Kolchanova, and Yu. P. Yakovlev, Semiconductors **24**, 1708 (1990).

[4] A. A. Andaspaeva, A. N. Baranov, A. A. Guseinov, A. N. Imenkov, A. M. Litvak, G. M. Filaretova, and Yu. P. Yakovlev, Sov. Tech. Phys. Lett. **14**, 845 (1988).

[5] A. Popov, Tech. Phys. Lett. **20**, 845 (1994).

[6] A. M. Grabenyuk, A. M. Litvak, A. A. Popov, S. V. Syavris, and N. A. Charykov, J. Appl. Chem. (GB) **64**(12), Part 1, 2421 (1991).

Translated by M. E. Alferieff

Effect of C_{60} on the thermal stability of polyethylene glycol grafted to it

L. A. Shibaev, T. A. Antonova, L. V. Vinogradova, B. M. Ginzburg, V. N. Zgonnik, and E. Yu. Melenevskaya

Institute of High-Molecular Compounds, Russian Academy of Sciences, St. Petersburg; Institute of Problems of Machine Engineering, Russian Academy of Sciences, St. Petersburg
(Submitted April 22, 1997)
Pis'ma Zh. Tekh. Fiz. **23**, 19–24 (September 26, 1997)

The thermal degradation of regular polymer networks, cross-linked by C_{60} molecules along the end groups of polyethylene glycol, has been investigated by mass-spectrometric thermal analysis for the example of polyethylene glycol grafted to fullerene C_{60}. The character of the thermal degradation of the networks is substantially different from that of free polyethylene glycol and other polymer systems investigated earlier. The grafting to C_{60} increases the thermal stability of polyethylene glycol. © *1997 American Institute of Physics.* [S1063-7850(97)01909-5]

The present work is an elaboration of the investigations in Refs. 1–4 of the effect of C_{60} fullerene on the thermal stability of different types of polymer compounds. In Ref. 1 it was shown for the example of the atactic polystyrene by mass-spectrometry that grafting polystyrene to C_{60} fullerene greatly decreases (by more than 100°) the thermal stability of polystyrene. In the same work it was found that even in the case of a mixture of polystyrene with C_{60} the thermal stability of the polystyrene decreases. However, in the case of a mixture of C_{60} with polymethyl methacrylate synthesized by free-radical polymerization the presence of C_{60} increases the thermal stability of the polymer.[3] An increase in thermal stability was also observed for poly-*N*-vinylpyrrolidone cross-linked into an irregular network via carbonyl groups by C_{60} molecules.[4] It is remarkable that in the cases investigated an increase in thermal stability was observed not only in the displacement of the main thermal-degradation process in the direction of high temperatures but also in the inhibition of other thermal-degradation processes (occurring at lower temperatures) right up to their complete suppression.

In the present work the regular polymer networks based on low-molecular polyethylene glycols cross-linked along the end groups of C_{60} molecules have been investigated for the first time by mass-spectrometric thermal analysis.[5]

C_{60} fullerene was obtained by the same method as in Refs. 1–4. Fluka A.C. polyethylene glycol with molecular mass $MM=950-1050$ was used for grafting to C_{60}. The polyethylene glycol was dissolved in toluene and activated by boiling the solvent in argon, using an excess of potassium equal to three times the amount of the OH groups. The activated polyethylene glycol was used for reaction with C_{60}. Since each polyethylene glycol molecule possesses two OH end groups, the formation of macromolecules with C_{60} on both ends as well as on one end was possible as a result of the reaction. Furthermore, taking into consideration the capability of C_{60} to graft several polyethylene glycol molecules, the formation of a cross-linked structure with C_{60} molecules occupying the nodes was possible. This situation was apparently realized in practice, since together with the soluble fraction, consisting of C_{60} molecules with one grafted polyethylene glycol molecule, an insoluble fraction was also obtained. This latter fraction was the object of study in the present work.

The mass spectra were obtained with a MKh-1320 mass spectrometer, heating the sample in vacuum ($10^{-2}-10^{-3}$ Pa) at a rate of 5°/min. Figure 1 displays the mass thermogram of Fluka polyethylene glycol. On account of the low molecular mass of polyethylene glycol, the curves of the yield of the products of thermal degradation have an unusual form (a peak which is not always distinct and the absence of a decreasing part of the curve). This is due to the relatively high volatility of the polymer, which is destroyed only partially, while a substantial part of the polymer shifts along the degrader in the region of lower temperature and is once again partially degraded when the temperature rises to the required values, and so on. The validity of the explanation of the observed form of the thermograms is confirmed by experiments with polyethylene glycol with a higher molecular weight — in this case the thermograms have the standard form (Fig. 2).

Despite the unusual nature of the thermograms of the low-molecular polyethylene glycol, conclusions can be drawn about the main products of its degradation— they are fragments with mass 45 ($^{\bullet}CH_2-CH_2-OH$ or $CH_3-CH_2O^{\bullet}$), 44 ($^{\bullet}CH_2-CH_2-O^{\bullet}$), 89 ($^{\bullet}CH_2-CH_2-O-CH_2-CH_2-OH$ or $CH_3-CH_2-O-CH_2-CH_2-O^{\bullet}$), 117 ($CH_3-CH_2-O-CH_2-CH_2-O-CH_2-CH_2^{\bullet}$). The onset of the thermal degradation of the Fluka polyethylene glycol should evidently be taken at $T_0=300$ °C, and the temperature of peak thermal degradation should be taken as $T_{max}=360$ °C.

The mass-thermogram of fullerene-containing polyethylene oxide[1)] (Fig. 3) differs substantially from the mass-thermogram of polyethylene glycol. Two groups of ion peaks are observed. The lower-temperature peaks with $T_{max}=360$ °C are observed for ions with mass 45, 44, and 43. However, the most intense peak corresponds to the ion with mass 104 ($^{\bullet}O-CH_2-CH_2-O-CH_2-CH_2-O^{\bullet}$), which is not characteristic for the mass thermograms of polyethylene glycol. For it we have $T_0\approx 320$ °C and $T_{max}\approx 440$ °C, which are 20 and 80 degrees higher than the corresponding characteristics of polyethylene glycol. Besides the ion with mass

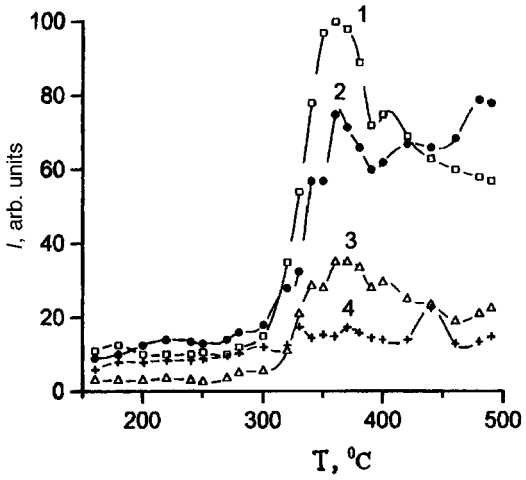

FIG. 1. Mass-thermogram of the initial polyethylene glycol with molecular mass ~1000. *1* — $m/e=45$; *2* — 44; *3* — 89; *4* — 117.

104, ions with mass 91, 117, and 118 but with a much lower yield are present in the same temperature intervals.

The result obtained can be explained only by the fact that on account of the reaction of fullerene and polyethylene glycol a product forming a covalent bond with fullerene was formed. It is known that the thermal stability of polyethylene glycol increases substantially if esterification of the hydroxyl end groups is performed,[6] i.e. thermal degradation of polyethylene glycol starts with the hydroxyl end groups. Apparently, the main part of the product analyzed consists of polyethylene glycol, a molecule of which is attached on both sides to fullerene molecules. This is supported by not only the higher thermal stability of the fullerene-containing polyethylene oxide but also the composition of the products of thermal degradation.

If the polyethylene glycol is degraded from the ends, then it is understandable why the ion with mass 45 (CH_2-CH_2-OH), containing a hydroxyl group, is most intense when the polymer undergoes degradation. In the case of fullerene-containing polyethylene oxide, at high temperatures the intensity of this ion is negligibly small compared

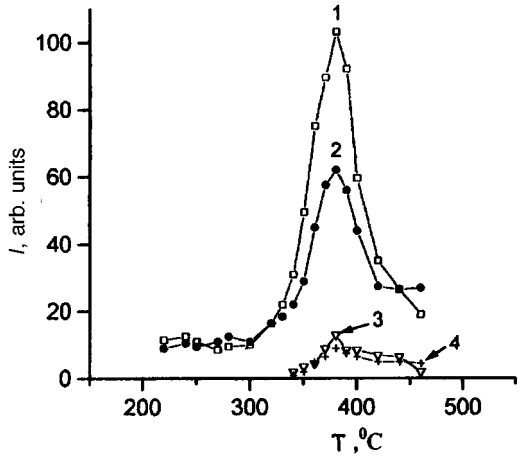

FIG. 2. Mass-thermogram of polyethylene glycol with molecular mass ~20000. *1* — $m/e=45$; *2* — 44; *3* — 89; *4* — 117.

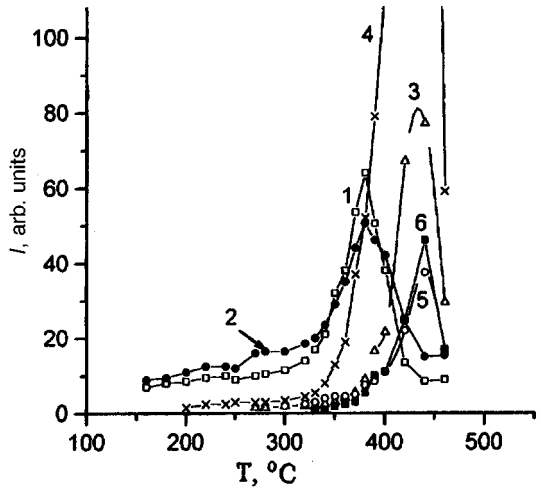

FIG. 3. Mass-thermogram of a network consisting of polyethylene oxide macromolecules cross-linked by C_{60} fullerene molecules. *1* — $m/e=45$; *2* — 44; *3* — 91; *4* — 104 (in the scale presented the maximum of the peak reaches 423 arbitrary units); *5* — 117; *6* — 118.

with the ion 104, and its probable structure ($^{\bullet}O-CH_2-CH_2-O-CH_2-CH_2-O^{\bullet}$) confirms the absence of hydroxyl groups in the initial product.

The low-temperature peaks at ~380 °C (curves *1* and *2*) corresponding to ions with masses 45 and 44 can be explained by the presence of a product of interaction of polyethylene glycol with one fullerene molecule. In this case the degradation starts from the hydroxyl part of the molecule and proceeds in the same manner as the degradation of the initial polyethylene glycol (compare with Fig. 2 and the position of the main peaks in Fig. 1). However, the peaks do not ''creep,'' as happens with low-molecular polyethylene glycol (Fig. 1), since the second end of the polyethylene glycol molecules is apparently bound with fullerene.

This work was performed as part of the Russian Scientific–Technological Program ''Fullerenes and atomic clusters'' (Project Tribol).

[1)] In polymer chemistry, polyethylene glycols that lose hydroxyl end groups are called polyethylene oxides.

[1] B. M. Ginzburg, A. O. Posdnyakov, V. N. Zgonnik, O. F. Posdnyakov, B. P. Redkov, E. Yu. Melenevskaya, and L. V. Vinogradova, Pis'ma Zh. Tekh. Fiz. **22**(4), 73 (1996) [Tech. Phys. Lett. **22**, 166 (1996)].
[2] A. O. Posdnyakov, O. F. Posdnyakov, B. P. Redkov, V. N. Zgonnik, E. Yu. Melenevskaya, L. V. Vinogradova, and B. M. Ginzburg, Pis'ma Zh. Tekh. Fiz. **22**(18), 57 (1996) [Tech. Phys. Lett. **22**, 759 (1996)].
[3] L. A. Shibaev, T. A. Antonova, L. V. Vinogradova, B. M. Ginzburg, V. N. Zgonnik, and E. Yu. Melenevskaya, Pis'ma Zh. Tekh. Fiz. **23**(18), 81 (1997) [Tech. Phys. Lett. **23**, 730 (1997)].
[4] L. A. Shibaev, T. A. Antonova, L. V. Vinogradova, B. M. Ginzburg, V. N. Zgonnik, and E. Yu. Melenevskaya, Pis'ma Zh. Tekh. Fiz. **23**(18), 87 (1997) [Tech. Phys. Lett. **23**, 732 (1997)].
[5] L. A. Shibaev, T. A. Antonova, L. A. Fedorova, S. I. Klenin, I. A. Baranovskaya, and B. L. Erusalimskiĭ, Vysokomolek. Soed., Ser. A **37**, 1874 (1995).
[6] J. Mito, in *Aspects of Degradation and Stabilization of Polymers*, Edited by H. H. G. Jellinek, Elsevier Sci. Pub. Co., N. Y., 1978, pp. 247–294.

Translated by M. E. Alferieff

Interaction of relaxational waves with waves of a redistributing surfactant on a free surface of a liquid

D. F. Belonozhko, A. I. Grigor'ev, and Yu. D. Rakhmanova

Yaroslav State University
(Submitted April 21, 1997)
Pis'ma Zh. Tekh. Fiz. **23**, 25–31 (September 26, 1997)

Thermal capillary wave motion on a charged free surface of a liquid covered with a surfactant film gives rise to waves of redistributing charge (equalizing the electrical potential) and waves of the surfactant (equalizing the concentration of the surfactant). Numerical analysis of the dispersion equation shows that in some range of physical parameters the waves of charge interact with the waves of surfactant, forming two new branches of charge-concentration waves.
 [S1063-7850(97)02009-0]

We shall consider the problem of calculating the spectrum of capillary oscillations on the surface of a solution of a surfactant in a liquid with finite conductivity. The entire system is located in the field of gravity $\mathbf{g}$ and in an electrostatic field $\mathbf{E}_2$ which is normal to the free surface and is determined by the potential difference V between electrodes — the free surface of the conducting liquid and a flat counter electrode on top, parallel to the surface of the liquid and separated from it by a distance d. The solution has density ρ, kinematic viscosity ν, specific conductivity σ, and permittivity $\varepsilon_1=\varepsilon$; the mobility of the charge on the free surface is b. Let C_0 and Γ_0 be the volume and surface concentrations of the surfactant in the unperturbed state, γ the surface tension of the solution, and μ_n and μ_p the chemical potentials of the volume and surface phases of the surfactant. Let us assume that the relaxation time of the surfactant between the surface and the region of the bulk solution lying next to the surface is small compared with the period of the thermal capillary waves at the wavelength analyzed.

In a Cartesian coordinate system with the z axis directed vertically upwards, $\mathbf{n}_z \| \mathbf{g}$ ($\mathbf{n}_z$ is a unit vector directed along the Cartesian coordinate z), the plane $z=0$ is the unperturbed free surface of the solution and the function $\xi(x,t)=\xi_0\exp(st+ikx)$ describes a small perturbation of this surface caused by thermal capillary wave motion of very small amplitude ($\xi_0 \sim (kT/\gamma)^{1/2}$); k is Boltzmann's constant; T is the absolute temperature; s is the complex frequency; k is the wave number; and, t is the time. The liquid velocity field $\mathbf{U}(\mathbf{r},t)$ generated by the perturbation ξ is an infinitesimal of the same order of magnitude. Let the permittivity of the medium above the solution be $\varepsilon_2=1$.

To analyze the spectrum of capillary motions in the system described above, we can use the linearized system of equations

$$\frac{\partial \mathbf{U}}{\partial t} = -\nabla P(\mathbf{U}) + \nu \Delta \mathbf{U} + \mathbf{g}; \tag{1}$$

$$\nabla \cdot \mathbf{U} = 0; \tag{2}$$

$$\Delta \Phi_i = 0; \quad \mathbf{E}_i = -\nabla \Phi_i; \quad (i=1;\ 2); \tag{3}$$

$$\frac{\partial C}{\partial t} = D\left(\frac{\partial^2 C}{\partial x^2} + \frac{\partial^2 C}{\partial z^2}\right); \tag{4}$$

with the boundary conditions

$$z=d: \quad \Phi_2 = V; \tag{5}$$

$$z \to -\infty: \quad \mathbf{U} \to 0; \tag{6}$$

$$C \to C_0; \tag{7}$$

$$\Phi_1 \to 0. \tag{8}$$

Here $P=P(\mathbf{r},t)$ is the pressure inside the liquid; $C=C(\mathbf{r},t)$ is the volume concentration of the surfactant in solution; and, Φ_2 and Φ_1 are the electrical potentials above and below the perturbed surface.

At the interface, described by the equation $z=\xi_0\exp(st-ikx)$, of the media the boundary conditions are

$$\frac{\partial \varkappa}{\partial t} - \mathbf{n}\cdot\mathbf{E}_1\sigma + \nabla_s \cdot (\varkappa \mathbf{U}_\tau + \varkappa \mathbf{E}_\tau d - D_s \nabla \cdot \varkappa) = 0; \tag{9}$$

$$\frac{\partial \Gamma}{\partial t} + \nabla_s(\Gamma \cdot \mathbf{U}_\tau) = D\left(\frac{\partial C}{\partial z}\right) + D_\tau\left(\frac{\partial^2 \Gamma}{\partial x^2}\right); \tag{10}$$

$$\nabla_s \equiv \frac{\partial}{\partial x} + \frac{\partial}{\partial y};$$

$$\mu_n(C) = \mu_p(\Gamma); \tag{11}$$

$$4\pi\varkappa = (\mathbf{n}\cdot\mathbf{E}_2) - \varepsilon(\mathbf{n}\cdot\mathbf{E}_1); \tag{12}$$

$$\Phi_1 = \Phi_2; \tag{13}$$

$$-\frac{\partial \xi(x,t)}{\partial t} + U_z = 0; \tag{14}$$

$$-P(\mathbf{U}) + \xi + 2\nu\mathbf{n}\cdot(\mathbf{n}\cdot\nabla)\mathbf{U} - P_E(\xi) + P_\gamma(\xi) = 0; \tag{15}$$

$$\nu(\mathbf{n}\cdot(\boldsymbol{\tau}\cdot\nabla)\mathbf{U} + \boldsymbol{\tau}\cdot(\mathbf{n}\cdot\nabla)\mathbf{U}) + P_\tau(\xi) + \Pi_E = 0. \tag{16}$$

In these relations $P_\gamma = -\gamma(\Gamma_0)(\partial^2\xi/\partial x^2)$ is the pressure due to the surface tension under the flat surface, curved by the wave motion, of the surfactant solution; $P_E = P_{E2} - P_{E1}$, where $P_{Ei} = (\varepsilon_i/8\pi)[(\mathbf{n}\cdot\mathbf{E}_i)^2 - (\boldsymbol{\tau}\cdot\mathbf{E}_i)^2]$, $i=1,2$, is the electrostatic pressure on the surface as a result of the presence of a surface charge distributed with density $\varkappa$; $\Pi_\varkappa = \Pi_{\varkappa 1} - \Pi_{\varkappa 2}$, where $\Pi_{\varkappa i} = (\varepsilon_i/4\pi)(\mathbf{n}\cdot\mathbf{E})(\boldsymbol{\tau}\cdot\mathbf{E}_i)$, $i=1,2$, is the electrical part of the tangential components of the stress tensor; $P_\tau \equiv (\boldsymbol{\tau}\cdot\nabla\gamma)$ is the tangential component of the stress tensor

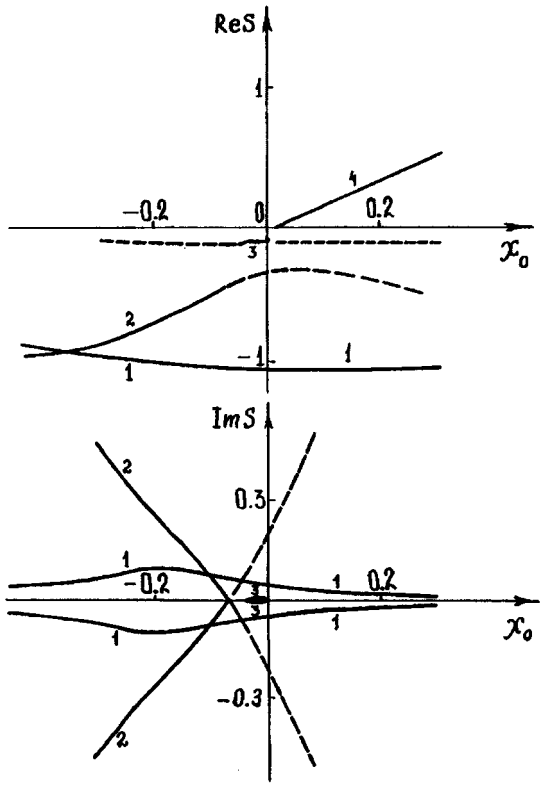

FIG. 1. Curves of the real Re $s=\mathrm{Re}\, s(\chi_0)$ and imaginary Im $s=\mathrm{Im}\, s(\chi_0)$ parts of the complex frequency of capillary motions on the surface of a surfactant solution versus the dimensionless parameter χ_0. The curves were calculated for the following values of the parameters: $k=1$, $\nu=0.1$; $L=500$; $D=1\times10^{-6}$; $D_\tau=1\times10^{-6}$; $D_s=10^{-5}$; $W=2$; and, $\beta=1\times10^{-2}$.

due to the relaxation of the surfactant on the perturbed surface; D_τ and $D_s$are the surface diffusion coefficients for the surfactant and charge, respectively; D is the volume diffusion coefficient of the surfactant; and, $\boldsymbol{\tau}$ and $\mathbf{n}$ are unit vectors tangent and normal to the surface of the solution.

Solving the problem (1)–(16) by the method described in Ref. 1 yields a dispersion equation for capillary motions of the liquid which in the dimensional variables where $g=\rho=\gamma=1$ has the form

$$
\begin{aligned}
&(\beta s^2\Lambda - kH)(s+k^2D_\tau)+\Theta\chi_0 s k^3\omega_0^2\\
&+\beta k^5 W\coth(kd)\chi_0 s(s+k^2D_s)\\
&+q((s+k^2D_\tau)(H-4\Theta\nu^2k^3s^2-\beta k^4W\coth(kd)\chi_0 s)\\
&-\Theta\chi_0 s k^2(\omega_0^2+s^2))\\
&+RL(s^2\Lambda-kH)+qRL(H-4\Theta\nu^2k^3s^2)=0; \qquad (17)\\
&\Theta\equiv\beta(s+k^2D_s)(1+\varepsilon\tanh(kd))\\
&\quad+(1+\beta E_0 kb)\tanh(kd);\\
&\Lambda\equiv\Theta((s+2\nu k^2)^2+\omega_0^2)+\beta k^2 W\coth(kd)\\
&\quad\times(s(1-\tanh(kd))+k^2D_s)(1-\tanh(kd));\\
&H\equiv\beta s k W((\omega_0^2+s^2)\tanh(kd)\\
&\quad+2\nu k^2(2s+k^2D_s))\tanh^2(kd);\\
&\chi_0=\frac{\partial\gamma}{\partial\Gamma}\Gamma_0;\quad L=\left(\frac{\partial\mu_n}{\partial\Gamma_0}\right)\Big/\left(\frac{\partial\mu_p}{\partial C_0}\right);\\
&W=\frac{\varepsilon E_0^2}{4\pi};\quad E_0=V/d;\quad \beta\equiv\frac{1}{4\pi\sigma};
\end{aligned}
$$

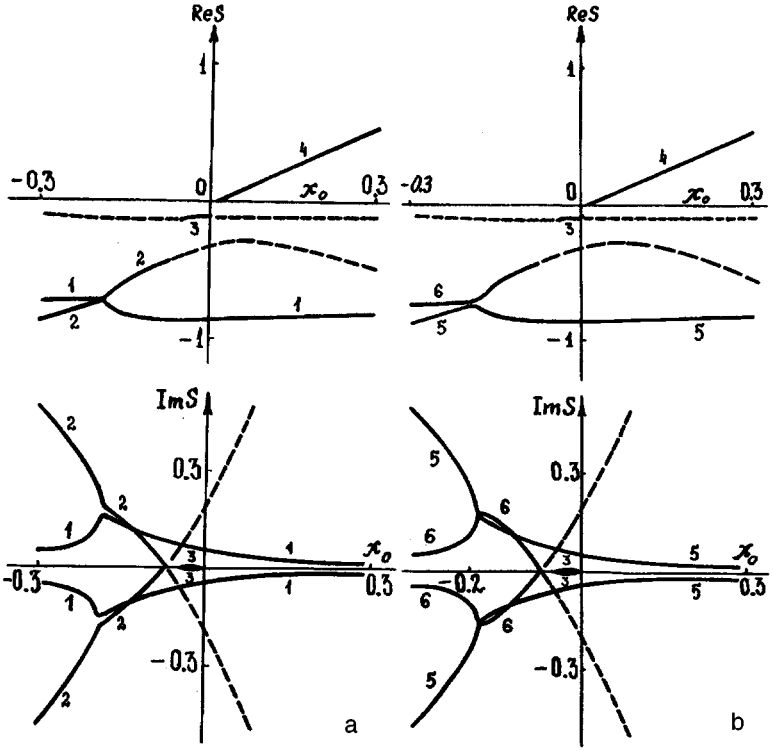

FIG. 2. Curves of the real Re $s=\mathrm{Re}\, s(\chi_0)$ and imaginary Im $s=\mathrm{Im}\, s(\chi_0)$ parts of the complex frequency of capillary motions on the surface of a surfactant solution versus the dimensionless parameter χ_0. The curves were calculated for the following values of the parameters: $k=1$, $\nu=0.1$; $L=500$; $D=10^{-6}$; $D_\tau=1\times10^{-6}$; $D_s=10^{-5}$; $W=2$; a — $\beta=1.2\times10^{-2}$; b — $\beta=1.21\times10^{-2}$.

$$\omega_0^2 \equiv k^3 + k - Wk^2 \coth(kd); \quad q \equiv \sqrt{k^2 + s/\nu};$$

$$R \equiv \sqrt{D(s + k^2 D)}$$

with characteristic scales of the dimensional quantities

$$s_* = \left(\frac{\rho g^3}{\gamma}\right)^{1/4}; \quad k_* = \left(\frac{\rho g}{\gamma}\right)^{1/2};$$

$$D_{\tau *} = D_{s*} = D_* = \left(\frac{\gamma^3}{\rho^3 g}\right)^{1/4};$$

$$\nu_* = \frac{\gamma}{\rho g^3}; \quad \beta_* = \left(\frac{\gamma}{\rho g^3}\right)^{1/4}; \quad W_* = \sqrt{\rho g \gamma}; \quad d_* = \left(\frac{\gamma}{\rho g}\right)^{1/2}.$$

The region $\chi_0 < 0$ corresponds to ordinary surfactants, which decrease the surface tension γ of the free surface of the liquid and the region $\chi_0 > 0$ corresponds to inactive surfactants which increase γ.

The results of a numerical analysis of Eq. (17) are presented in Figs. 1 and 2 in the form of curves of the real and imaginary parts of the complex frequency s as a function of χ_0 with the critical value of the Tonks–Frenkel' parameter $W = 2$, which makes it possible to regard as relaxational all branches of the wave motions observed on the first sheet of a four-sheet Riemann surface on which the dispersion equation (17) is defined. It follows from Fig. 1 that when the conductivity of the solution is high the branch 1 of the relaxational waves associated with charge redistribution[2] does not interact with the branch *2* of waves associated with the redistribution of the surfactants[1,3]. For $\beta \approx 1.2 \times 10^{-2}$ and $\chi_0 \approx 0.19$ reconnection of these branches on one another occurs and two new branches *5* and *6* of composite waves form. The branch *2* reconnects with the branch of charge relaxation waves and extends continuously into the inactive-surfactant region. The branch *1* switches to the part of branch *2* that extends to the unobservable sheets of the Riemann surface even for values $\chi_0 < 0$ which are small in absolute magnitude and is found to be unobservable for inactive ($\chi_0 > 0$) surfactants.

Besides the motions mentioned above, in all relations presented above, for $\chi_0 < 0$ the first sheet of the Riemann surface contains a branch *3* of wave motions which is due to diffusion of the surfactant from the volume.[1] The branch *4* for $\chi_0 > 0$ determines the growth rate of the instability of the surface with respect to a change in the concentration of the inactive substance: For $\chi_0 < 0$ this branch leaves the observable first sheet of the Riemann surface.

In summary, in some range of values of the parameter β the waves of relaxing charge interact with the waves of the redistributing surfactant.

[1] V. G. Levich, *Physicochemical Hydrodynamics* [in Russian], Fizmatgiz, Moscow, 1959.
[2] S. O. Shiryaeva, A. I. Grigor'ev, and V. A. Koromyslov, Pis'ma Zh. Tekh. Fiz. **22**(4), 89 (1996) [Tech. Phys. Lett. **22**, 173 (1996)].
[3] D. F. Belonozhko, S. O. Shiryaeva, and A. I. Grigor'ev, Pis'ma Zh. Tekh. Fiz. **22**(15), 60 (1996) [Tech. Phys. Lett. **22**, 626 (1996)].

Translated by M. E. Alferieff

On the applicability of Stoney's formula for calculating the mechanical stresses in thick films and coatings

A. V. Dobrynin

Moscow Institute of Electrical Engineering
(Submitted February 11, 1997)
Pis'ma Zh. Tekh. Fiz. **23**, 32–36 (September 26, 1997)

The most accurate expressions for determining stresses in coatings, for example, in aluminum nitride on molybdenum, are derived. The stress curve has a characteristic shape, and for this reason it is proposed that the entire system be called a ''*z* system.'' It is shown that Stoney's formula is of limited applicability, over- or underestimating the true values of the stresses.
 [S1063-7850(97)02109-5]

Stoney's[1] or Timoshenko's[2] formulas are often used to calculate the stresses in layered structures. Stoney examined the case of negligibly small thicknesses of the layer and Timoshenko studied the case when the thickness of the layer equals the thickness of the substrate. These methods are based on the use of the radius of curvature ρ of a structure which is curved as a result of the difference $\Delta\alpha$ of the thermal expansion coefficients of the film and substrate and the difference Δt between the deposition and room temperature. For simplicity, we shall assume that α for the film is less than α for the substrate, i.e. the structure is convex. Let H_1 be the thickness of the film and H_2 the thickness of the substrate, E_1^* and E_2^* the modified Young's moduli of the layer and substrate, where $E_1^*=E_1/(1-\nu_1)$ and $E_2^*=E_2/(1-\nu_2)$, and ν_1 and ν_2 the Poisson ratios. Then the radius of curvature can be calculated according to the expression[2]

$$\rho=\frac{(H_1+H_2)/2+(E_1^*H_1^3+E_2^*H_2^3)(1/E_1^*H_1+1/E_2^*H_2)/6(H_1+H_2)}{\Delta\alpha\Delta t}. \tag{1}$$

In the isotropic approximation, we shall assume that the stresses along the x axis equal the stresses along the y axis. The starting point for constructing curves of the normal stresses σ_z is the relation

$$\sigma_z=E_i x/\rho, \tag{2}$$

where x is the coordinate with respect to the neutral layer (we place the origin of the coordinates on the neutral layer). If the layered structure were curved only by the action of a constant moment, then the curve would have a simple form (the line *a* in Fig. 1). In the presence of thermal deformation $\Delta\alpha\Delta t$, the curve is discontinuous at the interface (line *b* in Fig. 1). The curve assumes a characteristic form so that in what follows we shall call this system a ''*z* system.'' If $E_2^*\approx E_2^*\approx E$(as, for example, in the system AlN/Mo), then the difference between σ_2 and σ_3 equals $E\Delta\alpha\Delta t$. This quantity is divided into right and left parts in the proportion $\sigma_2/\sigma_3=\beta/(1-\beta)$, i.e.

$$\sigma_2=E\beta\Delta\alpha\Delta t, \tag{3}$$

$$\sigma_3=E(1-\beta)\Delta\alpha\Delta t. \tag{4}$$

The coordinates of the neutral layer in the substrate and layer are

$$H_2^*=-\Delta\alpha\Delta t(1-\beta)\rho, \tag{5}$$

$$H_1^*=\Delta\alpha\Delta t\beta\rho. \tag{6}$$

To find β we use the fact that

$$\int_{z_{\min}}^{z_{\max}}\sigma_z=0, \tag{7}$$

whence

$$\beta=H_2/(H_1+H_2)-(H_2-H_1)/(2\rho\Delta\alpha\Delta t). \tag{8}$$

Then the principal stresses of the z system can be expressed as

$$\sigma_1=E\Delta\alpha\Delta tH_2/(H_1+H_2)-E(H_2+H_1)/2\rho, \tag{9}$$

$$\sigma_2=E\Delta\alpha\Delta tH_2/(H_1+H_2)-E(H_2-H_1)/2\rho, \tag{10}$$

$$\sigma_3=-E\Delta\alpha\Delta tH_1/(H_1+H_2)-E(H_2-H_1)/2\rho, \tag{11}$$

$$\sigma_4=-E\Delta\alpha\Delta tH_1/(H_1+H_2)+E(H_2+H_1)/2\rho. \tag{12}$$

In this case the average stress in the layer can be calculated as

$$\overline{\sigma}=E\Delta\alpha\Delta tH_2/(H_1+H_2)-EH_2/\rho. \tag{13}$$

Let us compare the expressions (9), (10), and (13) presented above with Stoney's formula[1]

$$\sigma_s=E_2H_2^2/6\rho H_1. \tag{14}$$

If

$$m=H_1/H_2 \quad \text{and} \quad n=E_1^*/E_2^*\neq 1, \tag{15}$$

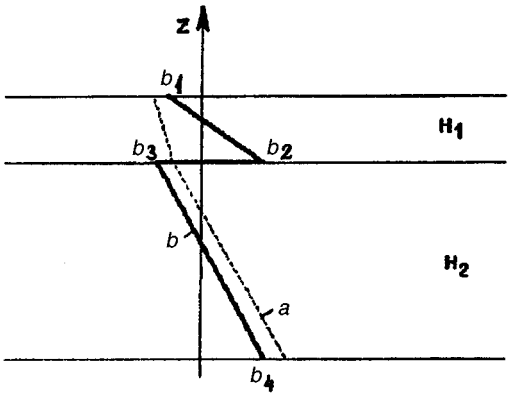

FIG. 1. Curves of the elastic stresses: *a* — in a layered structure subjected to simple bending; *b* — in a nonuniform layered structure subjected to bending (σ_1, σ_2, and σ_3 are the principal stresses forming the *z* system).

then in the *z* system expressions are obtained similarly for σ_1, σ_2, and $\overline{\sigma}$. Substituting the expressions (14) and (15) we obtain the simple expressions

$$\sigma_1=\sigma_s[(nm^3+1)/(m+1)-3nm^2]=K_1\sigma_s, \tag{16}$$

$$\sigma_2=\sigma_s[(nm^3+1)/(m+1)+3nm^2]=K_2\sigma_s, \tag{17}$$

$$\overline{\sigma}=\sigma_s(nm^3+1)/(m+1)=\overline{K}\sigma_s. \tag{18}$$

As an example, we shall examine curves for the structure AlN/Mo, which I investigated experimentally for different ratios of the thicknesses *m*. The stresses in the layer did not change sign for $m<0.5$ and decreased with increasing thickness of this coating. This dependence is due to the decrease in the radius of curvature. The following stresses were found in the structure AlN/Mo ($n=1$; $m=0.8$; $\Delta\alpha\Delta t=1.85\times10^{-3}$): $\sigma_1=-97.2$ MPa, $\sigma_2=248$ MPa, and from Eqs. (14) $\sigma_s=90$ MPa. A coating consisting of polycrystalline aluminum nitride fractured because the rupture strength was exceeded, and according to Stoney's formula it was subjected to a compression far from the critical value. The computed curves of the stresses are displayed in Fig. 2.

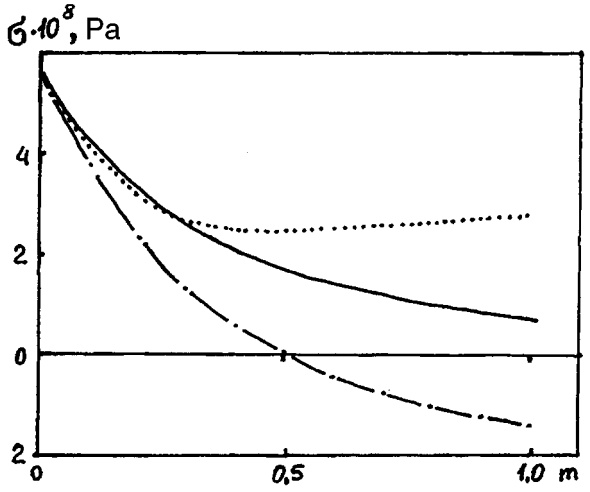

FIG. 2. Stresses in an aluminum nitride coating on a molybdenum base as a function of the ratio of the thicknesses *m* (the simple line corresponds to σ_s, the dashed line corresponds to σ_1, and the dotted line corresponds to σ_2).

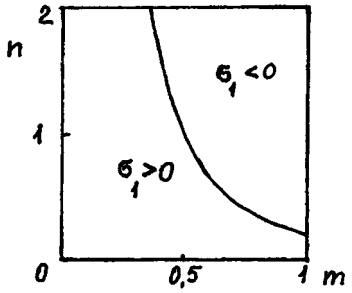

FIG. 3. Region of existence of negative stresses on the surface of a coating with positive stresses in the coating near the interface.

Is it possible to have a case when the substrate is predominantly compressed but the layer is entirely stretched? For $\sigma_2\leqslant0$ we obtain the inequality

$$(1+mn)[m+(1+nm^3)/3nm(1+m)]\leqslant0, \tag{19}$$

which makes no sense, since *n* and *m* are greater than zero. A further analysis of the relations showed that instead of the case when the substrate is predominantly stretched and the layer has different stresses, the bottom part is compressed and the top part is stretched. This requires that $\sigma_1<0$ and $\sigma_2>0$. Therefore, substituting Eqs. (16) and (17) we obtain

$$2n^2m^3+3nm^2-1>0. \tag{20}$$

From the expression (20) it is easy to determine the region of existence of the negative values of σ_1 (Fig. 3). It is evident that thick ($m>0.5$) or stiff ($n>1$) layers can partially stretch. Analysis of these curves shows that it is incorrect to use Stoney's formula for thick coatings, but even for relatively thin layers the expression (15) overestimates the stresses. It is evident that for relatively thin layers ($m\leqslant0.5$) the overestimation is in the range 10–20%. However, Stoney's formula does not reflect at all the true situation in relatively thick layers or coatings, where according to the *z* system a tensile stress acts on the top surface and compressive stresses, many times greater than σ_s, act on the interface in the layer. For example, for $n=2$ and $m=1$ we have $K_1=-4.5$, $K_2=+7.5$, and $\overline{K}=1.5$. The deviations are especially large in the case when the coating material is stiffer than the substrate material ($n>1$), for example, the structures nitrides on silicon, metals on polyamide films, and others.

[1] G. S. Stoney, Proc. Royal Soc. Ser. A **82**, 172 (1990).
[2] S. P. Timoshenko, J. Optical Soc. America and Review Scientific Instruments **11**, 233 (1925).

Translated by M. E. Alferieff

Maximum information capacity of a three-dimensional hologram

Yu. I. Kuz'min

A. F. Ioffe Physicotechnical Institute, Russian Academy of Sciences, St. Petersburg
(Submitted February 5, 1997)
Pis'ma Zh. Tekh. Fiz. **23**, 37–43 (September 26, 1997)

This Letter is devoted to the problem of the maximum information capacity of a three-dimensional hologram with optimal utilization of the dynamic range of the storage medium. A hologram is treated as an object of information theory. Diffraction-limited holographic writing is analyzed on the basis of the reciprocal-lattice formalism. The calculation of the information capacity of the three-dimensional hologram is reduced to analysis of a set of multiplexed holograms each of which possesses a finite signal/noise ratio determined by the dynamic range of the holographic medium. The optimal number of pages which give the maximum information capacity with angular multiplexing is found. © *1997 American Institute of Physics.* [S1063-7850(97)02209-X]

Since the discovery of holography, the question of the information capacity of holograms has been very important for the development of optical information processing and storage systems.[1–5] The present Letter is devoted to an analysis of the maximum information capacity of a three-dimensional hologram with optimal utilization of the dynamic range of the storage medium.

The information capacity is the largest amount of information that can be stored and then retrieved with as small a probability of error as desired. According to the Kotel'nikov–Shannon theorem, the information recorded in a hologram is completely determined by $4A\Delta^2W$ read-outs (pixels), where A is the transverse area of the hologram and Δ^2W is the two-dimensional width of the spectrum of recorded spatial frequencies. The quantity $4\Delta^2W$ is the two-dimensional analog of the Nyquist frequency. The upper limit of the information capacity of both three- and two-dimensional holograms can be found by analogy to the Shannon formula for the throughput capacity of a communication channel in the presence of white noise:[6,7]

$$C_{3D}=4A\Delta^2WN\ \log_2(1+R_{3D}(\Delta^2W,N)),\quad \text{bit}, \tag{1}$$

$$C_{2D}=4A\Delta^2W\ \log_2(1+R_{2D}(\Delta^2W)),\quad \text{bit}, \tag{2}$$

where N is the number of multiplexed holograms (pages), $R\equiv P_s/P_n$ is the signal/noise ratio in reading of a single pixel, P_s is the upper limit of the average power of the signal producing the image, and P_n is the average optical noise power.

Let us determine the maximum number of pixels that can be recorded in the hologram in the presence of only diffraction limitations. We shall take an elementary holographic grating to mean the spatial distribution of the recorded physical parameter, the distribution being invariant relative to translations of the form

$$\mathbf{T}_{3D}=n_1\mathbf{e}_1+\nu_2\mathbf{e}_2+\nu_3\mathbf{e}_3,\quad \forall n_1\in\mathbb{I},\quad \forall \nu_2,\nu_3\in\mathbb{R}, \tag{3}$$

$$\mathbf{T}_{2D}=n_1\mathbf{e}_1+\nu_2\mathbf{e}_2+\nu_0\mathbf{e}_3,\quad \forall n_1\in\mathbb{I},\quad \forall \nu_2\in\mathbb{R}, \tag{4}$$

for three- and two-dimensional holograms, respectively; here $\mathbf{e}_i$ are the basis vectors of the translations, ν_0 is the coordinate of the lattice plane, $\mathbb{I}$ and $\mathbb{R}$ are sets of integer and real numbers. In three-dimensional space the translational vector (3) describes a set of parallel planes $\mathbf{T}_{3D}\in\mathbb{I}\otimes\mathbb{R}^2$ (Fig. 1a), and the vector (4) describes a set of collinear and coplanar lines $\mathbf{T}_{2D}\in\mathbb{I}\otimes\mathbb{R}$(Fig. 1c).

Reciprocal lattices corresponding in k space to the translations (3) and (4) have the form

$$\mathbf{Q}_{3D}=m^1\mathbf{q}^1,\quad \forall m^1\in\mathbb{I}, \tag{5}$$

$$\mathbf{Q}_{2D}=m^1\mathbf{q}^1+\mu^0\mathbf{q}^2+\mu^3\mathbf{q}^3,\quad \forall m^1\in\mathbb{I},\quad \forall \mu^3\in\mathbb{R}, \tag{6}$$

where μ^0 is a coordinate of the plane of the reciprocal lattice, $\mathbf{q}^j$ are the basis vectors of the reciprocal lattice, which satisfy the orthogonality relation $\mathbf{e}_j\cdot\mathbf{q}^j=2\pi\delta_i^j$, where δ_i^j is the Kronecker δ function.

In k-space the reciprocal lattice (5) is a set of equidistant points $\mathbf{Q}_{3D}\in\mathbb{I}$ (Fig. 1b), and the reciprocal lattice (6) is a set of collinear and coplanar lines $\mathbf{Q}_{2D}\in\mathbb{I}\otimes\mathbb{R}$ whose orientation is fixed by the orthogonality relation (Fig. 1d). When reading information from a hologram, the orientation of the restored beam is determined by the points of intersection of the Ewald sphere (whose radius equals the wave vector $\mathbf{k}_0$ of the reading light) and the reciprocal lattice. The scattering vector is identical to the reciprocal lattice vector (5) or (6), as shown in Fig. 1. The independent states in k-space on the Ewald sphere correspond to the diffraction-resolvable Fourier components of the reconstructed image. Thus the largest number of pixels that can be recorded in a hologram of any dimension equals the number of states on (1/2) the surface of the Ewald sphere:

$$\sup(4A\Delta^2W)=\frac{1}{2}\left(\frac{4\pi k_0^2}{\Delta^2k}\right)=8\pi\frac{A}{\lambda^2}, \tag{7}$$

where $\Delta^2k=\pi/A$ is the squared minimum uncertainty of the wave vector in the diffraction limit of resolution and λ is the wavelength of the reading light. Counting the states on half the surface of the Ewald sphere corresponds to summing over the spatial frequencies within the entire Fourier plane. The expression (7) assumes that there is no polarization multiplexing, taking account of which doubles the result.

The maximum number of pages that can be recorded in a three-dimensional hologram with angular multiplexing can

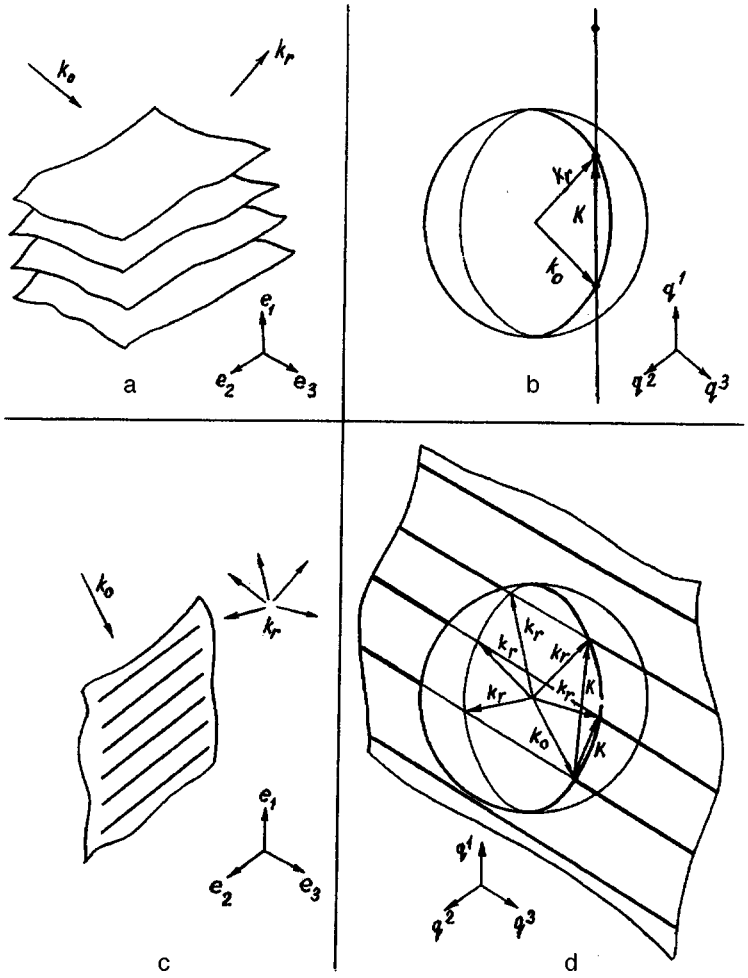

FIG. 1. Translation-invariant sets and reciprocal lattices for optical diffraction by a three-dimensional (a, b) and two-dimensional (c, d) holographic lattices: (a, c) — coordinate space, (b, d) — k-space; $\mathbf{K}$ — scattering vector (shown only for forward scattering), $\mathbf{k}_0$ and $\mathbf{k}_r$ — wave vectors of the reading and reconstructed beams, respectively.

be counted by summing over all reciprocal-lattice vectors based on the Ewald sphere (i.e. over all wave vectors of the recorded holographic gratings): $\max(N)=2k/\Delta k=4L/\lambda$, where $\Delta k=\pi/L$ is the minimum uncertainty of the wave vector and L is the thickness of the hologram. On the basis of the expression (7), it is easy to find the maximum number of pixels that can be recorded in all pages of the three-dimensional hologram with an unlimited dynamic range:

$$\sup(4A\Delta^2W)\max(N)=32\pi AL/\lambda^3. \tag{8}$$

Estimates of the type ''volume''$/\lambda^3$ are often given for the maximum information capacity of a hologram.[1,2,5] But, in so doing an unsubstantiated assumption is often made that the information is stored in the form of volume resolution elements (''voxels''[8]) and the two-dimensionality of the spectrum of spatial frequencies of the recorded information is neglected. The number of multiplexed holograms is determined by the finite dynamic range of the holographic medium, on which the signal/noise ratio depends. For this reason, the estimate (8) is unattainable in practice. In the case of multiplexing, the information capacity does not at all increase by a factor of N, as could appear in a cursory analysis of the formulas (1) and (8) neglecting the dependence $R_{3D}=R_{3D}(N)$.

Let us see how the number of pages influences the information capacity. In the case of a two-dimensional hologram, the entire dynamic range is employed for encoding each pixel with the maximum word length. For a three-dimensional hologram the word lengths can be exchanged for the number of pages within the same dynamic range. An increase in the number of pages is accomplished by decreasing R_{3D} down to the word length of one bit per pixel. We shall show that there exists an optimal number of pages for which the information capacity is maximum. The number of multiplexed holograms can be represented in the form $N=\sqrt{P_s(1)}/\sqrt{P_s(N)}$, where $P_s(1)$ is the maximum power of the signal for writing only one page using the entire dynamic range and $P_s(N)$ is the signal power for writing one of the N multiplexed pages. Now we can relate $R_{3D}(N)$ and $R_{3D}(1)=\max_N R_{3D}(N)$ as

$$R_{3D}(N)\equiv\frac{P_s(N)}{P_n}=\frac{P_s(1)}{N^2P_n}=\frac{P_{3D}(1)}{N^2}.$$

If $R_{3D}(1)\gg N^2$, the expression (1) assumes the form

$$C_{3D}(N)=NC_{3D}(1)-8A\Delta^2WN\log_2 N. \tag{9}$$

This function has a maximum at

$$N_0=2\left(\frac{C_{3D}(1)}{8A\Delta^2W}-\frac{1}{\ln 2}\right).$$

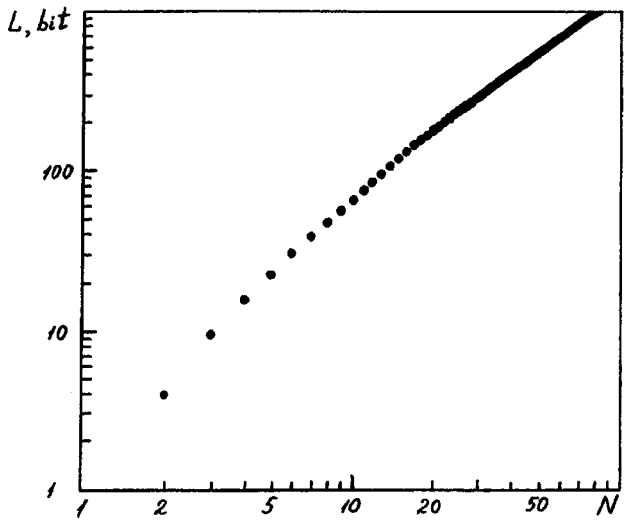

FIG. 2. The function $L(N)$, where N is the number of multiplexed holograms.

Therefore, there exists an optimal number of pages $N_{\text{opt}} = \text{entier}(N_0)$, above which the information capacity will decrease as a result of a decrease in the signal/noise ratio $R_{3D}(N)$.

It is interesting to note that for a sufficiently large value of $R_{3D}(1)$ the information capacity $C_{3D}(N)$ of a three-dimensional hologram containing N pages is less than the information capacity $NC_{3D}(1)$ of N holograms each of which contains only one page, all other conditions being equivalent. As follows from the expression (9), the difference in the information capacity per pixel is described by the function

$$L(N) \equiv \frac{NC_{3D}(1) - C_{3D}(N)}{4A\Delta^2 W} = 2N \log_2 N, \quad \text{bit},$$

displayed in Fig. 2.

In the present Letter a hologram is treated as an object of information theory. The calculation of the information capacity of a three-dimensional hologram has been reduced to analysis of a set of multiplexed holograms, each of which has a finite signal/noise ratio determined by the dynamic range of the recording medium. A solution was obtained for the problem of optimal utilization of the dynamic range with angular multiplexing. The diffraction-limited holographic writing of information was analyzed on the basis of a reciprocal-lattice formalism. This makes it possible to utilize to the maximum possible degree the fundamental property of an optical image — the two-dimensional nature of the spectrum of its spatial frequencies.

I am grateful to Professor M. P. Petrov for a fruitful discussion of the problem of the information capacity of a hologram.

[1] P. J. Van Heerden, Appl. Opt. **2**, 393 (1963).
[2] R. G. Ramberg, RCA Rev. **33**, 5 (1972).
[3] M. P. Petrov, S. I. Stepanov, and A. V. Khomenko, *Photorefractive Crystals in Coherent Optical Systems*, Springer-Verlag, N. Y., 1991.
[4] S. V. Miridonov, A. V. Khomenko, D. Tentori, and A. A. Kamshilin, Opt. Lett. **19**, 502 (1994).
[5] J. Wullert and Y. Lu, Appl. Opt. **33**, 2192 (1994).
[6] C. Shannon, Proc. IRE. **37**, 10 (1949).
[7] P. B. Fellgett and E. H. Linfoot, Phil. Trans. Roy. Soc. A **247**, 369 (1955).
[8] D. Brady and D. Psaltis, J. Opt. Soc. Amer. A **9**, 1167 (1992).

Translated by M. E. Alferieff

Activation energy of electron-stimulated quenching of the photoluminescence of *n*-type porous silicon

B. M. Kostishko, A. M. Orlov, and V. A. Frolov

Ul'yanov State University
(Submitted March 13, 1997)
Pis'ma Zh. Tekh. Fiz. **23**, 44–50 (September 26, 1997)

The degradation of photoluminescence of porous silicon by kilovolt electrons and the mechanism and activation energy of this process have been investigated. Quantitative relations between the integral intensity of the photoluminescence and the irradiation dose and substrate temperature are obtained. The mechanism of the process is discussed and its activation energy is determined. © *1997 American Institute of Physics.* [S1063-7850(97)02309-4]

The discovery of the light emitting properties of porous silicon[1] stimulated great interest in this porous silicon as a promising material for optoelectronics. Attempts to adopt this material in practice have generated an increasing number of works on the influence of different types of actions (thermal,[2] electromagnetic,[3,4] penetrating radiations,[5], and so on) on the properties of porous silicon and, specifically, on its photoluminescence. Thus far, however, many aspects of this problem remain unknown. Specifically, very little data[6,7] exist on the effect of electronic stimulation of the quenching of photoluminescence of porous silicon.

The present work is devoted to an investigation of the degradation of photoluminescence by kilovolt electrons and the determination of the mechanism and activation energy of this process.

Phosphorus-doped silicon wafers with (100) orientation and resistivity $\rho = 2.4\ \Omega \cdot \mathrm{cm}$ ($N_a = 1.5 \times 10^{15}\ \mathrm{cm}^{-3}$) served as the starting material for the samples of porous silicon. The porous silicon was produced by the standard technology by electrochemical etching in an electrolyte consisting of 48% hydrofluoric acid (HF) and ethyl alcohol in a 1:1 ratio. The electrochemical etching time was equal to $t_{\mathrm{etch}} = 40$ min with current density $j = 20\ \mathrm{mA/cm}^2$. For each sample the initial intensity of the photoluminescence and its uniformity over the surface were checked beforehand.

Irradiation by electrons with energy $E_p = 4$ keV was conducted in an ultrahigh-vacuum chamber of an 09IOS10-005 Auger spectrometer with residual pressure 5×10^{-8} Pa in the chamber in an electron beam scanning regime. This made it possible to vary the irradiation dose in the range $D = 10^{15} - 5 \times 10^{17}\ \mathrm{cm}^{-2}$. A series of up to 12 sections with different doses was formed on 1 cm^2 one sample. To investigate the temperature dependence of the degradation rate of the photoluminescence under irradiation with electrons, the holder with the porous-silicon samples was heated directly in the chamber by a wide electron beam directed onto the backside of the holder. The temperature of the irradiated porous silicon was varied in the range 20–125 °C and recorded with a thermocouple. The intensity of the luminescence of the treated sections of the porous silicon was different and depended strongly on the electronic irradiation does and the temperature of the irradiated sample.

The quantitative dependences of the integrated intensity I_L of the photoluminescence on the dose D of electronic irradiation and the substrate temperature T were determined according to the starting values of the intensities with the surface of porous silicon irradiated with a LGN-409 He–Cd laser ($\lambda = 325$ nm, $P = 20\ \mathrm{mW/cm}^2$) and are presented in Fig. 1. As one can see, the integrated intensity of the photoluminescence has the form of an asymptotic exponential — rapid decay for low doses followed by saturation. This character of the electronic stimulation of the quenching of the photoluminescence of porous silicon is especially clearly manifested at high temperatures. For room temperatures, saturation occurs at higher doses.[7]

In accordance with the principles developed in Ref. 7, the degradation of the photoluminescence of porous silicon under the action of kilovolt electrons is due not to the formation of defects in the single-crystal matrix but rather the change in the composition of the atoms passivating the pores and the number of broken bonds. It is assumed that the electrons effectively destroy the $\mathrm{Si–H_2}$ groups on the surface of quantum wires. This in turn increases the density of centers of nonradiative annihilation of excitons and decreases the photoluminescence intensity[8]

$$I_L = A_{\mathrm{ex}} \beta N_L n_{\mathrm{ex}}, \tag{1}$$

where N_L is the density of centers of radiative annihilation of excitons, which corresponds to the density of adsorbed hydrogen N_{H_s}; n_{ex} is the density of excitons; β is the probability of radiative annihilation; and, A_{ex} is a dimensional constant.

It can be conjectured on the basis of the experimental data obtained that the dose dependence of the concentration of $\mathrm{SiH_2}$ groups and, correspondingly, centers of luminescence at a maximum electron penetration depth h comparable to the thickness h_0 of the light-emitting layer can be written in the form

$$N_L(D) = N_0 \exp(-(D/D_0)^{\alpha}), \tag{2}$$

where N_0 is the initial density of light-emitting centers in the sample; D_0 is the characteristic electron dose for which the density of hydrogen-passivated bonds in the porous silicon decreases by a factor of e; and, α is an empirical parameter.

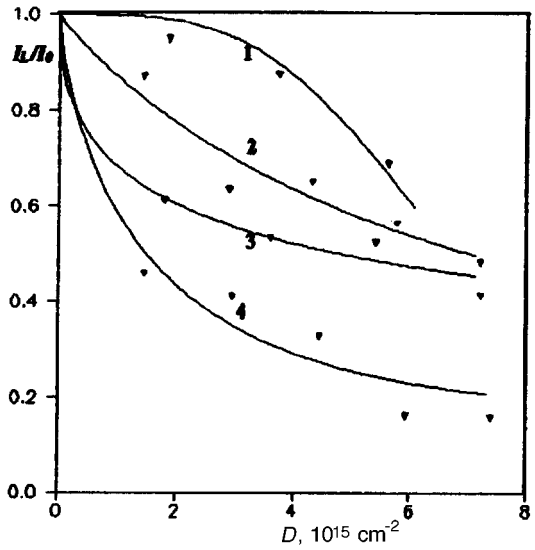

FIG. 1. Normalized integral photoluminescence intensity versus electronic irradiation dose for *n*-type porous silicon. Points — experimental values, lines — computational results obtained with Eq. (3). The curves *1, 2, 3,* and *4* correspond to substrate temperatures of 20, 40, 90, and 125 °C, respectively.

The ratio of the intensities of the photoluminescence of the section irradiated by electrons to a dose D and not irradiated by electrons is described by the expression

$$I_L(D)/I_0 = 1-(h/h_0)(1-\exp(-(D/D_0)^{\alpha})). \quad (3)$$

The equation (3) was used to calculate the theoretical curves superposed on the experimental points in Fig. 1. Obvious, the experimental data are described quite well in the model proposed.

The characteristic doses obtained for different sample temperatures are presented in Fig. 2 in the form of the curve $\ln(D_0)=f(1/T)$. As one can see, the experimental points fall on a straight line — the pair correlation coefficient is close to 1 ($R=0.98$). Therefore it can be concluded that the electronic degradation of the photoluminescence of porous silicon is of an activational character, and the temperature dependence of D_0 is described by the Arrhenius law

$$D_0 = D_{00}\exp(-\Delta E/kT), \quad (4)$$

where ΔE is the activation energy of electron-stimulated quenching of the photoluminescence of porous silicon and D_{00} is a preexponential factor. A least-squares approximation of the data presented in Fig. 2 yielded the parameters in the equation (4): $\Delta E = 0.13$ eV and $D_{00}=5\times 10^{13}\text{cm}^{-2}$.

It should be noted that the empirical parameter α decreases with increasing temperature from 3.44 at 20 °C to 0.73 at 125°C. This fact, in our opinion, is attributable to the acceleration of the removal of hydrogen atoms from porous silicon when the silicon is heated. The decrease in α with increasing electron energy[9] likewise indicates that the diffusion of atoms desorbed from the surface of quantum wires plays a large role in the kinetics of the decrease in the intensity of the photoluminescence of porous silicon. In this connection, we propose the following model for estimating the diffusion coefficient of hydrogen in porous silicon. Since porous silicon is a fine-pore material and is in a vacuum during the electronic treatment, i.e. the gas pressure in the pores is low, only a Knudsen diffusion mechanism need be considered.[10] In this case, the classical diffusion of hydrogen in the volume of the quantum wires and pores as well as along the surfaces of the pores is neglected because of the long diffusion path along the tortuous walls of the pores. We write the equation of continuity for the one-dimensional case in the general form

$$dN_{Hg}/dt = k_C(N_S - N_{\text{Hs}}) - k_D N_{\text{Hs}} - D_{Kn}d^2N_{Hg}/dx^2, \quad (5)$$

where N_{Hg} and N_{Hs} are the density of hydrogen atoms in the pores in the gas phase and in the chemisorbed state; N_S is the density of surface bonds in the porous silicon (prior to irradiation most surface bonds are occupied by hydrogen); k_D and k_C are the rates of electronic stimulation of the destruction of hydrogen complexes and their restoration; and, D_{Kn} is the Knudsen diffusion coefficient. The x axis is perpen-

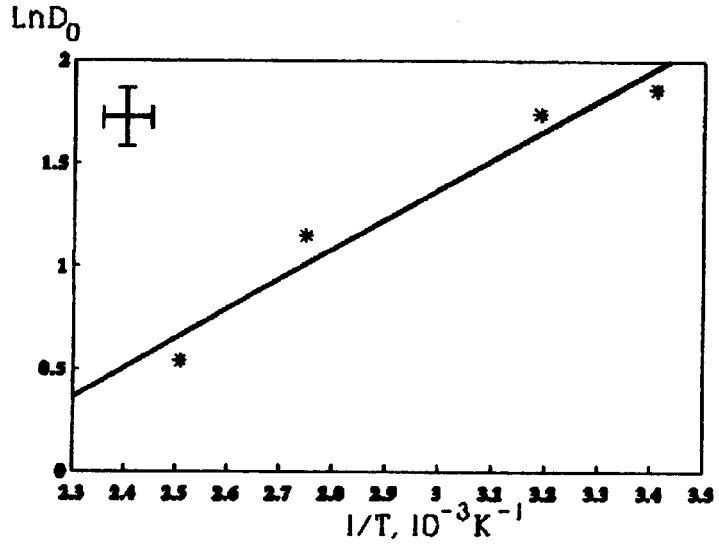

FIG. 2. The characteristic dose for electronic stimulation of photoluminescence quenching versus the reciprocal of the temperature of porous silicon.

dicular to the surface of porous silicon and is directed into the volume of the material. Since kilovolt electrons are used for irradiation, it can be assumed that the hydrogen desorption rate is much higher than the hydride restoration rate. Then, when the electronic irradiation starts, practically all hydrogen atoms are instantaneously desorbed and the amount of hydrogen in the pores will be determined only by the removal of the hydrogen atoms by diffusion. We write the linear approximation of Fick's first law

$$J_H = -D_{Kn}(N_{Hg} - N_\nu)/\delta = -N_{\mathrm{Hs}}\nu, \tag{6}$$

where $N_\nu = 0$ is the density of hydrogen outside the surface of porous silicon (in the vacuum); δ is the length of the diffusion zone; and, $\nu = d\delta/dt$ is the rate of advancement of the diffusion zone in porous silicon. Integrating the equation (6) gives the relation $\delta^2 = 2D_{Kn}t/\theta$, where for the present model $\theta = N_{Hg}/N_{\mathrm{Hs}}$ is the porosity of the sample and t is the electronic treatment time. The process of quenching of the photoluminescence by the electrons can be regarded as instantaneous because of the activity of the broken bonds. Then, after irradiation stops the broken surface bonds are quite rapidly saturated by the hydrogen remaining the gas phase. The decrease in the intensity of the photoluminescence will therefore be determined only by the amount of hydrogen which has diffused out of the porous silicon during irradiation, and the expression (3) can be written in the form

$$qI_L(D)/I_0 = 1 - \sqrt{D_{Kn}t/2\theta h_0^2}\ . \tag{7}$$

Analysis of the experimental data presented in Fig. 1 in accordance with the expression (7) and the data $h_0 = 0.5\ \mu$m, $\theta = 0.5$ (Ref. 7) gave the following expression for the diffusion coefficient of hydrogen in porous silicon:

$$D_{Kn} = 6.3\times 10^{-9}\exp(-0.17[\mathrm{eV}]/kT)[\mathrm{cm}^2/\mathrm{s}]. \tag{8}$$

At $T = 20$ °C, $D_{Kn} = 8\times 10^{-12}$ cm^2/s. This value is almost three orders of magnitude higher than the hydrogen diffusion coefficient in the volume of single-crystal silicon.[11] This confirms the conjecture that the diffusion in porous silicon occurs by the Knudsen mechanism.

In summary, in the present Letter we obtained the dependence of the integral photoluminescence intensity of *n*-type porous silicon on the electron irradiation dose for different substrate temperatures ($T = 20$–125 °C). The experimental results can be explained by a decrease in the number of radiative recombination centers as a result of electron-stimulated destruction of SiH_2 groups on the surface of the quantum wires. It was shown that the temperature dependence of the characteristic dose or electron-stimulated quenching of photoluminescence of porous silicon follows an Arrhenius law, and the activation energy of this process was determined. A model of the diffusion removal of hydrogen from porous silicon was presented and the hydrogen diffusion coefficient in porous silicon was estimated.

This work was financed by a Goskomvuz grant.

[1] L. T. Canham, Appl. Phys. Lett. **57**, 1046 (1990).
[2] C. Tsai, K.-H. Li, J. Sarantz *et al.*, Appl. Phys. Lett. **59,** 2814 (1991).
[3] I. M. Chang, G. S. Chuo, D. C. Chang *et al.*, J. Appl. Phys. **77**, 5356 (1995).
[4] B. M. Kostishko, A. M. Orlov, and T. G. Emel'yanova, Pis'ma Zh. Tekh. Fiz. **22**(10), 68 (1996) [Tech. Phys. Lett. **22**, 417 (1996)].
[5] E. V. Astrova, A. A. Lebedev, A. D. Remenyuk *et al.*, Fiz. Tekh. Poluprovodn. **29**, 1649 (1995) [Semicond. **29**, 858 (1995)].
[6] S. Migazaki, K. Sniba, K. Sakamoto *et al.*, Optoelectron.: Devices and Technol. **7**, 95 (1992).
[7] B. M. Kostishko, A. M. Orlov, and T. G. Emel'yanova, Izv. Ross. Akad. Nauk, Neorg. mater. **32**, 1432 (1996).
[8] F. F. Vol'kenshteĭn, *Electronic Processes on Semiconductor Surfaces During Chemisorption* [in Russian], Nauka, Moscow, 1987.
[9] B. M. Kostishko, A. M. Orlov, and S. N. Gerasimov, in *Abstracts of Reports at the 1st All-Russia Conference on Materials Engineering and the Physicochemical Principles of the Production of Doped Silicon Crystals ''Silicon-96''* [in Russian], Moscow, 1996, p. 158.
[10] T. Sherwood, R. Piford, and C. Wilkey, *Mass Transfer* [Russian translation], Khimiya, Moscow, 1982.
[11] S. J. Paerton, J. M. Corbett, and T. S. Shi, J. Appl. Phys. A **43**, 153 (1987).

Translated by M. E. Alferieff

Kinetics of dislocation ensembles in deformable irradiated materials

N. V. Kamyshanchenko, V. V. Krasil'nikov, I. M. Neklyudov, and A. A. Parkhomenko

Khar'kov Physicotechnical Institute
(Submitted April 30, 1997)
Pis'ma Zh. Tekh. Fiz. **23**, 51–54 (September 26, 1997)

A model of for the development of plastic deformation processes in an irradiated material is proposed. The model is based on the kinetics of dislocation ensembles interacting with defects of different nature. It is shown that the appearance of radiation embrittlement of reactor materials cannot be adequately described if the pseudorelativistic dynamic effects are neglected.
 [S1063-7850(97)02409-9]

Radiation hardening of materials can be associated with the formation of curves of stretching of a ''yield tooth'' and the Chernov–Lüders area,[1,2] which attest to plastic instability in materials.

In the present work we studied the development of plastic instability taking account of the dependence of the velocity distribution function of an ensemble of dislocations. The subject of the description are mobile dislocations that interact with fixed obstacles of different nature but are not stopped (do not ''get caught'') by the obstacles, for example, they move in a channeling regime. This situation is possible in the case of the deformation of an irradiated material when ensembles of dislocations ''cut up'' obstacles in the form of small clusters, loops, and micropores. It is obvious that such a situation can occur both in the presence of a wide spectrum of dislocation velocities (energies) and with different mechanisms of interaction of dislocations with obstacles.

We shall investigate the development of plastic deformation on the basis of a kinetic equation for the distribution function $n(\mathbf{r},\mathbf{v},t)$ of dislocations interacting with some fixed obstacles over the coordinates $\mathbf{r}$, velocities $\mathbf{v}$, and time t:

$$\frac{\partial n}{\partial t}+\mathbf{v}\cdot\frac{\partial n}{\partial \mathbf{r}}+\mathbf{a}\cdot\frac{\partial n}{\partial \mathbf{v}}=\frac{|\mathbf{v}|^m}{A}\frac{1}{4\pi}\int d\Omega_v\cdot(n(\mathbf{r},\mathbf{v}',t)-n(\mathbf{r},\mathbf{v},t)), \tag{1}$$

where $d\Omega_{\mathbf{v}}$ is an element of solid angle in velocity space and $\mathbf{a}$ is the acceleration imparted to a dislocation by, for example, an external stress σ. Here the frequency of collisions with obstacles for a dislocation moving with velocity $\mathbf{v}$ equals $|\mathbf{v}|^m/A$ (we shall assume below that $m<-1$), where A is a constant quantity that takes account of the presence of stops of different nature and density. In an irradiated material A will be proportional to the relative radiation hardening of the material: $A\sim\sigma_{\rm ir}/\sigma_{\rm nonir}$.

The equation (1) holds in the spatially uniform case, i.e. when the distribution function of an ensemble of dislocations changes very little over a distance of the order of the distance between obstacles: $\Delta=n_1-n_2\ll d$ (d is the average distance between stops).

To equation (1) we add the initial condition $n(\mathbf{v},0;\mathbf{v}_0)=\delta(\mathbf{v}-\mathbf{v}_0)$, signifying that at time $t=0$ all dislocations have a velocity close to $\mathbf{v}_0$.

We now introduce the parameter $\rho^*(\mathbf{v}_0,t;m)=\rho_{\rm act}/\rho_{\rm tot}$, where $\rho_{\rm act}$ is the density of dislocations which have passed ''through'' obstacles and $\rho_{\rm tot}$ is the total density of dislocations. The parameter $\rho^*(\mathbf{v}_0,t;m)$ indicates the relative fraction of dislocations in an ensemble which have passed ''through'' an obstacle. The following integral equation can be established from the physical meaning of the distribution function $n(\mathbf{v},t;\mathbf{v}_0)$ as the probability density for dislocations moving with velocity $\mathbf{v}$:

$$n(\mathbf{v},\mathbf{t};\mathbf{v}_0)=\rho^*(\mathbf{v}_0,t;m)\,\delta(\mathbf{a}t+\mathbf{v}_0-\mathbf{v})-\int_0^t dt'\,\frac{\partial}{\partial t'}\rho^*(\mathbf{v}_0,t';m)\,\frac{1}{4\pi}\int d\Omega_{\mathbf{w}}n(\mathbf{v},t-t';\mathbf{w}|\mathbf{a}t'+\mathbf{v}_0|), \tag{2}$$

where w is a unit vector ($|\mathbf{w}|=1$) of arbitrary direction. The first term in Eq. (2) is the fraction of dislocations which have passed through an obstacle and have acquired over a time t the velocity $\mathbf{a}t+\mathbf{v}_0$. The second term takes account of the fraction of dislocations whose velocity has assumed an arbitrary direction $\mathbf{w}$ as a result of collisions with obstacles. These directions knock dislocations out of the probability density $n(\mathbf{v},t;\mathbf{v}_0)$, as is indicated by the minus sign in front of the second term. Using Eq. (2) we obtain from the kinetic equation (1) an equation for ρ^*:

$$\frac{\partial\rho^*(\mathbf{v}_0,t;m)}{\partial t}+\frac{|\mathbf{a}t+\mathbf{v}_0|^m}{2A}\rho^*(\mathbf{v}_0,t;m)=0. \tag{3}$$

Assuming that the direction of the initial velocity $\mathbf{v}_0$ is the same as the vector of the applied load σ, we find

$$\rho^*(\mathbf{v}_0,t;m)=\exp\left(\frac{|\mathbf{v}_0|^{m+1}-(|\mathbf{a}|t+|\mathbf{v}_0|)^{m+1}}{2|\mathbf{a}|A(m+1)}\right) \tag{4}$$

with $m\neq-1$. For $m<-1$ the solution (4) has the asymptotic form

$$q=\lim_{t\to\infty}\rho^*(\mathbf{v}_0,t;m+1)=\exp\left(\frac{|\mathbf{v_0}|^{m+1}}{2A|\mathbf{a}(m+1)|}\right). \tag{5}$$

This is the fraction of dislocations with initial velocity $\mathbf{v}_0\|\sigma$ that pass through an obstacle. As $|\mathbf{v}_0|\to\infty$ (or $|\mathbf{a}|$ increases) this fraction approaches 1, i.e. for high velocities (energies) the dislocations ''slip past'' the obstacles without stopping.

Figure 1 displays the fraction of dislocations that overcome obstacles in a dynamic regime as a function of the dislocation velocity for four cases: q_1 corresponds to the

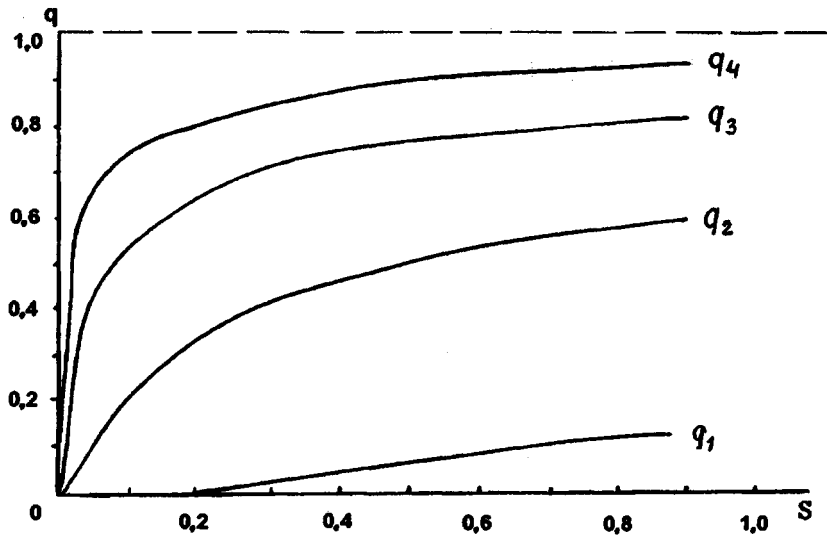

FIG. 1.

initial material ($A_1=1$), q_2, q_3, and q_4 correspond to the irradiated materials ($A_2=4$, $A_3=8$, and $A_4=20$). The quantity $s=\nu_0/c$, where c is the speed of sound, is plotted along the abscissa. According to our data as well as the data analyzed by others,[3] the relative increase in the yield stress of a material by a factor of 4–20 is observed in most model and reactor materials even at doses of 10^{-2}, ..., 10^{-1} displacements per atom. Furthermore, one can see that, under otherwise equal conditions, in irradiated materials the fraction of dislocations that overcome obstacles in a dynamic regime (according to Ref. 4, the criterion for a dynamic or ''pseudorelativistic'' regime is dislocations reaching velocities ~ 0.1 times the speed of sound) already becomes substantial.

According to the data in Fig. 1, in irradiated materials a dynamic (pseudorelativistic) deformation regime is reached for lower dislocation velocities.

The model presented in this Letter could have a direct bearing, in our opinion, for example, on the problem of brittleness of irradiated materials in vessel reactors, since the deformation and destruction of vessel steels are accompanied by dynamic processes under dynamic channeling conditions.

[1] I. M. Neklyudov and N. V. Kamyshanchenko, *The Structure and Radiation Damage in Construction Materials* [in Russian], Metallurgiya, Moscow, 1966, Part 3, pp. 5–49.
[2] A. V. Volobuev, L. S. Ozhigov, and A. A. Parkhomenko, VANT, Ser. FRP i RM, No. 1(64), 3 (1996).
[3] V. F. Zelenskiĭ, I. M. Neklyudov, L. S. Ozhigov *et al.*, *Some Problems of the Physics of Radiation Damage in Materials* [in Russian], Naukova dumka, Kiev, 1979.
[4] L. E. Popov, *Mathematical Simulation of Plastic Deformation* [in Russian], Tomsk University Press, Tomsk, 1992.

Translated by M. E. Alferieff

Oscillations in a system of two model self-excited oscillators based on vacuum microtriodes with unidirectional coupling

A. A. Koronovskiĭ, V. I. Ponomarenko, and D. I. Trubetskov

Institute of Radio Engineering and Electronics, Russian Academy of Sciences (Saratov Affiliate), Saratov State University (GosUNTs ''College'')

Pis'ma Zh. Tekh. Fiz. **23**, 55–61 (September 26, 1997)

The results of a numerical investigation of the behavior of two model self-excited oscillators with vacuum microtriodes coupled with one another by a unidirectional coupling are presented. It is shown that the behavior of such self-excited oscillators (each of which, being a system with one degree of freedom, can exhibit only periodic oscillations) is quite complicated: Not only periodic and quasiperiodic but also chaotic oscillations are possible in the system. A state diagram is constructed in the plane of the controlling parameters frequency detuning — magnitude of the coupling. © *1997 American Institute of Physics.* [S1063-7850(97)02509-3]

In Ref. 1 the idea of developing new nonlinear active vacuum media with field-emission impregnations was advanced. A natural step in the direction of realizing such a medium is the investigation of a ''model media'' in the form of arrays or lattices of coupled self-excited oscillators in a microvacuum implementation.[2–4]

In the present Letter we take the first step in this direction: The behavior of two self-excited oscillators with unidirectional coupling is investigated in a numerical experiment. The circuit with the self-excited oscillators is displayed in Fig. 1. Each oscillator is identical to the self-excited oscillator described in Refs. 2 and 4: The anode current of the vacuum microtriode depends on the grid voltage (with a fixed anode voltage) in accordance with the Fowler–Nordheim law,[5,6] expressed in the form

$$I_a(U)=A^*F^2(aU+b)^2\exp\left(-\frac{B^*\varphi^{3/2}}{F(aU+b)}\right)=A(oU+b)^2\exp\left(-\frac{B}{aU+b}\right) \tag{1}$$

where A^* and B^* are constant parameters, φ is the work function, F is the field intensification factor, a and b are geometric constants, $A=A^*F^2$, and $B=(B^*\varphi^{3/2})/F$. Since the nonlinear characteristic of the active element does not saturate, a diode with a nonlinear exponential characteristic is introduced as a dissipative element into the feedback circuit of each oscillator.[2–4] The current-voltage characteristic of the diode has the form[7]

$$I_R(U)=I_0\left(\exp\left(\frac{U_e}{k_BT}\right)-1\right), \tag{2}$$

where I_0 is the theoretical reverse current of the diode, k_B is Boltzmann's constant, T is the temperature, and e is the electron charge.

In accordance with Kirchhoff's laws, we can write the following equations for two self-excited oscillators coupled by a unidirectional coupling and connected in the manner shown in Fig. 1:

$$\begin{aligned} &U_i=L_i\frac{dI_{L_i}}{dt}+M_i\frac{dI_{a_i}}{dt}, \quad i=1,2;\\ &I_{C_i}=-C_i\frac{dU_{C_i}}{dt}, \quad i=1,2;\\ &I_{C_1}=I_{R_1}(U_1)+I_{L_1};\\ &I_{C_2}=I_{R_2}(U_2)+I_{L_2}+I_{\mathrm{C}}. \end{aligned} \tag{3}$$

Writing the equations (3) in a dimensionless form, we obtain a system of ordinary nonlinear differential equations describing the dynamics of the system under study:

$$\begin{aligned} &\frac{dx_1}{d\tau}=\alpha\{-i_r(x_1)-\beta[y_1-\gamma i_a(x_1)]\},\\ &\frac{dy_1}{d\tau}=x_1,\\ &\frac{dx_2}{d\tau}=-i_r(x_2)-y_2+i_a(x_2)-s(x_2-x_1),\\ &\frac{dy_2}{\tau}=x_2, \end{aligned} \tag{4}$$

where $t=\tau\sqrt{L_2C_2}$; τ is the dimensionless time; $x_{1,2}=U_{1,2}/U_m$ are dimensionless dynamic variables corresponding to the grid voltage of the vacuum microtriode in the first and second self-excited oscillators, respectively; $y_{1,2}=\int x_{1,2}(\tau)d\tau$; $\rho=\sqrt{L_2/C_2}$ is a dimensionless parameter characterizing the second self-excited oscillator; $U_m=B/a$ and $\sigma=b/B$ are parameters characterizing the vacuum microtriode; $i_a(x)=\mu(x+\sigma)^2\exp(-1/(x+\sigma))$ is a dimensionless nonlinear characteristic of a vacuum microtriode; $s=\rho/R_c$ is a dimensionless coupling parameter of the self-excited oscillator; $k=eU_m(k_bT)$and $g_0=I_0\rho e/(k_bT)$ are the parameters of the diode playing the role of a nonlinear dissipative element; $i_r(x)=g_0(\exp(kx)-1)/k$ is the dimensionless current-voltage characteristic of the diode; $\mu=AaBM_2/\sqrt{L_2C_2}$ is a dimensionless feedback parameter of the second self-excited oscillator; $\alpha=C_2/C_1$, $\beta=L_2/L_1$, and $\gamma=M_1/M_2$are dimensionless parameters characterizing

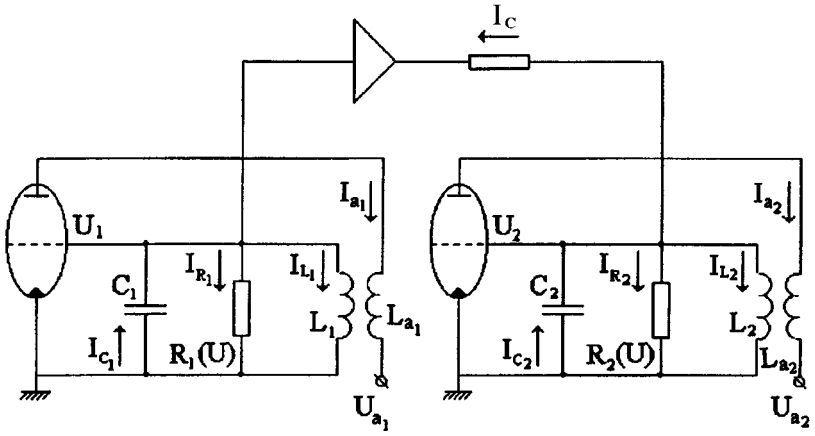

FIG. 1. Circuit diagram of two unidirectionally coupled self-excited oscillators with vacuum microtriodes.

the mismatch of the self-excited oscillators. We note that the form of the dimensionless equations (4) was chosen so that the dimensionless parameters introduced for one self-excited oscillator with a vacuum microtriode (see Refs. 2 and 4) would retain their form and the equations, which decouple into two independent subsystems as $s \to 0$, would be identical to the equation in Refs. 2 and 4.

The derivation of the equations (4) assumed that both the vacuum microtriodes and diodes in both self-excited oscillators are identical. In other words, $I_{a_1}(U) = I_{a_2}(U)$ and $I_{R_1}(U) = I_{R_2}(U)$. We shall assume below that $L_1 = L_2$ and $M_1 = M_2$ and, correspondingly, $\beta = 1$ and $\gamma = 1$. In this case the two coupled self-excited oscillators will differ only by the capacitance and the parameter α reflecting the mismatch of the self-excited oscillators will in this case equal the squared ratio of the characteristic frequencies of the *LC* circuits of the oscillators.

In the course of the investigations of the behavior of the two above-described self-excited oscillators with unidirectional coupling, we constructed a diagram of the oscillation states of the second self-excited oscillator in the plane of the controlling parameters $\alpha - s$ (''mismatch of the self-excited oscillators — coupling strength'') (Fig. 2a). This diagram was constructed on the basis of a family of bifurcation dia-

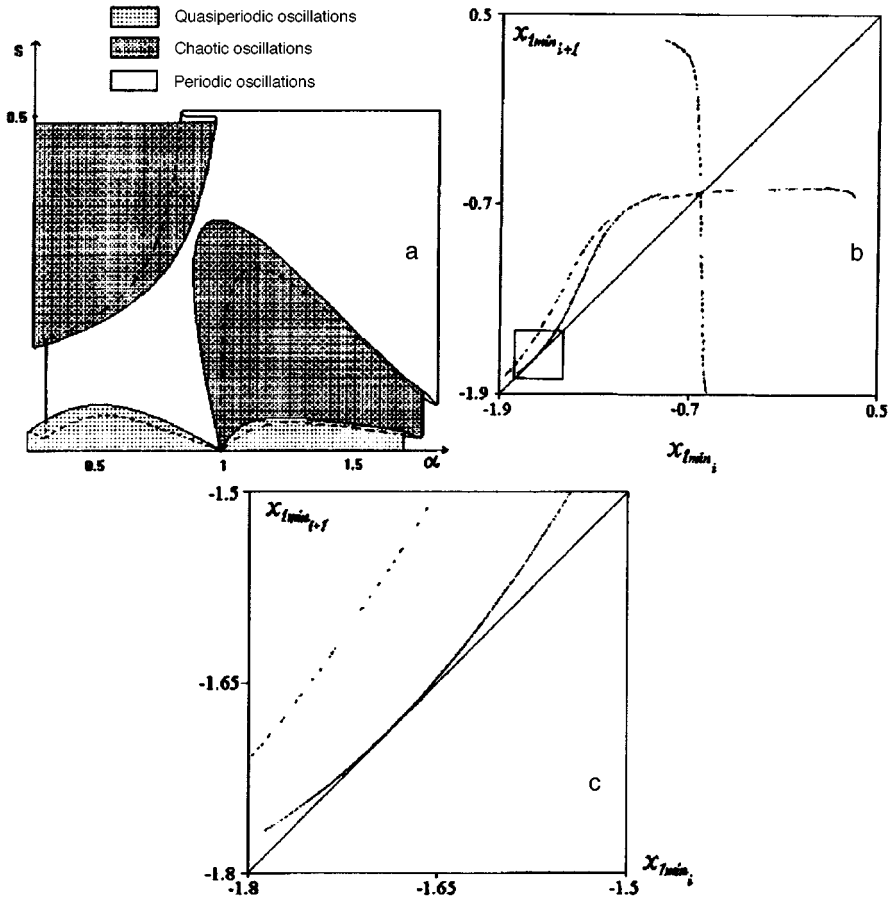

FIG. 2. a — Two-parameter state diagram of the oscillations of the first self-excited oscillator as a function of the controlling parameters α and s. b — Iterative map obtained at the point with controlling parameters $\alpha = 0.95$ and $s = 0.435$ that clearly shows the transition to chaos via intermittency. c — Fragment of the map presented in Fig. 2b.

grams obtained with numerical simulation of the system (4) by a fourth-order Runge–Kutta method (with time step $h=0.01$) with adiabatically slow variation of the controlling parameters α and s. The remaining parameters of the system were chosen, by analogy to Refs. 2 and 4, as follows: $\sigma=4.5$, $k=10$, $g_0=0.54$, and $\mu=0.2$. We note that in constructing the two-parameter state diagram on the basis of the family of bifurcation diagrams we used the method presented in Ref. 8, in which each bifurcation diagram was constructed twice: The controlling parameter was increased in the first case and decreased in the second case. The values of the parameter for which a transition occurred from one oscillatory state into another were compared with one another for both bifurcation diagrams, and if these two values were different, then this was interpreted to mean that the behavior of the system is not unique in this region of controlling parameters, and this was displayed in the state diagram by a hysteresis folding.

As one can see from Fig. 2a, the state diagram in the plane of controlling parameters α and s has a quite odd form: For a small coupling parameter quasiperiodic oscillations are realized in the second self-excited oscillator. (We note that since the coupling is unidirectional, only periodic oscillations are realized in the first oscillator.) As the coupling parameter increases, a sharp jump occurs from quasiperiodic oscillations either to chaotic ($\alpha>1.0$) or periodic ($\alpha<1.0$) oscillations; this corresponds in the plane of controlling parameters to a folding and a transition to a different sheet. As the coupling parameter s increases further, a transition occurs either from periodic to chaotic oscillations ($\alpha<1.0$) or, conversely, from chaotic to periodic oscillations ($\alpha>1.0$). In the case when both self-excited oscillators are identical (i.e. $\alpha=1$), in a system which moves in the plane of controlling parameters in the direction of increasing coupling parameter there are no quasiperiodic oscillations with a small coupling parameter or chaotic oscillations with large values of s. At the same time, moving in the state diagram from the region of chaotic oscillations ($\alpha>1$) with fixed parameter s in the direction of decreasing α, one can see from Fig. 2a that it is possible to reach the region of chaotic oscillations with $\alpha=1$ also.

The question of the scenario of the transition from periodic to chaotic oscillations merits special attention. As the foregoing investigation shows, in both cases $\alpha<1.0$ (with increasing parameter s) and $\alpha>1.0$ (with decreasing coupling parameter) the transition from periodic to chaotic oscillations occurs through intermittency: Analysis of the temporal realizations of the oscillations of the second oscillator shows alternation of laminar and turbulent phases, the duration of the turbulent phases in the temporal realizations increasing with the supercriticality. A stricter proof of the transition to chaos via intermittency is the form of the iterative map $x_{1\min_{i+1}}=f(x_{1\min_i})$ shown in Fig. 2b. This map was obtained for the system (4) near the bifurcation point for the controlling parameters $\alpha=0.95$ and $s=0.435$. Figure 2c shows in detail a fragment of this map illustrating clearly the transition to chaos via intermittency: A corridor, corresponding to laminar phases of the temporal variations, between the plot of the map and the straight line $x_{1\min_{i+1}}=x_{1\min_i}$ is clearly seen in the diagram. As the coupling parameter s decreases, the plot of the map and the straight line touch. This corresponds to a tangential bifurcation and appearance of periodic oscillations.

It is also worth noting that sheets of periodic oscillations also exist in the region of chaotic oscillations. The transition to chaos from the sheets can also occur via a cascade of period-doubling bifurcations.

In summary, in the present Letter we investigated the dynamics of a new radiophysical system — two unidirectionally couled oscillators whose active elements are field-emission vacuum microtriodes. The results obtained also extend the understanding of the possible behavior of coupled oscillators.

This work was supported by the Russian Fund for Fundamental Research, Grant No. 96-02-16753.

[1] D. I. Trubetskov, A. G. Rozhnev, and D. V. Sokolov, *Lectures on Microwave Vacuum Microelectronics* [in Russian], GosUNTs ''Kolledzh'' Press, Saratov, 1996.
[2] V. I. Ponomarenko and D. I. Trubetskov, Dokl. Akad. Nauk **337**, 602 (1994).
[3] V. I. Ponomarenko and D. I. Trubetskov, Izv. vyssh. uchebn. zaved., PND, No. 6, 56 (1994).
[4] D. I. Trubetskov, E. S. Mchedlova, V. G. Anfinogenov, V. I. Ponomarenko, and N. M. Ryskin, Chaos **6**, 358 (1996).
[5] T. Asano, IEEE Trans. on ED **ED-38**, 2392 (1991).
[6] W. J. Orwis, C. F. McConaghy, D. R. Ciarlo, J. H. Yee, and E. W. Hee, IEEE Trans. on ED **ED-36,** 2651 (1989).
[7] V. L. Bonch-Bruevich and S. G. Kalashnikov, *Semiconductor Physics* [in Russian], Nauka, Moscow, 1977.
[8] A. V. Andrushkevich, A. A. Kipchatov, L. V. Krasichkova, and A. A. Koronovskiĭ, Izv. vysh. uchebn. zaved., Radiofiz. **38**, 1195 (1995).

Translated by M. E. Alferieff

Advantage of Josephson bridges in synchronized arrays for a voltage standard

Kh. A. Aĭnitdinov, E. I. Efanov, and A. M. Klushin

''Ikar'' Design Office, Nizhniĭ Novgorod
(Submitted April 7, 1997)
Pis'ma Zh. Tekh. Fiz. **23**, 62–68 (September 26, 1997)

A novel possibility of obtaining a standard voltage of the order of 1 volt with fewer superconducting bridges than Josephson junctions in existing voltage standards is discussed. It is proposed that a special feature of the current-voltage characteristic of superconducting bridges be utilized — a group of current steps induced by microwave radiation is observed on it.
 [S1063-7850(97)02609-8]

The development of improved devices based on synchronized arrays of a large number of Josephson junctions (voltage standard, oscillators, multipliers, submillimeter- and IR-range mixers, and others) is the most pressing, intensely developing field of the practical applications of the Josephson effect.[1–3] A large-array dc voltage standard of up to 1 V with a step of 150 μV, equal to the voltage of a current step induced by microwave radiation, is under intensive development at the NIST in the USA.[1] Another group is developing an oscillator based on a synchronized Josephson array in for submillimeter and IR ranges that makes it possible to vary the oscillation frequency continuously in a wide band, specifically, in Ref. 3 in the band 100–500 GHz.

The possibility of a voltage standard based on an array of a large number of serially connected high-T_c superconducting junctions, operating at liquid-nitrogen temperature, is being investigated by a group which has been involved since 1970 in developing a voltage standard.[4] In the present Letter we propose a new possibility for obtaining a standard Josephson voltage of 1 V with a much smaller number of junctions in an array than in existing standards. The technique is to use a special feature of the stepped current-voltage characteristic of bridges and point contacts that distinguishes them from tunnelng contacts. This feature is due to the so-called ''excess'' superconducting current and consists of the fact that a group of current steps, which are close in amplitude, is induced at high voltages on the current-voltage characteristics of bridges by microwave irradiation in a wide range. This group extends the possibility of combining in a voltage interval a group of current steps of two or more serially connected contacts with somewhat different (as a result of the technological variance) parameters — resistance and critical current. According to the theory of Refs. 5 and 6, the current through a bridge with dimensions less than the penetration depth of the magnetic field in the superconductor (the size of a vortex superconducting current) is given by the formula

$$I = V/R + I_u(V) + I_s \sin\varphi, \tag{1}$$

where $\varphi(t) = 2e\int dt V(t)/\hbar$, V is the voltage on the bridge, t is the time, and R is the resistance of the bridge. The current through the bridge, in contrast to a tunneling contact, contains an additional component — an excess superconducting current $I_{\rm exc}$, which at $V=0$ jumps from $-I_{\rm exc}(0)$ to $I_{\rm exc}(0)$. The magnitude of the excess current is determined[7] by the current density at the superconducting edges of the bridge, which is proportional to the diameter of the bridge and depends on the temperature in the limit $V\to 0$ in the same manner as the critical current $I_c = I_s + I_{\rm exc}(0)$.

In the fixed-current regime, i.e. for contact resistance R less than the external impedance, $I(t) = \ddot{I} + \hat{I}\cos\omega_0 t$, in the approximation $\hat{I} > I_0(0) > I_s$ for the amplitude I_N of the N-th induced step at high voltages

$$2eI_N R/\hbar\omega_0 < 1, \tag{2}$$

where the following expression was obtained in Ref. 5

$$I_N \approx I_s(0)\left|J_{p-a}(\hat{A}) + \mathrm{Re}[\exp(\Phi_1 - \Phi_2)H^{(1)}_{p+a}(\hat{A})]\right|, \tag{3}$$

where $p = 2e\ddot{I}R/\hbar\omega_0$, $a = 2eI_{\rm exc}R/\hbar\omega_0$, $\hat{A} = 2e\hat{I}R/\hbar\omega_0$, $\Phi_i = 2eR/\hbar\omega_0[\hat{I}\sin\omega_0 t_i + \omega_0 t_i(\ddot{I} \pm I_{\rm exc})]\,\theta(\hat{I} - \ddot{I} \pm I_{\rm exc})$, $\omega_0 t_i = \cos^{-1}\{(\pm I_{\rm exc} - \ddot{I})/\hat{I}\}$, $i = 1,2$ correspond to the upper and lower signs in the formula, $\theta(x)$ is the Heavside function, $J_p(x)$ and $H^{(1)}_p(x)$ are Bessel and Hankel functions, respectively. It follows from Eq. (2) that in the range of dc currents $\hat{I} - I_{\rm exc} \geqslant \ddot{I} \geqslant \hat{I} + I_{\rm exc}$, containing $\delta N \approx 4eI_{\rm exc}R/\hbar\omega_0$ steps, the amplitude of the currents is maximum and changes very little from one step to another.

In an experiment[5] on *Nb–Nb* point contacts with $I_{\rm exc}(0)R \approx 0.5$–$1$ mV under microwave irradiation with $f = \omega_0/2\pi = 10$ GHz, the group described contained 40–80 steps, while in tunneling contacts such a group is described by the Bessel function $I_N = I_s J_N(\hat{A})$ and contains[8] $\delta N = 2N^{1/3}$ steps, where $N = 2eV^-/\hbar\omega_0$, V^- is a dc voltage, specifically, $\delta N \approx 8$ for $\ddot{I}R = 2$ mV. The differential equation

$$CdV/dt + V/R + j dt V/L + I_s \sin\varphi + I_{\rm exc}(V) = \ddot{I} + \hat{I}\cos\omega_0 t, \tag{4}$$

describing a Josephson junction with an internal resistance R and a shunting characteristic capacitance C and inductance L in a fixed-current regime was solved on a computer by the finite-difference method. For the initial random values $\varphi(0) = 0$, $V(0) = 0$ the resulting dc voltage $V^- = (\varphi(40/f) - \varphi(20/f))/40\pi$ was averaged over 20 periods $1/f$ and plotted along the ordinate in units of $h\omega_0/4\pi e$. The quantity $\ddot{I}$ was plotted on the abscissa in units of $h\omega_0/4\pi eR$.

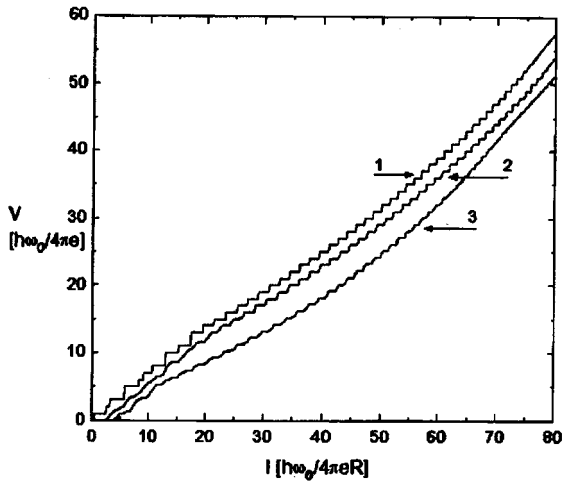

FIG. 1. Current-voltage characteristics of Josephson contacts exposed to microwave radiation: *1* — Current-voltage characteristic of one junction, measured from the monitor screen of a personal computer, $I_{\rm exc}=22$, $I_s=5$, $\hat{I}=48$ in units of $h\omega_0/4\pi eR$; *2, 3* — experimental current–voltage characteristics of two and three, respectively, serially connected $YBa_2Cu_3O_{7-x}$ bicrystalline high-T_c superconducting junctions (the scale along the axes is enlarged by a factors of *2* and *3*, respectively; the current–voltage characteristics are shifted along the current axis.

In the computer calculations, without the restriction (2) on I_s, the first wide group contained $\delta N\approx 4eI_0R/\hbar\omega_0$ current steps, but to obtain large δN in practice it is much more difficult to increase I_s than $I_{\rm exc}(0)$.

On the experimental current-voltage characteristic of two serially connected bicrystalline $YBa_2Cu_3O_{7-x}$ high-T_c superconducting junctions (curve *2* in Fig. 1), the group noted contains 40 steps in the region 1–4 mW. For comparison, a stepped current–voltage characteristic, calculated on a PC/AT personal computer, of one junction with parameters $(R,I_{\rm exc},I_s)$ close to the experimental values and taken from the monitor screen (curve *1*), is displayed in the Fig. 1. In contrast to the IVC of one junction, in the region 0–0.5 mV the current steps are smoothed (curve *2*), since the resistance and critical currents of two high-T_c superconducting junctions for the experimental IVC differ by approximately 7%. Despite this difference in the parameters, the steps in the region 1–4 mV of both junctions were found to occur at the same current and were sharp. The possibility of varying the excess current $I_{\rm exc}(0)$ over wide limits is an advantage of bicrystalline junctions in developing a voltage standard based on synchronized arrays. Bijunctions were obtained by depositing 2000 Å thick YBCO films on a single-crystalline YSZ substrate consisting of two parts differing with respect to the orientation of crystallographic axes in the ab plane. A junction was obtained in the form of a bridge on the bicrystalline boundary and had a width of 4 μm, a misorientation angle of 19°, and a current density in the bridge at 67 K $j=5\times10^5$ A/cm^2 and, correspondingly, the Josephson penetration depth of the magnetic field was $\lambda_l=0.5$ μm. The technology for preparing bicontacts is described in greater detail in Ref. 9. The experimental current-voltage characteristics of the junctions were measured by a four-probe method from the screen of an oscillograph; the contacts were irradiated at frequency 18.81903 CHz. Analysis of the observed current-voltage characteristics shows that it is most likely that the junction at the location of the bicrystalline boundary contains a semiconducting interlayer as a result of oxygen vacancies in the YBCO lattice. The semiconductor properties are confirmed by the temperature dependence of the resistance $R(T)$.[1] Similarly to the *Nb–Nb* clamped contacts[5], bijunctions can be divided into two types according to the character of the dependences $R(V)$ and $R(T)$, depending on the angle of the crystallographic misorientation. For small misorientation angles the resistance grows with temperature. In such junctions the current density is high and $R(T)$ and $R(V)$ are similar to the analogous dependences for metallic bridges, specifically, the differential resistance increases with temperature and voltage (on account of the Joule heating by the current flowing through the bridge). The decrease in the resistance R with increasing T and V for junctions with a large misorientation angle[10] can be explained only by a potential barrier in the bridge for transmission of electrons.[5] With variation of the penetrability of the potential barrier in the junction, the excess current $I_0(0)$, determined by the current density in the superconducting edges of the junction, can differ for different junctions over wide limits $0<I_{\rm exc}<I_c$. Specifically, for junctions with a misorientation angle of 37° it is close to zero. Hence, junctions with quite large excess current, i.e. with a large misorientation angle 10–20°, are required to obtain a standard voltage of 1 V with the smallest number of serially connected junctions. However, the increase in $I_{\rm exc}$ is limited by the characteristic size of junctions with Josephson properties.[6] In a low-T_c superconducting bridge this dimension is the size of an Abrikosov vortex and in a high-T_c superconducting bridge it is the size of a hypervortex, i.e. the Josephson penetration depth λ_j, which decreases with increasing critical current density j_c in the bridge as $\lambda_j\sim j_c^{-1/2}$. Junctions with a sufficiently large $I_{\rm exc}$ and critical current $I_c=I_{\rm exc}+I_s$ are also required in order to develop a voltage standard operating in liquid nitrogen, where small current steps $I_N\sim I_s(T)$ are smoothed as a result of the presence of strong thermal noise[12] and also as a result of the penetration of vortex currents into the superconducting edges near the critical temperature T_c. It should be noted that, in accordance with the condition $\hat{I}-I_{\rm exc}<\ddot{I}<\hat{I}+I_{\rm exc}(0)$, to induce current steps at high voltage it is necessary to pass through the bridge a large dc $\ddot{I}$ and microwave current $\hat{I}$, which in turn increases the shot noise in the junction ,and furthermore, the current-induced magnetic field (vortices) of magnitude greater than the critical field H_c penetrates into the superconductor. Therefore single-crystalline high-T_c superconducting films with a higher critical magnetic field intensity are preferable. This clarifies the difficulties and at the same time gives points of reference for developing a technology for depositing microcircuits consisting of serially connected high-T_c superconducting junctions for a voltage standard operating at liquid-nitrogen temperature, specifically, by choosing the misorientation angle, the width, and the thickness of the barrier. The results of a comparison of a setup for a reference voltage of the current steps of a bijunction and a *Nb–Nb* point contact, connected in opposition to one another with the same voltage $\sim$2 mV, are described in Ref. 4. The volt-

age of the steps is the same to within a relative error of 10^{-6}. Measurements with a bijunction were performed in the temperature range from 4.2 to 40 K.

In closing, we shall compare the effectiveness of the proposed variant of a voltage standard based on arrays of Josephson junctions with that of existing standards. For an average voltage step for one junction of 2 mV (curve *2*) 1 V can be obtained with 500 junctions, while in the standards now being developed based on arrays of bridges,[1] matched on the first current step, 20–50 thousand junctions are required. The transition from currently operating voltage standards based on arrays of tunneling contacts to arrays of bridges involves an instability of the voltage on the former due to the discrete nonsinglevaluedness of $\ddot{I}(V)$. With only one displacement current, the voltage of the steps on the tunneling contact takes on a discrete series of values, i.e. the voltage can change abruptly, resulting in malfunctioning of the normal element certified according to the standard. However, the stepped current-voltage characteristic in a hysteresis-free regime $\ddot{I}(V)$ is single-valued.

[1] C. A. Hamilton and C. J. Burroughs, IEEE Trans. Instrum. Meas. **44**, 223 (1995).
[2] F. X. Hebrank, E. Vollmer, T. Funck, and P. Gutmann in *Niemeyer*, CPEM'96 (1996), p. 148.
[3] S. Han, B. Bi, W. Zang, and J. E. Lukens, Appl. Phys. Lett. **64**, 1424 (1994).
[4] Kh. A. Ainitdinoy, S. I. Borovitskii, V. D. Gelikonova, A. V. Komkov, C. Copetti, A. M. Klushin, E. Sodtke, L. Vonderbeck, M. Siegel, and W. Prusseit, *Ext. Abstr. of 5th Intern. Supercond. Electr. Conf. (ISEC'95)*, 1995, p. 144.
[5] Kh. A. Aĭnitdinov, S. I. Borovitskiĭ, and L. L. Malinovskiĭ, Zh. Éksp. Teor. Fiz. **76**, 1342 (1979) [Sov. Phys. JETP **83**, 356 (1979)].
[6] L. L. Malinovskiĭ, Zh. Éksp. Teor. Fiz. **110**, 661 (1996) [J. Exp. Theor. Phys. **83**, 356 (1996)].
[7] Kh. A. Aĭnitdinov and L. L. Malinovskiĭ, Fiz. Nizk. Temp. **12**, 10 (1986) [Sov. J. Low. Temp. Phys. **12**, 5 (1986)].
[8] C. A. Hamilton, Phys. Rev. B **5**, 912 (1972).
[9] A. M. Klushin, L. E. Amatuni, E. Sodtke, W. Prusseit, S. I. Borovitskii, and H. Kohlstedt, Appl. Phys. Lett. **69**, 1634.
[10] I. I. Vengrus, M. I. Kupriyanov, O. V. Snigirev *et al.*, JETP Lett. **60**, 381 (1994).
[11] A. S. Katkov, S. V. Kozyrev, V. I. Krzhimovskiĭ *et al.*, Pis'ma Zh. Tekh. Fiz. **19**, 70 (1993) [Tech. Phys. Lett. **19**, 285 (1993)].

Translated by M. E. Alferieff

Acoustic hysteresis phenomena due to the dislocation nonlinearity in crystals

G. N. Burlak and I. V. Ostrovskiĭ

Taras Shevchenko Kiev National University
(Submitted April 16, 1997)
Pis'ma Zh. Tekh. Fiz. **23**, 69–74 (September 26, 1997)

It is shown that intense ultrasound gives rise to the experimentally observed nonlocality of the acoustodislocation interaction, manifested as a hysteretetic dependence of the damping coefficient of an acoustic wave on the wave amplitude, including a decrease in damping. © *1997 American Institute of Physics.* [S1063-7850(97)02709-2]

1. A direction, of importance for practical applications, in the investigation of dynamic properties of crystals is the study of their acoustic and dislocation properties,[1,2] especially in connection with the dynamics of dislocations.

In a series of experimental works,[3–7] it was that the properties of different crystals change when ultrasound of intensity W of the order of W/cm^2 was introduced into crystal samples. It was found that ultrasound gives rise in a threshold manner to ionization and redistribution of local centers, which takes place as a result of the detachment of dislocations from pinning locations. As the amplitude of the dislocation oscillations increases, the local environment of a dislocation, including the charge states of point defects and the type and number of pinning locations, changes. A common feature of the works cited above is that the threshold changes in the properties of solids occur by a dislocation mechanism. This makes it possible to formulate the concept of nonlinearity of the dislocation subsystem in the sense that the oscillating dislocations influence many dynamical properties of crystal. It is shown below that this nonlinearity can be manifested as a strongly nonmonotonic dependence of the ultrasonic absorption coefficient on the amplitude of the ultrasound.

2. The dislocation nonlinearity of solids can be introduced as a dependence of the characteristics of a dislocation on its displacement amplitude and therefore on the amplitude of the acoustic wave interacting with it. In our model, in contrast to the amplitude-dependent internal friction known previously,[1,8] the parameters of a dislocation themselves, its effective mass, stiffness, and damping coefficient of its oscillations, become functions of the amplitude of the oscillations.

Let us examine the damping of longitudinal ultrasound propagating along the x axis in a cubic crystal that is uniform along the y and z axes. The initial equations of motion for ultrasound with displacement U and a dislocation with displacement ξ_i have the form

$$\rho\frac{\partial^2 U_i}{\partial t^2}=\frac{\partial P_{ik}}{\partial x_k};\quad A\frac{\partial^2\xi_i}{\partial t^2}+B\frac{\partial\xi_i}{\partial t}=f_i, \tag{1}$$

where A and B are the mass and damping coefficient of the oscillations of the dislocation, respectively; P_{ik} is the stress tensor; and, f_i is the force acting on the dislocation. We write the free energy F of the crystal as a function of the variable deformations U_{ij} and dislocation displacement ξ_i in the form

$$F=\frac{1}{2}\lambda_{ijkl}U_{ij}U_{kl}+\frac{1}{2}c_{ik}\xi_i\xi_k+\frac{1}{2}\tilde{\beta}_{ijkl}(b_i\xi_j+b_j\xi_i)U_{kl}, \tag{2}$$

where λ_{ijkl} are the elastic moduli, c_{ik} are the ''stiffness'' moduli of the dislocation, $\tilde{\beta}_{ijkl}$ is the acoustodislocation interaction tensor, and b_j is Burgers vector. Using the equations

$$P_{ik}=\frac{\partial F}{\partial U_{ik}};\quad f_i=-\frac{\partial F}{\partial\xi_i} \tag{3}$$

and substituting the expression (2), it is easy to calculate the right-hand sides in Eqs. (1). Then the equations of motion acquire the form ($\xi_i=\xi$, $U_{ik}=U$, i, $k=1$)

$$\frac{\partial^2 U}{\partial t^2}-c_t^2\frac{\partial^2 U}{\partial x^2}=\frac{\beta\partial\xi}{\rho\partial x};\quad A\frac{\partial^2\xi}{\partial t^2}+B\frac{\partial\xi}{\partial t}=-\beta\frac{\partial U}{\partial x}, \tag{4}$$

where c_1 is the velocity of the longitudinal wave and $\tilde{\beta}_{1j11}b_j=\beta$. Starting with a definite threshold ultrasound amplitude, equal to U_c, the amplitude of the oscillation of the dislocation reaches a critical magnitude ξ_c of the order of 1 lattice period of the crystal. The environment of the dislocations changes as a result of charge exchange and generation of point defects and multiplication of dislocations can occur. All this makes it necessary to take account of the nonlinearity of the dislocation subsystem, which can be manifested earlier than the acoustic nonlinearity. We shall do this, making the assumption that the effective mass, stiffness, and damping coefficient of the dislocation oscillations depend on the ultrasound amplitude in the form

$$A=A_0(1+A_1\xi^2),\quad C=C_0(1+C_1\xi^2), \tag{5}$$

$$B=B_0(1+B_1\xi^2+B_3\xi^4+B_2\overline{\Delta l}^{-2}). \tag{6}$$

Here A_0, B_0, C_0 and A_1, B_1, B_2, B_3, C_1 are constant coefficients and $\overline{\Delta l}^2$determines the average increase in the length of the loops, determined by dislocation pinning on impurities. We shall express $\overline{\Delta l}^2$ in the form

$$\overline{\Delta l}^2=\chi\xi^2\theta(S)\int_0^x U^2dx. \tag{7}$$

The step function $\theta(S)$ vanishes for subcritical amplitudes of the dislocation oscillations, when $S=(\xi^2-\xi_c^2)<0$ and $\theta(S)=1$ for $S>0$. The relation (7) reflects the fact that for small amplitudes $|\xi|\ll|\xi_c|$ the lengths of the loops are fixed

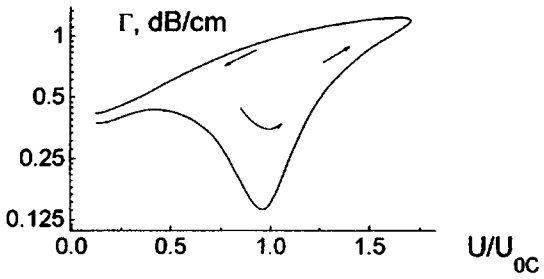

FIG. 1. Effective ultrasonic absorption coefficient versus the amplitude of the input pulse (numerical calculation) $q_2=-0.05$, $a_3=0.3$, $\gamma=0.47$.

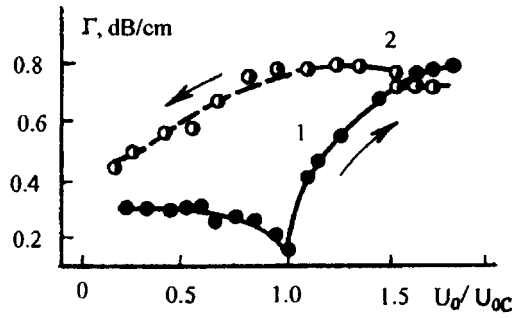

FIG. 2. Absorption coefficient for 2.02 MHz ultrasound versus the amplitude of the input pulse in a ZnS crystal (sample ZnS–10A) at room temperature.

and $\overline{\Delta}^{-2}=0$, the change $\overline{\Delta l}^2$ being proportional to the amplitude of the dislocation oscillations and the energy of acoustic vibrations in the crystal. We shall assume that the sound frequency is much less than the frequency of the characteristic dislocation oscillations, which was the case in the experiments. We solve the nonlinear system (4), substituting the expressions (5), by the method of slowly varying amplitudes, setting

$$U=U_0(x,t)e^{i(\omega_0 t-k_0 x)}+\text{c.c}, \quad \xi=V_0(x,t)e^{i(\omega_0 t-k_0 x)}+\text{c.c}, \tag{8}$$

where $U_0(x,t)$ and $V_0(x,t)$ are complex, slowly varying amplitudes of the ultrasound and the induced dislocation oscillation. From Eq. (4) we obtain an equation for the amplitude of the acoustic wave in the form

$$\left(\frac{\partial}{\partial t}+c_g\frac{\partial}{\partial x}\right)U_0=-\left[\gamma-a_2\left(1-\chi\theta(U_0^2-U_t^2)\int_0^x U_0^2 dx'\right)U_0^2+a_3U_0^4\right]U_0, \tag{9}$$

where c_g is the group velocity, the coefficients $a_{2,3}$ are associated with the nonlinearity of the dislocation subsystem and are not present here because of their complexit, and γ is the parameter characterizing the phenomenologically introduced linear absorption of sound. For small amplitudes U_0 the equation (9) describes the propagation of a damped ultrasonic pulse, γ being the damping decrement. However, in the case of ultrasound with a finite amplitude the equation (9) becomes nonlinear, and the effective absorption coefficient becomes amplitude-dependent.

The equation (9) is too complicated to solve analytically. For this reason, in the present work we performed a computer calculation by solving the equation (9) numerically and calculated on the basis of the numerical solution the dependence of the effective ultrasonic absorption coefficient

$$\Gamma=\Gamma(U_0)=-\frac{1}{L}\ln\frac{U_0(L,t+L/c_g)}{U_0(0,t)} \tag{10}$$

on the amplitude $U_0(0,t)$ of the output pulse in a crystal of length L. The damping of 2.02 MHz ultrasound has been measured experimentally in ZnS single crystals at room temperature. The computational and experimental results are presented in Figs. 1 and 2, respectively.

One can see that as the amplitude of the ultrasound increases, the damping decrement acquires a pronounced hysteresis in both the calculations and experiment. It is important to note that in contrast to the previously known amplitude-dependent internal friction in the string model of a dislocation,[1,8] our data show a decrease in damping with increasing ultrasound amplitude in the subthreshold region, followed by a steep increase in Γ under above-threshold loads. At subthreshold amplitudes (or with $\chi=0$) the dependence $\Gamma=\Gamma(U_0)$ did not exhibit hysteresis. The characteristic form of $\Gamma(U_0)$ remained similar to the lower part of the curve in Fig. 1. Experiment also does not show damping hysteresis for subthreshold ultrasound amplitudes corresponding to $U_0<U_{0C}$ in Fig. 2.

Therefore intense ultrasound substantially changes the dislocation characteristics of the crystal (lengths of the oscillating dislocation loops as well as the parameters of the dislocations). A change in the state of the dislocation subsystem gives rise to the observed nonlocality of the acoustodislocation interaction, manifested as a hysteresis of the damping coefficient of the acoustic wave as a function of the wave amplitude, including the region of a decrease in damping. Decreasing damping is not present in the string model, which takes account of only the change in the lengths of the dislocation loops, leaving other characteristics of the dislocations unchanged.

We note that the effects described above have been observed in relatively pure crystals with dislocation densities up to 10^6 cm^{-2}. Apparently, in contaminated samples with a much higher dislocation density or in metals[1] a decrease in damping is not observed, since in such materials effects due to dislocation charge exchange on point defects are weak or suppressed.

[1] W. P. Mason [Ed.], *Physical Acoustics*, Academic Press, N. Y., Vol. 4A; Nauka, Moscow, 1969.
[2] S. P. Nikanorov and B. K. Kardashev, *Elasticity and Dislocation Anelasticity of Crystals* [in Russian], Nauka, Moscow, 1985.
[3] T. Pustelny, Ultrasonics **33**, 289 (1995).
[4] O. A. Korotchenkov, A. Kh. Rozhko, and A. M. Antonov, Fiz. Tverd. Tela (St. Petersburg) **35**, 2244 (1993) [Phys. Solid State **35**, 1115 (1993)].
[5] I. V. Ostrovskii and O. F. Korotchenkov, Solid State Comm. **82**, 267 (1992).
[6] M. Benabdeslem and I. Ostrovskii, Revue Phys. Appl. **25**, 1005 (1990).
[7] O. A. Korotchenkov, A. T. Marchenko, and I. V. Ostrovskiĭ, Zh. Tekh. Fiz. **62**, 187 (1992) [Sov. Phys. Tech. Phys. **37**, 895 (1992)].
[8] A. Granato and K. Luecke, Journ. Appl. Phys. **27,** 789 (1956).

Translated by M. E. Alferieff

Voltage dependences of the amplitude and phase of reflected radiation in liquid-crystal structures with surface plasmons

D. I. Kovalenko

M. G. Chernyshevskiĭ Saratov State University
(Submitted December 3, 1996)
Pis'ma Zh. Tekh. Fiz. **23**, 75–80 (September 26, 1997)

The results of a theoretical calculation of the amplitude and phase of *p*-polarized monochromatic radiation reflected from layered liquid-crystal structures with surface plasmons as a function of the external voltage applied to the structure (in the Kretschmann geometry) are reported.
 [S1063-7850(97)02809-7]

Surface plasmons have been studied for many years both theoretically and experimentally. They have been attracting a great deal of attention in recent years because of their applications in the spectroscopy of surfaces, optical microscopy, the development of optical sensors for different physical quantities,[1–3] and the development of electrically and optically controlled light modulators, including liquid-crystal modulators. In a number of works mainly devices in a regime of amplitude modulation of the reflected radiation were studied experimentally and theoretically. The characteristics of liquid-crystal light modulators with surface plasmons under different voltages have been investigated only experimentally.[10]

The objective of the present work is to investigate theoretically the properties of liquid-crystal structures with surface plasmons in the presence of a voltage. The present Letter reports the results of a theoretical calculation of the voltage dependence of the amplitude and phase of reflected *p*-polarized monochromatic radiation ($\lambda = 6328$ Å) for different liquid-crystal structures with surface plasmons.

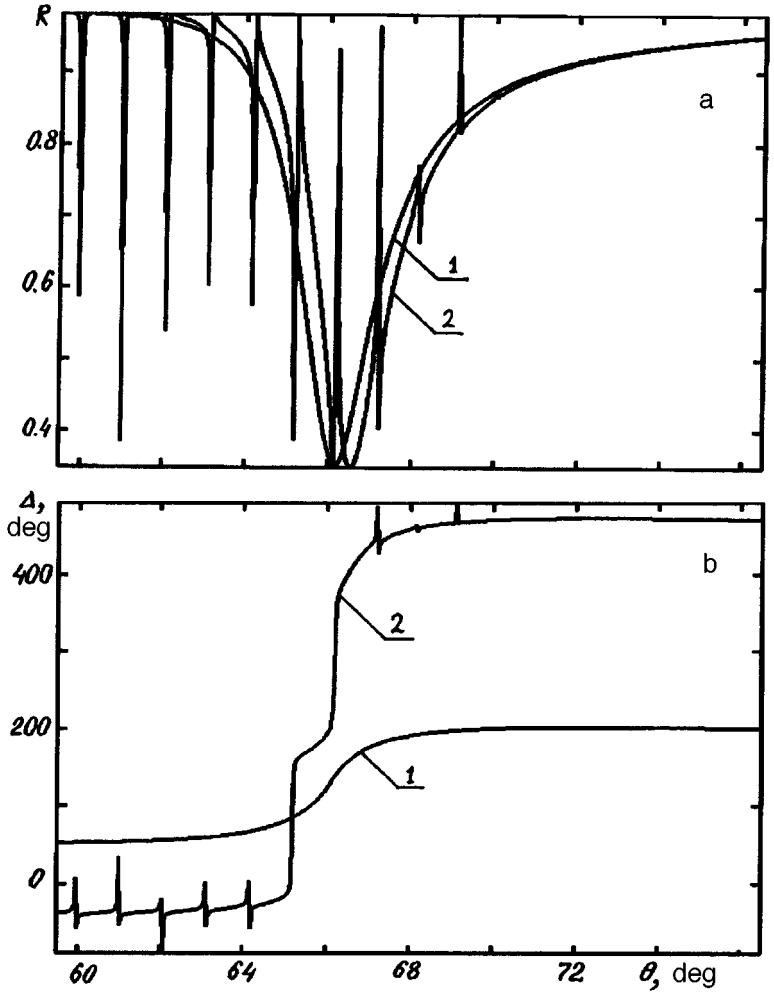

FIG. 1. a — Energy reflection coefficients versus angle of incidence with a fixed voltage. Curve *1* — 0 V, curve *2* — 6 V. b — Phase shift between the *p*- and *s*-components of the reflected radiation versus the angle of incidence with a fixed voltage. Curve *1* — 0 V; curve *2* — 6 V.

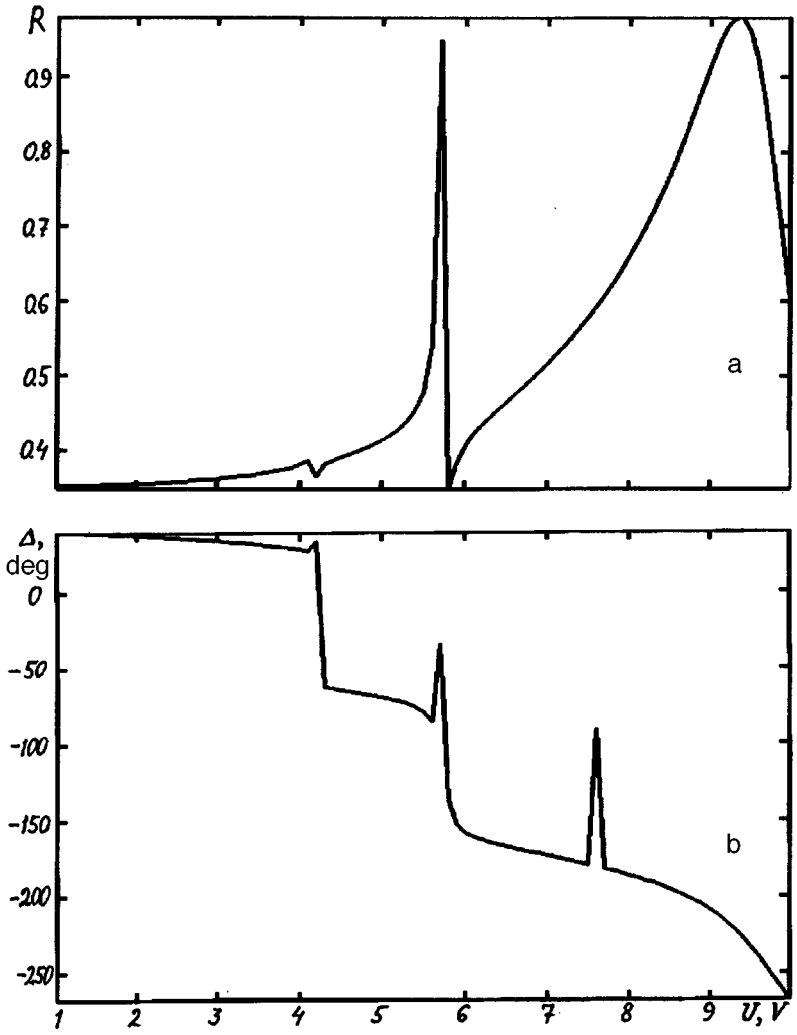

FIG. 2. Energy reflection coefficient for reflected radiation versus voltage for a fixed angle of incidence 66.0875°. b — Phase shift between the *p*- and *s*-components of the reflected radiation versus voltage with a fixed angle of incidence 66.0875°.

Such problems can be solved either by means of the Fresnel equations[5] or by the matrix method.[4,7] The present work employs the matrix method.[7] Both methods require uniform layers. For this reason, instead of one liquid-crystal layer, a set of uniform layers were substituted. In the calculations the layers of the liquid crystal were divided into 256 layers. For a large number of layers the computational results were practically the same but the computational time became extremely long. For each layer, the tilt angle of the director was calculated for a fixed voltage from the solution of the following system of equations[8]

$$\frac{V}{V_0}=\frac{1}{\pi}(1+Y(1+\gamma))^{1/2}\int_0^{\infty}\times\sqrt{\frac{(1+Y)(1+W)+kYW}{((1+Y)(1+W)+\gamma YW)(1+Y+W)(1+W)W}}\,dW, \tag{1}$$

$$\frac{2z}{L}\int_0^{\infty}\sqrt{\frac{((1+Y)(1+W))+kYW)((1+Y)(1+W)+\gamma YW)}{(1+Y+W)(1+Y)(1+W)W}}\frac{dW}{1+W}=\int_0^{W_L}\sqrt{\frac{((1+Y)(1+W)+kYW)((1+Y)(1+W)+\gamma YW)}{(1+Y+W)(1+Y)(1+W)W}}\frac{dW}{1+W}, \tag{2}$$

$$V_0=\pi\sqrt{\frac{k_{11}}{\varepsilon_0(\varepsilon_{\parallel}-\varepsilon_{\perp})}}, \tag{3}$$

$$W_L=\frac{\tan^2\Phi(1+Y)}{Y-\tan^2\Phi}, \tag{4}$$

$$k=\frac{(k_{33}-k_{11})}{k_{11}}, \tag{5}$$

$$\gamma=\frac{(\varepsilon_{\parallel}-\varepsilon_{\perp})}{\varepsilon_{\perp}}, \tag{6}$$

where L is the thickness of the plate, z is the distance into the plate, $Y=\tan^2\Phi_m$, and Φ_m is the maximum tilt angle of the director.

It was assumed that in the absence of a voltage the tilt angle of the director was equal to zero, though in real structures this angle is ordinarily equal to several degrees.

The computer programs were checked on the materials used in Refs. 6 and 8. Complete agreement with the published results was obtained.

The amplitude and phase as functions of the angle of incidence were calculated for voltages ranging from 1 to 10 V with a step of 0.1 in the range of angles of incidence from

59.5 to 76.5°. Next, the voltage dependences for different angles of incidence were constructed from the computed dependences on the angle of incidence in the presence of different voltages.

The following structure (in the Kretschmann geometry) was employed: glass ($n=1.8$), metal ($\varepsilon=-17.75+i\cdot 0.787$, $d=400$ Å), SiO_x ($\varepsilon=2.234+i\cdot 0.0045$, $d=265$ Å), liquid crystal ($d=95400$ Å, $\varepsilon_{\parallel}=18.7$, $\varepsilon_{\perp}=4.4$, $n_0=1.526$, $n_e=1.74$, $K_{11}=11.7e-12$ N·m^{-1}, $K_{33}=18.9e-12$ N·m^{-1}).

The computed curves of the energy reflection coefficients for the *p*-polarized component of the radiation versus the angle of incidence for two voltages applied to the liquid-crystal structure are presented in Fig. 1a. The computed dependences of the phase difference between the *p*- and *s*-components of the reflected radiation on the angle of incidence for two voltages applied to the liquid-crystal structure are shown in Fig. 1b. It is evident from the figures that when a voltage is applied, the modes appearing in the liquid-crystal structure strongly distort the ideal pattern of the frustration of the total internal reflection. For this reason, the properties of the modes should be used in devices based on a structure with a liquid crystal under a voltage.

Curves of the reflection coefficient for *p*-polarized light as a function of the voltage applied to the liquid-crystal structure are presented in Figs. 2a and 2b. The curves were calculated for the same structure in amplitude and phase modulation regimes with a fixed angle of incidence. Analysis of the figure shows that this structure can be used as an effective light modulator, since both the amplitude and phase characteristics contain sections with a large slope angle. Choosing the required section of the curve, it is possible to develop a device possessing both high sensitivity and good linearity of the transfer characteristic. It is possible to develop devices for a wide range of voltages. For this, it is only necessary to vary the angle of incidence/reflection.

Thus, the program developed for calculating not only the amplitude but also the phase of the reflected *p*-polarized radiation in the regime of excitation of surface plasmons in structures with a liquid crystal, taking account of the anisotropy of the properties of the layers, is the next step in the solution of the problems of determining the properties and characteristics of structures based on surface plasmons, including liquid-crystal structures.

[1] V. M. Agranovich and D. L. Mills [Eds.], *Surface Polaritons. Electromagnetic Waves on Surfaces and Interfaces* [in Russian], Nauka, Moscow, 1985.
[2] N. L. Dmitruk, V. G. Litovchenko, and V. L. Strizhevskiĭ, *Surface Polaritons in Semiconducotrs and Insulators* [in Russian], Naukova dumka, Kiev, 1989.
[3] K. R. Welford, Opt. and Quantum Electron. **23**, 1 (1991).
[4] J. M, Simon and V. A. Presa, J. Mod. Opt. **36**, 649(1989).
[5] M. Born and E. Wolf, *Principles of Optics*, Pergamon Press, N. Y., 1980, 6th edition; Mir, Moscow, 1973].
[6] S. A. Basmanova, Opt. spektrosk. **76**, 100 (1994).
[7] G. J. Sprokel, Cryst. Liq. Cryst. **68** (1981).
[8] K. R. Welford and J. R. Samples, Liquid Crystals **2**, 91 (1987).
[9] V. F. Nazvanov and D. I. Kovalenko, Pis'ma Zh. Tekh. Fiz. **21**, 60 (1995) [Tech. Phys. Lett. **21,** 565 (1995)].
[10] V. F. Nazvanov, A. O. Afonin, and A. I. Grebennikov, Kvant. Élektron. **22**, 1063 (1995).
[11] J. T. Remillard, J. M. Ginder, and W. H. Weber, Appl. Opt. **34**, 3777 (1995).
[12] L. Levesque and B. E. Paton, Can. J. Phys. **72**, 651 (1994).

Translated by M. E. Alferieff

Mass-spectrometric investigation of the thermal stability of polymethyl methacrylate in the presence of C_{60} fullerene

L. A. Shibaev, T. A. Antonova, L. V. Vinogradova, B. M. Ginzburg, V. G. Ginzburg, V. N. Zgonnik, and E. Yu. Melenevskaya

Institute of Problems of Machine Engineering, Russian Academy of Sciences, St. Petersburg; Institute of High-Molecular Compounds, Russian Academy of Sciences, St. Petersburg
(Submitted April 3, 1997)
Pis'ma Zh. Tekh. Fiz. **23**, 81–85 (September 26, 1997)

The thermal degradation of polymethyl methacrylate, synthesized by the method of free-radical polymerization, in a mixture with C_{60} fullerene has been investigated by mass-spectrometric thermal analysis. C_{60} suppresses the first two, low-temperature, stages in the thermal degradation of polymethyl methacrylate and thereby increases its thermal stability.
 [S1063-7850(97)02909-1]

Thermal stability is one of the most important technical characteristics of polymers. In a previous work[1] it was shown that the thermal stability of polystyrene decreases substantially in the presence of C_{60} fullerene. The thermal stability was characterized by the onset temperature and the temperature of the highest rate of thermal degradation of the polymer or its mechanical mixture with C_{60} heated at a constant rate. These temperatures were determined by mass-spectrometry according to the release of a monomer.

In the present Letter it is shown that in the case of polymethyl methacrylate synthesized by free-radical polymerization C_{60} fullerene can suppress depolymerization at relatively low temperatures and therefore exert a stabilizing influence, improving the thermal stability of the polymer.

The polymethyl methacrylate was chosen as the object of investigation for a number of reasons. First, a monomer comprises the main mass (more than 92%) in the gaseous products of the thermal degradation of polymethyl methacrylate. This greatly simplifies the analysis and interpretation of the experimental results. Second, the mechanism of polymerization of polymethyl methacrylate and the corresponding molecular structure have been studied comparatively well.[2–7] This structure (in contrast to polymethyl methacrylate synthesized by the method of anionic polymerization, contains repeating units of different configuration, including units with weakened C–C bonds, which can be called ''defects.'' For this reason, the changes in the character of the thermal degradation of polymethyl methacrylate in the presence of C_{60} can serve for obtaining information about the properties of C_{60} itself and for assessing its role not only in the ''gross'' thermal degradation but also in some fine details of the degradation mechanisms that are associated with the presence of these ''defects.''

The products of thermal degradation were analyzed by the method of mass-spectrometric thermal analysis.[8] The samples, located in a vacuum ($10^{-2}-10^{-3}$ Pa), were heated at a rate of 5°/min and at the same time the different gaseous products of their thermal degradation were detected with a MKh-1320 mass spectrometer. In order to eliminate, when possible, the fragmentation of the products of thermal degradation by electron impact, the products were ionized by a beam of low-energy electrons (18 eV).

We obtained by mass-spectrometric thermal analysis results that convey quite accurately the picture of thermal degradation of polymethyl methacrylate observed earlier in Refs. 2 and 3 by thermogravimetry. A curve of the yield of the monomer (with molecular mass 100) as a function of temperature during heating of pure polymethyl methacrylate is presented in Fig. 1 (curve 1). At least three peaks with temperatures of the maximum yield $T_{max}=160$, 280, and 375 °C can be distinguished in the thermogram. In accordance with Refs. 2 and 3, the first peak refers to the formation of a monomer by rupture of ''defect'' bonds of the ''head to head'' type and depolymerization of the macroradicals formed:

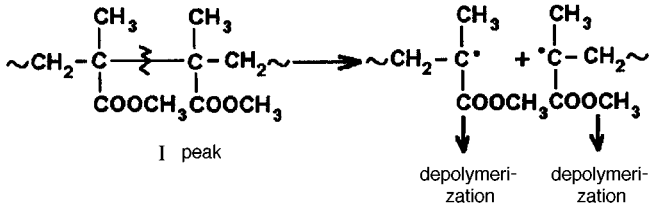

The energy of such bonds is approximately 20 kcal/mole lower than the energy of the ordinary C–C bonds in the main chain (62–65 kcal/mole),[9] rupture of which corresponds to the most intense peak with $T_{max}=375$ °C.

The second peak with $T_{max}=280$ °C refers to the formation of a monomer from a macroradical formed after the rupture of a β-bond at the end unit containing an umsaturated bond:

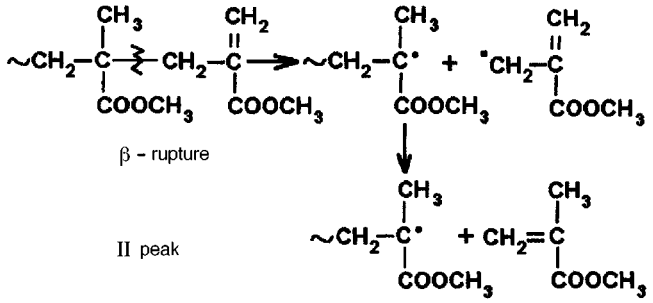

The rupture energy of a β-bond is approximately 10 kcal/mole less than that of a C–C bond in the main chain.[9]

The third peak has the same temperature characteristics

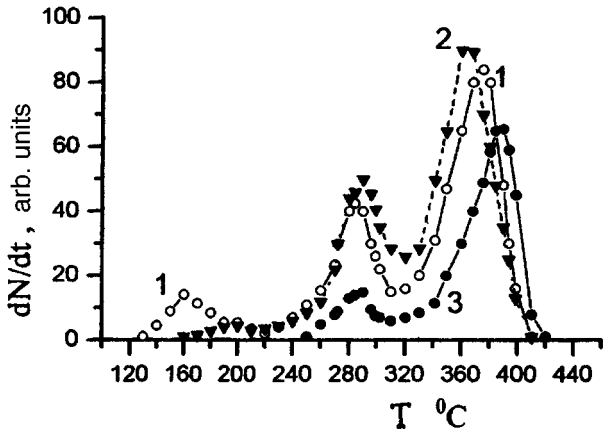

FIG. 1. Production rate dN/dt of the monomer (in arbitrary units) versus temperature: *1* — initial polymethyl methacrylate; *2* — anthracene-containing polymethyl methacrylate (one anthracene-containing unit per 880 ordinary units); *3* — mixture of polymethyl methacrylate with C_{60} (in a 9:1 ratio by weight).

as the peak formed a result of thermal degradation of polymethyl methacrylate obtained by anionic polymerization and therefore not possessing weak bonds:

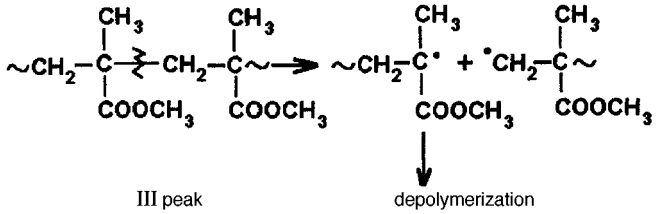

We found that polycyclic structures such as anthracene can suppress the chain radical decomposition of polymers, including polymethyl methacrylate. Figure 1 (curve *2*) shows the dependence of the monomer yield accompanying the degradation of polymethyl methacrylate in which there is one anthracene-containing unit per 880 ordinary monomer units. One can see that even at the low concentration indicated the anthracene-containing units exert an inhibiting influence, expressed as a decrease of the first peak and a shift of this peak in the direction of high temperatures.

It has been suggested that on account of its high reactivity C_{60} fullerene can also inhibit the thermal degradation of polymethyl methacrylate. For the investigations we prepared homogeneous samples of a mixture of solutions of polymethyl methacrylate and C_{60} in a common solvent (toluene). As one can see from the thermograms (see Fig. 1, curve *3*), C_{60} fullerene completely suppresses the low-temperature thermal degradation (expressed as the absence of the first peak), decreases the amount of the monomer released in the second peak, and shifts the third peak to high temperatures by 10–15°. The vanishing of the first peak signifies that at temperatures of 160–200 °C the rupture of bonds in the units located in the ''head to head'' position does not lead to depolymerization of the radicals which are formed and, apparently, results in a rapid reaction of the macroradical with the double bond of fullerene, which results in the formation of a covalent bond between the fullerene carbon and the polymer chain polymethyl methacrylate, the rupture energy of the bond being at least 65 kcal/mole.

A similar explanation is possible for the decrease in the intensity of the second peak in the region 240–290 °C. On account of the higher temperature (compared with the first peak), some of the radicals formed after the β-bond is ruptured can depolymerize, and the remaining radicals give covalent bonds with C_{60} fullerene, the bond energy being no lower than the energy of the C–C bond in the main polymer chain. A similar explanation was given for the suppression of the first and less effective suppression of the second peak of thermal degradation of polymethyl methacrylate in the presence of oxygen.[3]

The high strength of the C_{60}–polymethyl methacrylate bond can be explained from the standpoint of the interaction of the general π-electron system of the fullerene molecule with the *n*-electrons of the functional groups of the monomer units of the polymethyl methacrylate chain.

In summary, in contrast to mixtures with polystyrene, in the case of the thermal degradation of polymethyl methacrylate synthesized by the free-radical polymerization method the presence of C_{60} fullerene suppresses thermal degradation. This results in a decrease of the intensity of the low-temperature peaks in the thermograms, right up to complete vanishing of the peaks, as well as in a shift of the main, high-temperature, peak in the direction of high temperatures.

This work was performed as part of the Russian Scientific-Technological Program ''Fullerenes and atomic clusters'' (Project ''Tribol'').

[1] B. M. Ginzburg, A. O. Pozdnyakov, V. N. Zgonnik *et al.*, Pis'ma Zh. Tekh. Fiz. **22**(4), 73 (1996) [Tech. Phys. Lett. **22**, 166 (1996)].
[2] T. Hirata, T. Kashiwagi, and J. Brown, Macromolecules **18**, 1410 (1985).
[3] T. Kashiwagi, A. Inaba, J. E. Brown *et al.*, Macromolecules **19**, 2160 (1986).
[4] T. Kashiwagi, A. Inaba, and A. Hamins, Polymer Degrad. and Stab. **26**, 161 (1989).
[5] L. E. Manring, Macromolecules **21**, 528 (1988).
[6] L. E. Manring, Macromolecules **22**, 2673 (1989).
[7] L. E. Manring, D. G. Sogan, and G. M. Cohen, Macromolecules **22**, 4652 (1989).
[8] L. A. Shibaev, T. A. Antonova, L. A. Fedorova *et al.*, Vyskomolek. soed., Ser. A **37**, 1874 (1995).
[9] J. Mito, in *Aspects of Degradation and Stabilization of Polymers*, edited by H. H. G. Jellinek, Elsevier Scientific Publishing Company, N. Y., 1978, pp. 247–294.

Translated by M. E. Alferieff

Distinctive features of the thermal degradation of poly-*N*-vinylpyrrolidone cross-linked by C_{60} fullerene molecules

L. A. Shibaev, T. A. Antonova, L. V. Vinogradova, B. M. Ginzburg, V. N. Zgonnik, and E. Yu. Melenevskaya

Institute of High-Molecular Compounds, Russian Academy of Sciences, St. Petersburg; Institute of Problems of Machine Engineering
(Submitted April 9, 1997)
Pis'ma Zh. Tekh. Fiz. **23**, 87–92 (September 26, 1997)

The thermal degradation of polymer networks obtained by cross-linking by C_{60} molecules through the functional groups of pyrrolidone rings has been investigated by mass-spectrometric analysis for the example of poly-*N*-vinylpyrrolidone. The thermal degradation of the networks differs substantially in character from the case of free poly-*N*-vinylpyrrolidone. © *1997 American Institute of Physics.* [S1063-7850(97)03009-7]

The present work is a continuation of a series of investigations[1–3] of the influence of C_{60} fullerene on the thermal stability of different types of polymer compounds. Here the thermal stability of irregular polymer networks obtained by cross-linking through the carbonyl groups of the pyrrolidone rings of poly-*N*-vinylpyrrolidone by C_{60} molecules is investigated the first time.

Fullerene-containing poly-*N*-vinylpyrrolidone, obtained by a new method of synthesis, making it possible to introduce quite large quantities of C_{60} covalently bound with poly-*N*-vinylpyrrolidone, was chosen as the object of investigation.

The details of the synthesis process will be published elsewhere. In the present Letter we shall indicate only the main principles of this process. We shall focus our attention on the results of mass-spectrometric thermal analysis[4] of the effect of C_{60} on the thermal degradation of fullerene-containing poly-*N*-vinylpyrrolidone as compared with the thermal degradation of the initial compound.

Serva poly-*N*-vinylpyrrolidone with molecular mass $MM = 10000$ was employed as the initial material. To obtain fullerene-containing poly-*N*-vinylpyrrolidone the C_{60} was first activated by a reaction in a solution with potassium tert-butylate (tert-BuOK) in a 1:3 ratio:

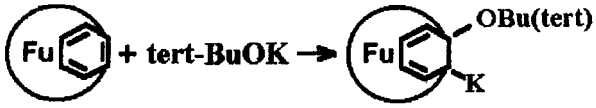

Monitoring of the changes taking place in the concentrations of the reaction components shows that on the average three tert-BuOK molecules were attached to each C_{60} molecule.

Thus, a network can form as a result of the interaction with poly-*N*-vinylpyrrolidone (PVP in the diagram):

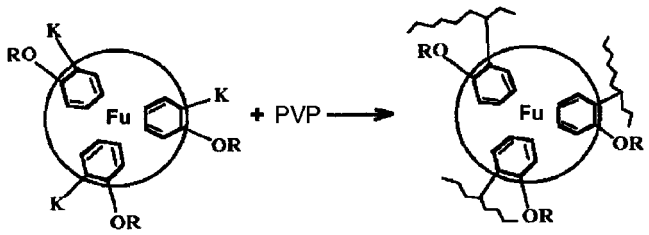

Since a poly-*N*-vinylpyrrolidone macromolecule contains approximately 100 repeating units and the molecular ratio of C_{60} and repeating units of poly-*N*-vinylpyrrolidone was equal to 1:24 (~21 wt % C_{60}), each poly-*N*-vinylpyrrolidone macromolecule can be multiply cross-linked with neighboring molecules and give an insoluble, cross-linked product, as is observed experimentally. It is obvious that C_{60} molecules occupy the sites in this network. In addition, an important technological feature of the network is that the intermolecular cross-links form randomly through the carbonyl groups of the pyrrolidone rings, i.e. the network is irregular.

The mass-thermogram of the initial poly-*N*-vinylpyrrolidone (Fig. 1) exhibits a definite similarity to the mass-thermogram of polymethyl methacrylate synthesized by the radical polymerization method.[3] Since poly-*N*-vinylpyrrolidone was synthesized by the same method and the positions of the peaks in the thermograms (170, 220, 320, and 420 °C) are close to the peaks for polymethyl methacrylate, the origin of the peaks can be explained similarly: The presence of poly-*N*-vinylpyrrolidone fragments, in which the repeating units are attached to one another ''head to head,'' in the main chain as well as the presence of unsaturated end groups result in rupturing of the ''weakened'' C–C bonds in the chain followed by depolymerization at temperatures much lower than the temperature of thermal degradation of poly-*N*-vinylpyrrolidone chains which do not contain weak bonds.

In the case of poly-*N*-vinylpyrrolidone the situation is, however, complicated by the presence of an α-hydrogen atom in the repeating unit. During thermal degradation, this leads to, first, reactions that break and transport the chain and, second, rupture of the relatively weak C–N bond, which leads to detachment of pyrrolidone rings from the poly-*N*-vinylpyrrolidone molecule.

Therefore, the process of degradation of poly-*N*-vinylpyrrolidone does not reduce to depolymerization. Indeed, besides ions with mass

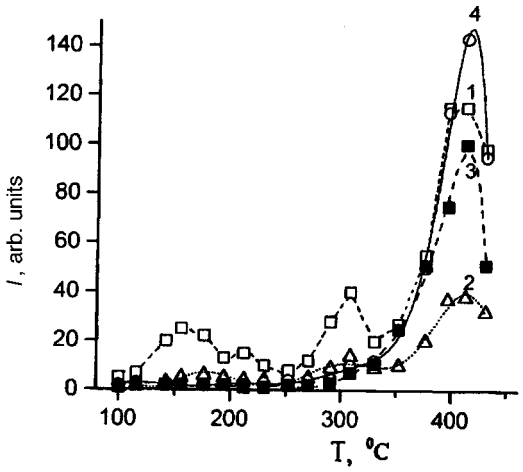

FIG. 1. Intensity of the release of the main products of thermal degradation of poly-*N*-vinylpyrrolidone as a function of temperature: 1 — mass 85; 2 — mass 84; 3 — mass 56; 4 — mass 111.

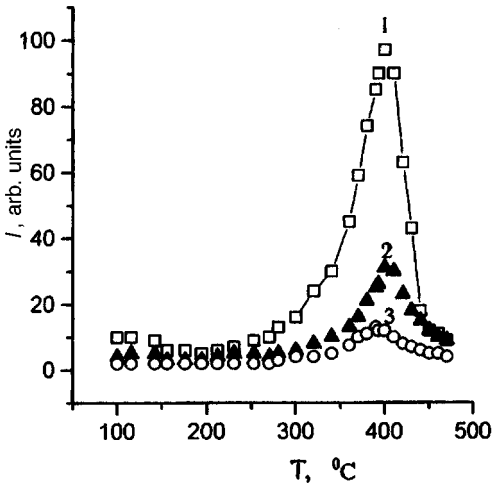

FIG. 2. Intensity of the release of the main products of thermal degradation of a network consisting of fullerene-containing poly-*N*-vinylpyrrolidone as a function of temperature: 1 — mass 85; 2 — mass 84; 3 — mass 111.

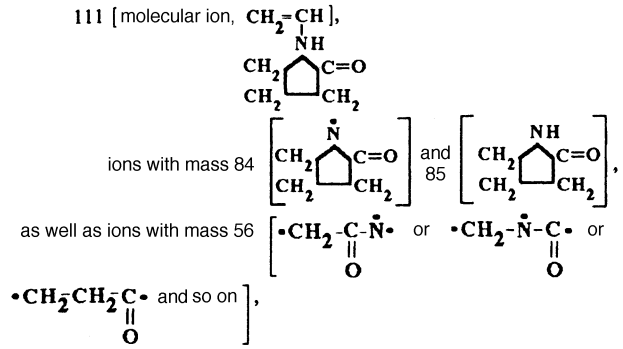

whose relative intensity varies in the temperature range 100–500°C (see Table I), are observed in the mass spectra.

Apparently, detachment of pyrrilidone rings along the C–N bonds, lying near the ''defect'' configurations of the main chain occurs primarily in the first three peaks at the corresponding temperatures. The intensity of the release of molecular ions is approximately an order of magnitude lower than that of ions with mass 85. The intensity of ions with mass 56 is also relatively low and can be attributed to splitting off of linear fragments of the chains near such ''defects'' as well as partial decomposition of the pyrrolidone rings.

In the fourth peak, located near 420 °C, the character of the thermal degradation changes, since homolithic rupture of any (and not only ''defect'') bonds in the repeating unit becomes possible. Furthermore, the depolymerization process (with formation of products with mass 111) becomes comparable in intensity to the total process of formation of the ions with masses 85 and 84. The intensity with which fragments with mass 56 are released increases substantially as a result of the increase in the rate of decomposition of the pyrrolidone rings.

All low-temperature peaks are practically absent in the mass thermogram of the fullerene-containing poly-*N*-vinylpyrrolidone (Fig. 2). All products of thermal degradation are released near ≈400 °C. Although this peak shifts somewhat toward lower temperatures with respect to the fourth peak of thermal degradation of poly-*N*-vinylpyrrolidone (evidently because of the fact that the C_{60}–C bond is weaker than the C–C bond in the main chain), the absence of the low-temperature peaks can be interpreted to mean that the thermal stability of the system is higher than that of the initial poly-*N*-vinylpyrrolidone.

The presence of cross links prevents depolymerization. Only a weak peak was mass 111 is seen. Apparently, thermal degradation proceeds predominantly with detachment of pyrrolidone rings (masses 84 and 85) and only ~10% of the chains decompose as a result of depolymerization.

Therefore, just as in polymethyl methacrylate[3], in the case of networks of fullerene-containing poly-*N*-vinylpyrrolidone C_{60} fullerene inhibits low-temperature degradation, the thermal stability of the main chain of poly-*N*-vinylpyrrolidone decreases somewhat at high temperatures, and decomposition of the polymer chain with splitting off of the pyrrolidone ring is the predominant mechanism of thermal degradation.

TABLE I. Intensity of release of the main products of thermal degradation (in relative units), corresponding to different values of m/e.

	m/e			
T, °C	111	85	84	56
170	40	1000	320	100
220	100	1000	320	125
320	87	1000	325	200
420	1000	786	253	693

This work was performed as part of the Russian Scientific-Technological Program ''Fullerenes and atomic clusters'' (Project Tribol).

[1] B. M. Ginzburg, A. O. Posdnyakov, V. N. Zgonnik, O. F. Posdnyakov, B. P. Redkov, E. Yu. Melenevskaya, and L. V. Vinogradova, Pis'ma Zh. Tekh. Fiz. **22**(4), 73 (1996) [Tech. Phys. Lett. **22**, 166 (1996)].
[2] A. O. Posdnyakov, O. F. Posdnyakov, B. P. Redkov, V. N. Zgonnik, E. Yu. Melenevskaya, L. V. Vinogradova, and B. M. Ginzburg, Pis'ma Zh. Tekh. Fiz. **22**(18), 57 (1996) [Tech. Phys. Lett. **22**, 759 (1996)].

[3] L. A. Shibaev, T. A. Antonova, L. V. Vinogradova, B. M. Ginzburg, V. N. Zgonnik, and E. Yu. Melenevskaya, Pis'ma Zh. Tekh. Fiz. **23**(18), 81 (1997) [Tech. Phys. Lett. **23**, 730 (1997)].
[4] L. A. Shibaev, T. A. Antonova, L. A. Fedorova, S. I. Klenin, I. A. Baranovskaya, and B. L. Erusalimskiĭ, Vysokomolek. Soed., Ser. A **37**, 1874 (1995).

Translated by M. E. Alferieff